NASA Contractor Report 201607
DOT/FAA/ND-96/2

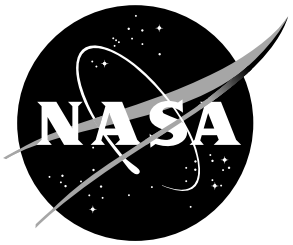

Performance of the NASA Airborne Radar With the Windshear Database for Forward-Looking Systems

George F. Switzer and Charles L. Britt
Research Triangle Institute, Research Triangle Park, North Carolina

Contract NAS1-18925

September 1996

National Aeronautics and
Space Administration
Langley Research Center
Hampton, Virginia 23681-0001

Table of Contents

List of Tables

List of Figures

Abstract

This document contains a description of the simulation approach used to test the performance of the NASA airborne windshear radar. Explanation of the actual radar hardware and processing algorithms provides an understanding of the parameters used in the simulation program. This report also contains a brief overview of the NASA airborne windshear radar experimental flight test results. A description of the radar simulation program shows the capabilities of the program and the techniques used for certification evaluation. Simulation of the NASA radar is comprised of three steps. First, the choice of the ground clutter data must be made. The ground clutter is the return from objects in or nearby an airport facility. The choice of the ground clutter also dictates the aircraft flight path since ground clutter is gathered while in flight. The second step is the choice of the radar parameters and the running of the simulation program which properly combines the ground clutter data with simulated windshear weather data. The simulated windshear weather data is comprised of a number of TASS (Terminal Area Simulation System) model results. The final step is the comparison of the radar simulation results to the known windshear data base. The final evaluation of the radar simulation is based on the ability to detect hazardous windshear with the aircraft at a safe distance while at the same time not displaying false alerts.

Conversion Table

Conversion Factors for Metric (SI) to Customary U.S. Units

To Convert	*Multiply by*	*To Get*
cubic meter (m^3)	35.31	cubic feet (cu ft)
gram (g)	0.035274	ounces (oz)
kilometer (km)	0.62137	statute miles
kilometer (km)	0.5396	nautical miles
meter (m)	3.2808	feet (ft)
meters per second (m/s)	196.8	feet per minute (ft/min)
meters per second (m/s)	1.9426	knots
meters per second (m/s)	2.237	miles per hour (mph)

Glossary

FBAR	An average of the wind shear hazard index (F-factor) taken over a flight path segment of a specified distance (1 km in this document).
hazardous windshear	Region of performance-decreasing winds with a 1-km averaged F-factor exceeding 0.105.
ILS	Instrument Landing System -- A system designed to provide an approach path for exact alignment and descent of an aircraft on final approach to a runway (Airman's Information Manual, 1993).
microburst	Region of divergent windshear that has a horizontal wind change of at least 10 m/s within a 4-km segment.
performance-decreasing winds	Windshear that causes a loss of aircraft performance.
PPI	Plan Position Indicator -- a display of selected parameters as a function of range and azimuth position relative to the aircraft.
stable layer	A vertical thickness of air with static stability: a parcel displaced vertically within such a layer is subjected to a buoyant force opposite to its displacement.
TASS	Terminal Area Simulation System -- A multi-dimensional numerical large-eddy simulation model developed at NASA Langley Research Center for the general purpose of studying phenomena such as microbursts, convective rain storms, gust fronts, hailstorms, atmospheric boundary layers, and aircraft wake vortices.
thunderstorm gust front	The transition zone at the leading edge of strong outflow from thunderstorm downdrafts, often referred to as "gust front."

1.0 Introduction

1.1 Purpose

The purpose of this report is to describe the performance of the NASA airborne forward-looking windshear radar system against established certification procedures. The radar was installed on the NASA Boeing 737 research aircraft and has been a test bed for evaluating the ability of an airborne radar to warn aircraft about potential encounters with hazardous windshear (Harrah et al. 1993). The testing of the NASA radar is based on the FAA requirements to certify an airborne windshear detection system.

The certification testing process involves three phases. The first phase involves gathering radar ground clutter data from particular airport facilities using an airborne radar flown on specified flight scenarios. Radar ground clutter is the signal return from objects on or nearby the airport facility. The second phase is to simulate the radar performance in an environment which is the result of the proper combination of the environmental ground clutter data and a simulated windshear environment. The windshear environment is one of seven cases contained within the windshear database developed at NASA Langley Research Center (Switzer et al. 1993). The final phase is the evaluation of the performance of the NASA radar system with the windshear data base. This numerical simulation approach provides a quick and accurate method of evaluating the NASA airborne forward-looking windshear radar in situations of low airspeed and altitude.

1.2 Background

The need for a sensor to detect low-altitude windshear was recognized in the mid-1980's. In the United States, during the period 1964 to 1985, windshear has been a contributing factor in at least 26 civil transport accidents and 3 incidents involving 500 fatalities and over 200 injuries (Bowles 1990). The Federal Aviation Administration (FAA) established a focused research and development program over a multi-year period. NASA signed a memorandum of agreement with the FAA in July 1986 to pursue a cooperative research program to address problems related to airborne detection, avoidance, and survivability of hazardous windshear environments (Bowles 1990).

One of the sensors investigated for the airborne windshear detector is microwave pulse Doppler radar. A comprehensive airborne Doppler radar simulation program was first developed to assess the feasibility of airborne Doppler radar to detect hazardous windshear with critical areas of concern being severe ground clutter, rain attenuation and low reflectivity levels. After successful completion of the assessment phase, an experimental airborne Doppler radar was developed (Harrah et al. 1993). The NASA radar is a prototype of forward-looking windshear radar systems and has been instrumental in assisting the FAA with assessing the performance of commercial airborne windshear radar systems. The NASA system is not a commercial system, therefore there was no need for certification. However, it has undergone extensive evaluation in both field studies and simulation testing. This report brings to a conclusion the effort of the NASA airborne radar system by documenting the characteristics of the hardware, the details of the simulation strategy, and the results of the simulation performance testing.

1.3 Overview of Documentation

The NASA airborne radar system is described in section 2.0. The description details the hardware, signal and data processing algorithms, and the experimental flight tests. Section 3.0 describes the radar simulation program. Descriptions of the windshear database along with the certification paths to be used with each data set are found in section 4.0.

Section 4.0 also contains descriptions of the simulation case runs that were performed. The results of the simulation runs are detailed in section 5.0 and concluding remarks are made in section 6.0. Plots of radar clutter PPI (Plan Position Indicator) plots are shown in appendix A and selected PPI plots of simulation results are shown in appendix B.

Appendix C contains line plots comparing measured hazard and wind velocity with actual database values along a particular azimuth line.

2.0 Description of NASA Airborne Radar System

2.1 Hardware Implementation

An experimental airborne radar was designed and implemented to collect ground clutter data and evaluate and verify wind shear detection capability of an airborne X-band Doppler radar. The radar implemented utilized a modified-production 708 weather radar like those used in commercial airlines. A number of key modifications and enhancements were incorporated in the 708 radar. External systems for signal detection, data processing, and data storage were added. The 708 radar includes a flat plate slot array antenna, a receiver/transmit (R/T) unit, and a control and display unit. The modifications to the basic unit included multiple and higher pulse repetition frequencies (PRF) multiple and more narrow transmission pulse widths, higher transmitter power, increase number of antenna control functions, and a number of output interface connections from various portions of the R/T unit. Improvements to the stability and low-phase noise characteristics of the stable local oscillator were also incorporated. NASA procured the standard 708 radar, with the specified modifications, from the Rockwell-Collins Corp. Collins produces standard 708 weather radars for the commercial airline industry. The additional external systems were designed and built in-house by NASA.

The NASA-designed external systems include a receiver sub-system which employs a fast-acting bin-to-bin Automatic Gain Control (AGC) system, a 12-bit digitized I/Q (In-phase & Quadrature) detector, a digital interface unit responsible for generating system timing and control signals, and a 14-track Kodak Data Tape flight recorder. The raw I/Q data pulses were recorded on the flight Data Tape for later processing and analysis. A real-time signal and data processor system was also employed during flight tests so radar velocity and hazard factor PPI displays could be presented to the pilots and researchers on the airplane. Harrah et al. provides a more detail description of the radar design and flight test results.

2.2 Signal and Data Processing Algorithms

A detailed analysis and performance assessment was conducted on data collected during the flight experiments to evaluate the windshear detection performance of the radar. Each raw I/Q data file was processed through a set of signal and data processing algorithms to determine the wind velocities, rain reflectivity, F-factors, and hazardous windshear detected by the radar. The F-factor is a quantitative measure of the effect of the windshear to either increase or decrease the performance of the aircraft. Positive values of F-factor are related to performance decreasing winds and negative values relate to performance increasing winds. The F-factor equation was originally explained in Bowles (1990). The results were evaluated to determine the capability of the radar to detect and alert of hazardous windshear. A baseline set of algorithms and threshold settings were used for the analysis. For the radar simulation performance testing described in this document, a similar set of algorithms and threshold settings were used. Table 2.1 lists the baseline signal processing techniques used for clutter rejection and velocity estimation. The techniques used for total hazard index estimation and the

procedure for assessing the hazard level are listed in Table 2.2. Table 2.3 lists the key thresholds used in the baseline algorithms when processing the radar data generated during the simulation runs.

.

Table 2.1 Clutter Rejection & Velocity Estimation

- Separate AGC for each range bin to allow processing with maximum dynamic range
- Antenna tilt control to reduce main beam clutter
- A/C velocity compensation
- Data processed through HANN window
- 128 pulse FFT Doppler processing
- Stationary ground clutter filtering using Doppler line editing of 0 3 m/s
- Compute mean and standard deviation of target velocity using Pulse-Pair algorithm in the frequency domain

Table 2.2 Hazard Estimation Procedure

- Velocity gradient is estimated over 5 range bins least-square fit
- If least-squares residual is less than a residual threshold continue hazard index (F_T) computation
- Compute F_h component of hazard index
- Compute F_V add to F_h to obtain F_T
- Compute moving average of the F_T values over range window = 1000 meters
- Determine contiguous regions in radar scan that exceed FT threshold. Calculate area(s)
- Identify area(s) in excess of an area threshold and track the region centroid with track-while-scan algorithm
- If hazard region exists for 2 consecutive scans & time to closest approach is less than 100 sec, then alert on hazardous area.

Table 2.3 Threshold Levels Used For Flight Experiments

Minimum signal level for processing	-112 dBm
Minimum SNR level for processing	- 3 dB
Maximum spectrum width on velocity estimation	10 m/s
Velocity slope estimation residual	3 m/s
Hazard factor (F_T) threshold	.105
Area threshold	.2 sq. km
Track distance threshold	750 m
Successive tracks	2
Time to closest approach	100 s

2.3 Experimental Flight Tests

An extensive flight test program was conducted to assess the wind shear detection performance of the airborne Doppler radar as well as other airborne sensors systems. Wind shear testing of these systems were coordinated between ground-based radars, the ATC (Air Traffic Control) system, and various governmental and research organizations. Wind shear flight experiments (38 in all) were performed primarily around the Orlando, FL airport (MCO), and Denver, CO airport (DEN), in the summers of 1991 and 1992. Table 2.4 summarizes the total wind shear events encountered during these flight experiments. Listed are the F-factor levels and in situ alerts encountered by the aircraft and the number of wind shear events detected by the radar. Since the radar was scanning a large area in front of the aircraft (usually a 60^o sector out to ~13 km), more wind shear events were seen and detected by the radar than were encountered by the aircraft. In many cases, the aircraft turned away from these events since either the reflectivity or F-factor exceeded the safe levels for aircraft penetration.

Table 2.4 Summary of Wind Shear Events Encountered: 1991&1992 Flight Experiments

Flight Location	Aircraft Flights	Weather Runs	Aircraft Wind Shear Encounters In Situ (F_T>0.05)			Airborne Radar Detection
			F_T<0.105	F_T>0.105	Total	
Orlando	19	221	43	12	55	70
Denver	19	134	15	6	21	27
Total	38	355	58	18	76	97

A total of 76 wind shear events (where F_T >.05) were encountered by the aircraft during the wind shear flight experiments. The radar obtained data from all but two of the 76 events. During these two events the radar tape recorder was off when the aircraft encountered a small unknown shear event while in a high-bank turn. Both of these

events, which occurred in Denver, were undetected by the ground radar. As shown in the table 2.4, the radar detected and recorded data from 21 additional events in Denver. Of the total aircraft encounters, 18 produced in situ alerts (F_T >.105). The remaining 58 events had F-factor values between .05 and .105.

A broad spectrum of microburst and gust front events were encountered during the flight experiments. The analysis of this data illustrated the wide range of hazardous windshear characteristics a pilot can encounter, and the capability of the radar to detect these events and provide timely pilot alerts. The analysis of the flight data showed that the radar can detect both dry and wet microbursts, both symmetrical and unsymmetrical microbursts, as well as hazardous gust fronts. It was also shown that, over the ranges required to provide timely alerts, rain attenuation is not a serious problem for detecting hazardous windshear.

3.0 Description of Radar Simulation Program

3.1 General Discussion

The certification process presents unique problems because of the near-impossibility of testing the proposed systems in a realistic environment. While the NASA tests of the experimental system demonstrated the possibility of observing numerous hazardous windshears in flight tests, the windshears observed were not generally located in areas of severe ground clutter as may be encountered on a landing approach or takeoff. Also, safety and operational factors prohibit flight tests through hazardous windshear at low altitudes and slow aircraft speeds. For these reasons, a simulation approach was used in early evaluations of the NASA system concept, with the validity of the simulation later confirmed by data from flight test of the NASA experimental system.

The success of the NASA system and microburst simulation approach led to a certification methodology consisting of a combination of flight tests and simulation. In this concept, illustrated in Figure 3.1, ground clutter data will be collected by manufacturers of systems being considered for certification at several severe clutter locations (*e.g.*, Washington National, Newark, and Denver) and will be merged with simulated microburst data generated by the Terminal Area Simulation System (TASS) (Proctor 1987a, 1987b, 1988a, 1988b, 1989, 1993, Proctor and Bowles 1992, Proctor et al 1995). The merged data will then be subjected to the signal, data processing, display, and hazard alert algorithms of the proposed system (using actual hardware or hardware emulation) to determine the success of the system in meeting the FAA-specified performance goals.

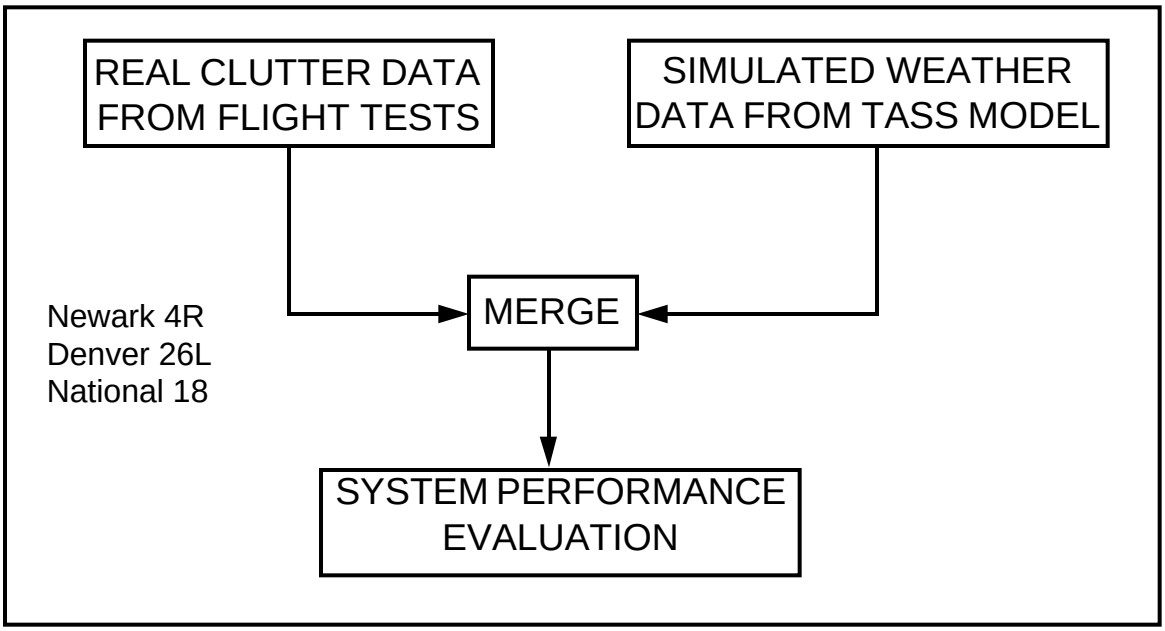

Figure 3.1 Illustration of Certification Methodology Using Merged Flight and Simulated Data.

To test the certification concept, the techniques were applied to the NASA experimental system. As mentioned above, extensive simulations had been conducted to determine the performance characteristics of the NASA system. After development of the experimental hardware, programs were developed to test various signal and data processing routines using the experimental flight data. The testing of the certification concept required the use of both the simulation and flight data processing programs and the development of algorithms to properly merge the flight and simulated data.

The following sections provide a description of the simulation approach used initially to predict the windshear detection performance of the NASA experimental Doppler radar and a description of the flight data processing program used to process radar flight data. Parts of the simulation (i.e., those associated with the generation of signals from a simulated microburst) were then incorporated into the flight data processing program along with (new) data merging algorithms to properly combine the simulated microburst signals with the real radar (clutter) data.

3.2 General Description of the Radar Simulation

As a vehicle for determining system performance under realistic conditions, a comprehensive computer simulation of a pulse-Doppler airborne radar was developed (Britt 1990). The simulation program (Airborne Windshear Doppler Radar Simulation - AWDRS) has been used extensively in the NASA program to evaluate radar parameter trade-offs and various signal and data processing techniques proposed to reliably detect windshear in the presence of ground clutter.

The radar simulation computer model is a comprehensive calculation of the expected outputs of an airborne coherent pulsed-Doppler radar system viewing a low-level microburst along or near the approach path of the aircraft. The simulation contains algorithms for direct calculation of radar signal returns from data files that provide, at any point in space, the radar reflectivity of moisture and the scattering cross section of ground clutter. The instantaneous radar signal amplitude and phase is calculated by spatially integrating the radar equation over a large population of incremental scatterers (i.e., a Monte-Carlo calculation). Further calculations simulate the signal processing done by a coherent radar in filtering the signal, providing Automatic Gain Control (AGC), forming in-phase (I) and quadrature (Q) base-band signal components, converting the I and Q signals to digital values, filtering the I and Q signals, and deriving Doppler velocity, spectral width, shear hazard, and other radar outputs of interest.

The detailed nature of the simulation permits the quick evaluation of proposed trade-offs in radar system parameters and the evaluation of the performance of proposed configurations in various microburst/clutter environments. The simulation also provides a test bed for various proposed signal processing techniques for minimizing the effects of noise, phase jitter, and ground clutter as well as maximizing the useful information derived for avoidance of microburst windshear by aircraft.

Figure 3.2 is a block diagram indicating the major features of the simulation. Inputs to the program include an input file specifying the radar system parameters and large data files that contain the characteristics of the ground clutter and the microburst. The ground clutter data file consists of high-resolution (20m grid) calibrated synthetic aperture radar

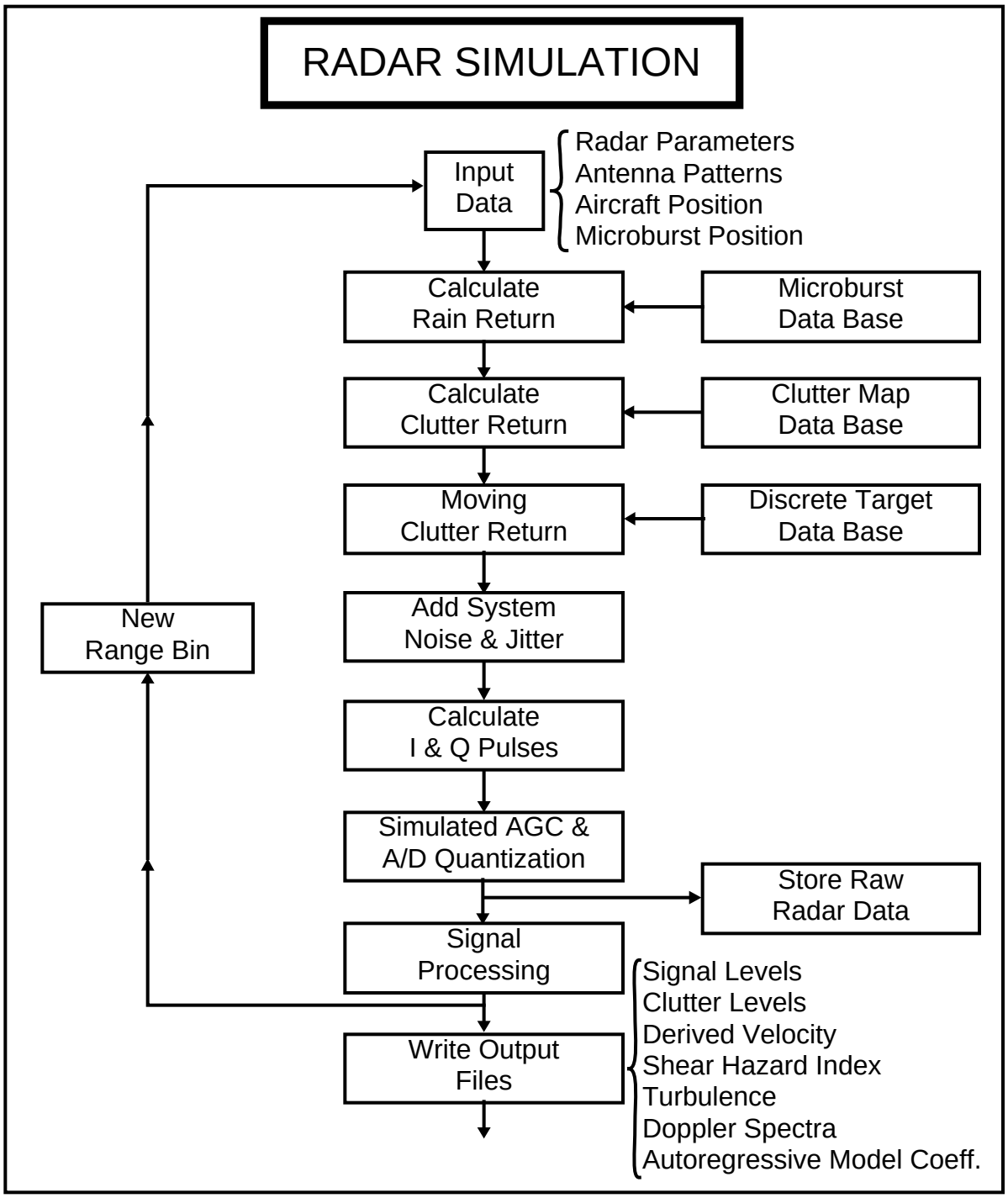

Figure 3.2 Flow Chart of the General Organization of the Airborne Doppler Windshear Radar Simulation (ADWRS) Program.

(SAR) data of selected airport areas collected by the Environmental Research Institute of Michigan (ERIM).

The microburst data files provide reflectivity factors, x,y,z wind velocity components and other meteorological parameters (Switzer et al. 1993). This data base has been created by TASS and is described in section 4.1.

For each range bin, the simulation calculates the received signal amplitude level by integrating the product of the antenna gain pattern and scattering source amplitude and phase over a spherical-shell volume segment defined by the pulse width, radar range, and ground plane intersection. The amplitude of the return from each incremental scatterer in the volume segment is proportional to either the square root of the normalized cross-section of the ground clutter (from the clutter map) or the square root of the reflectivity factor of the moisture in the microburst (from the microburst data base). The phase of each incremental scatterer is the sum of a uniformly-distributed (0 - 2π) random phase term, a phase term due to relative aircraft-scatterer radial velocity, and normally distributed random phase terms representing transmitter/receiver phase jitter and ground clutter random motion. The random phase terms simulating phase jitter and ground clutter motion are updated for each transmitted pulse while the uniformly-distributed phase terms are updated for each sequence of pulses in a range bin. The phase terms representing aircraft-scatterer relative motion are linear functions of time.

The basic equations used to calculate the I and Q pulse streams represent the pulses as the sum of many incremental scatterers, and may be written as follows:

$$I(t) = \sum_{i=1}^{N} A_i \cos\left[\tilde{\Phi}_i + \beta\left(V_i - V_a\right)t + \Delta\tilde{\Phi}\right] + \tilde{n}(t) \qquad (1)$$

$$Q(t) = \sum_{i=1}^{N} A_i \sin\left[\tilde{\Phi}_i + \beta\left(V_i - V_a\right)t + \Delta\tilde{\Phi}\right] + \tilde{n}(t) \qquad (2)$$

where

A_i is the amplitude of the return from scatterer i,

Φ is the random phase of scatterer i,

β is $2\pi/\lambda$,

V_i is the radial velocity component of scatterer i,

V_a is the radial component of aircraft velocity,

$\Delta\Phi$ is the (random) transmitter phase error,

n(t) is the (random) receiver noise term, and

N is the number of scatterers in the calculation.

Since weather return at X-band is known to remain coherent over an appreciable fraction of a second, the scatterer random phase is held constant over a complete frame of approximately 128 pulses, while the transmitter jitter and noise random phase variables change from pulse-to-pulse as discussed previously.

Path attenuation for each incremental scatterer is determined by integrating the path losses over the transmission path. The path loss is determined by converting the reflectivity values obtained from the microburst data base (at each point along the transmission path) into moisture content and then using empirical formulas (Doviak et al. 1984) to determine the incremental path losses from the moisture content.

Antenna patterns simulated include a generic parabolic antenna with size and aperture illumination taper specified by input data and a flat-plate array antenna with a pattern similar to that found in the current generation of X-band airborne weather radars. The latter antenna model consists of data obtained from actual antenna/radome measurements taken in the NASA-LaRC anechoic chamber.

A sequence of N pulses of in-phase (I) and quadrature (Q) signal amplitudes are calculated for each range bin as discussed above and subjected to AGC amplification and analog-to-digital (A/D) quantization. A simulated fast-acting AGC is used to adjust the gain of the system on a bin-by-bin basis to achieve a wide dynamic range and to prevent signal saturation (due to clutter) prior to and during A/D conversion. The I and Q pulse stream is then digitally filtered to suppress ground clutter near zero Doppler frequencies and processed using both conventional pulse-pair and spectral averaging algorithms to derive the average velocity and spectral width of the scatterers in the range bin. Further processing of the velocity data provides an estimate of windshear and aircraft hazard factor.

Provision is made in the simulation to generate returns from a specified number of range bins over several azimuth scans so that simulated color map displays of reflectivity, velocity, shear, spectral width, and hazard factor can be examined using a PC-based graphics program. Other outputs of the simulation include data for plots of power levels, velocity, spectral width, hazard factor, and AGC levels vs. radar range. Doppler spectra of ground clutter and moisture as derived from the I and Q signals from each simulated range bin can also be output and plotted if desired.

3.2.1 Clutter Model

The ground clutter model used for the initial simulation runs was a high-resolution X-band SAR map of the Willow Run, Michigan, airport area provided by the Environmental Research Institute of Michigan (ERIM). This airport area was selected for preliminary studies primarily because a SAR map of the area was available from previous ERIM efforts associated with SAR research. Under NASA sponsorship, ERIM later collected X-band SAR data at the Denver and Philadelphia terminal areas. The Denver data is extensive, with coverage of the terminal area at various grazing and azimuth angles.

The SAR map file was calibrated by ERIM personnel (using ground corner reflectors) to provide normalized cross-section data with a resolution of 20m. In the simulations, the aircraft is positioned at a selected distance from the runway touchdown point on a three-degree glide slope.

3.2.2 Moving Clutter Model

Discrete moving targets for the simulation are generated by a supplemental program called WXDGEN. This program uses statistical data on highway traffic densities and vehicular speeds to generate a data base consisting of a large number of discrete targets on highways associated with a specific ground clutter map. Roadway and traffic count data for input to the WXDGEN program are obtained from high-resolution aerial photographs that coincide with the areas covered by the ERIM SAR clutter maps.

The data base generated by WXDGEN provides up to 80,000 discrete targets with coordinate locations, velocities, and RCS values assigned to each target. The data base also contains targets such as aircraft on departure or approach paths.

The radar simulation uses the discrete target data by calculating the received amplitude and (random) phase of each discrete target within the integration area defined ground intercept of the integration volume discussed previously. Equations (1) and (2) are then used to calculate the contribution to the I and Q amplitudes by the discrete targets.

3.3 General Description of the Flight Data Processing Program

The windshear flight data processing program (CMPRS) is a program used to process raw radar data files from the NASA experimental windshear radar system. Algorithms in the program reduce the basic in-phase (I) and quadrature (Q) radar return pulses taken at each range bin into filtered and unfiltered power, Doppler velocity, and Doppler spectral widths for each range bin. Various type of Doppler clutter filters and velocity estimators can be applied to the raw data. The program usage has been previously described in Britt (1993).

The program provides up to five output files, each of which contains data processed with a user-defined set of signal processing techniques. The output files contain the processed radar data and the radar system auxiliary file. The radar auxiliary file contains information on the radar parameters, scan angles, aircraft location and attitude, in-situ hazard measurements, and other parameters of interest. Output files from the program are intended to be used as input files to the windshear radar “Quick-Look” program (Britt et al. 1993). The Quick-Look program contains windshear hazard detection algorithms and provides for display and analysis of the processed radar measurements.

The algorithms implemented in the CMPRS program include: a) Time-domain filtering with three user selectable IIR or FIR filters, b) Time-domain weighting of the radar data stream with Hann or Hamming data windows, c) Autoregressive (AR) spectral processing, d) Fast Fourier Transform (FFT) spectral processing, e) Line editing of

spectral lines (i.e., spectral domain filter), f) Pulse-pair spectral mean and width estimators, and g) Spectral averaging mean and width estimators.

Various combinations of the above algorithms can be user-selected to test a large set of signal processing techniques. Figure 3.3 shows a chart of the various algorithm combinations that may be used.

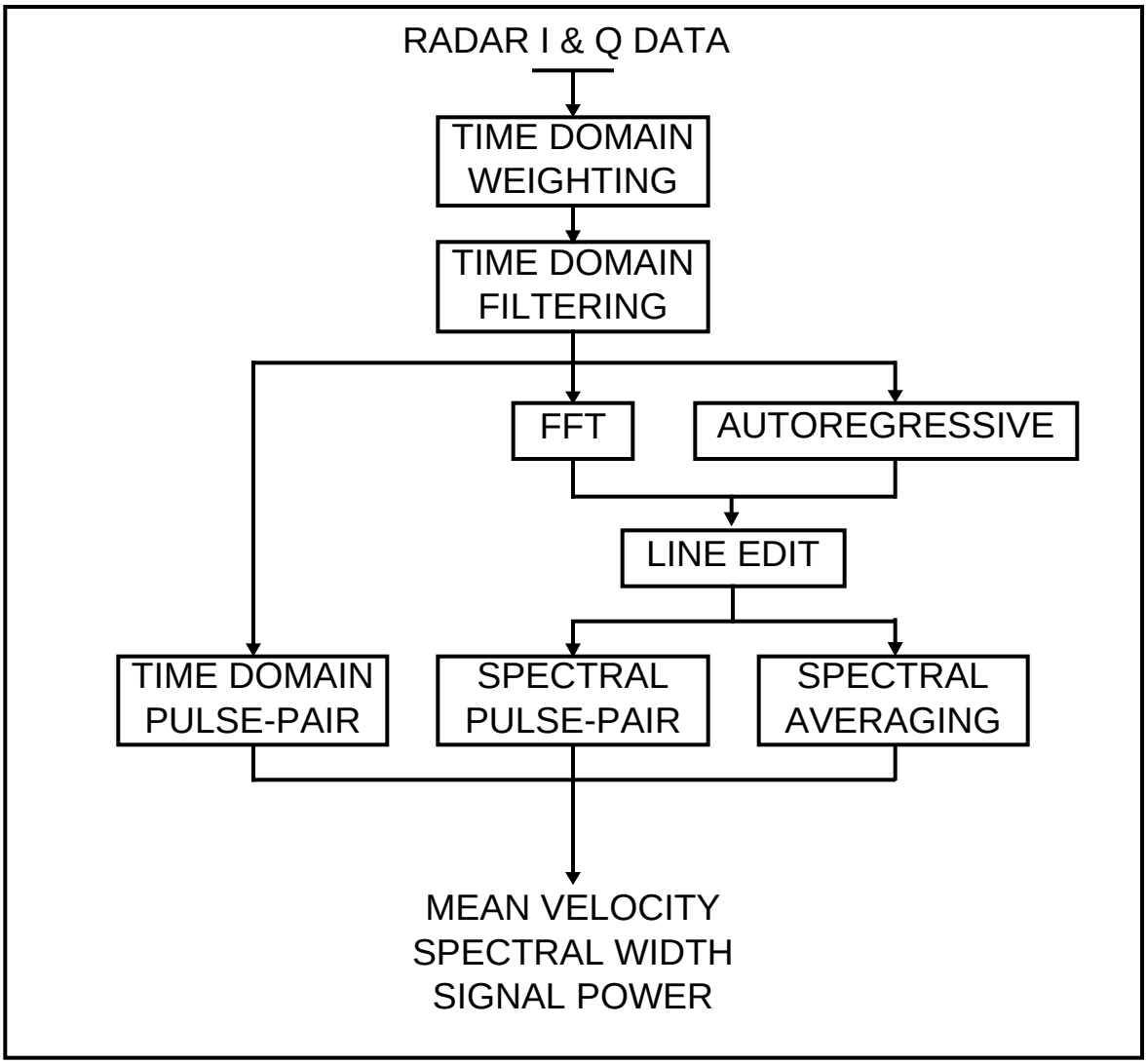

Figure 3.3 Chart Showing Signal Processing Algorithms that may be selected in the Flight Data Processing (CMPRS) Program.

3.4 Certification Evaluation Techniques

3.4.1 Simulation Model Algorithms Used

The set of algorithms associated with the generation of radar I and Q signals from the microburst model were extracted from the overall radar simulation (AWDRS) described above and were incorporated into the program used for processing flight data (CMPRS) from the NASA experimental radar system. Algorithms associated with generation of simulated ground clutter and simulated discrete targets were not used in the program used for the certification simulation.

3.4.2 Merging Flight and Simulated Data

The proper scaling and merging of flight and simulated data is critical to the success of the certification methodology for system performance evaluation. To determine possible problem areas and to serve as a guide to the use of the technique, the methodology has been applied to the NASA experimental system.

The data merging problem is illustrated in Figure 3.4. Figure 3.4a shows a simplified system gain model with gain to the IQ detector output of G/A. G is a constant system power gain factor (obtained by system calibration tests) and A is the value of the automatic gain control (AGC) attenuation factor. The flight data (clutter) provides actual IQ voltages and AGC levels, whereas the simulation (weather) module (from the ADWRS program) provides IQ voltages and associated power levels referenced to the system input. The desired merging process is illustrated schematically in Figure 3.4b, where the simulated weather signal is added to the real clutter signal to provide new IQ values and AGC levels. It is not possible to implement this process as shown because the real radar signals are available only at the IQ level and data merging must take place at this level.

If the system were completely linear, the merging at the IQ level could be accomplished by multiplying the simulated IQ pulse voltages by the square root of G/A and adding them to the real IQ voltages. The AGC levels would remain unchanged in this method however, and realistic AGC levels would not be available to output to subsequent analysis programs. This would effect the AGC thresholding processes used in the hazard detection algorithms. Also, small non-linearities in the system do exist and these would not be accounted for by this method.

There are several sources of non-linearity in the actual NASA system. These include; 1) the A/D converter acts somewhat as a limiter in that the AGC system is designed to allow approximately 5% of the IQ voltages to exceed values of maximum A/D output range (i.e. +/- 2048 millivolts); 2) the AGC system is designed to provide a constant averaged (over one frame of pulses) power level input to the A/D converter and therefore large clutter power levels will lower the weather signal-to-quantization noise ratio; and 3) the AGC is linear with power over a large but limited range. The net effect of these non-linearities is to cause suppression of small weather signals by large clutter signals and viceversa.

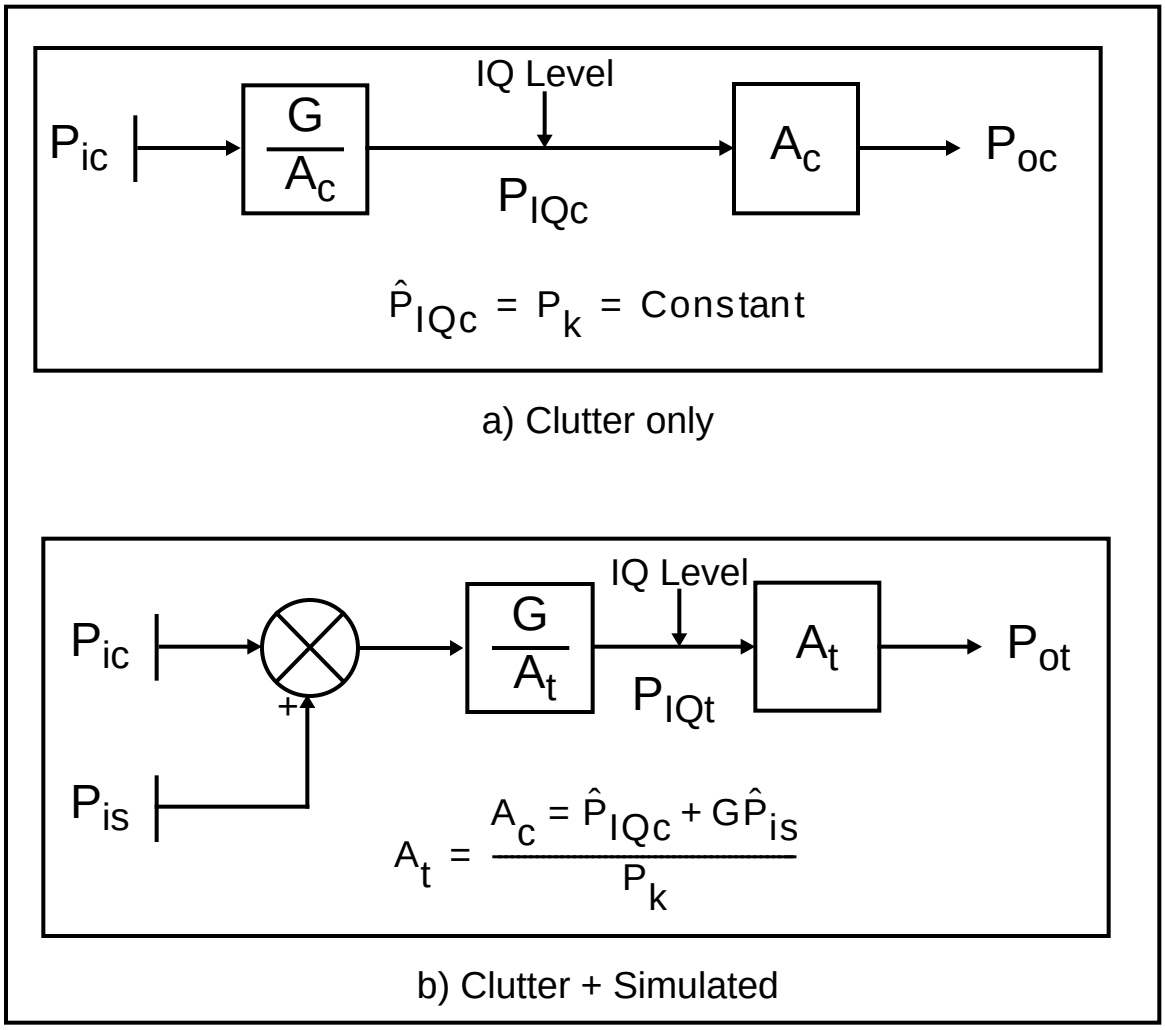

Figure 3.4 Diagrams Showing the Data Merging Problem for the NASA Experimental System.

Figure 3.5 shows a plot of the decrease in signal-to-quantization noise power ratio as a function of clutter-to-weather signal power ratio (CSR). As may be seen, the CSR must get relatively large before this effect becomes significant when using a 12-bit A/D converter. For A/D conversion using a smaller number of bits, the effect becomes significant at lower values of CSR.

3.4.3 Data Merging Technique

A method of superposition that can provide realistic AGC and IQ voltages and take into account the non-linearities discussed above has been developed and implemented (version V of the simulation program). This method calculates a new AGC gain level based on the averaged (over one frame of pulses) power of the real IQ voltages and the averaged power of the simulated weather IQ voltages. This new AGC level is a value that

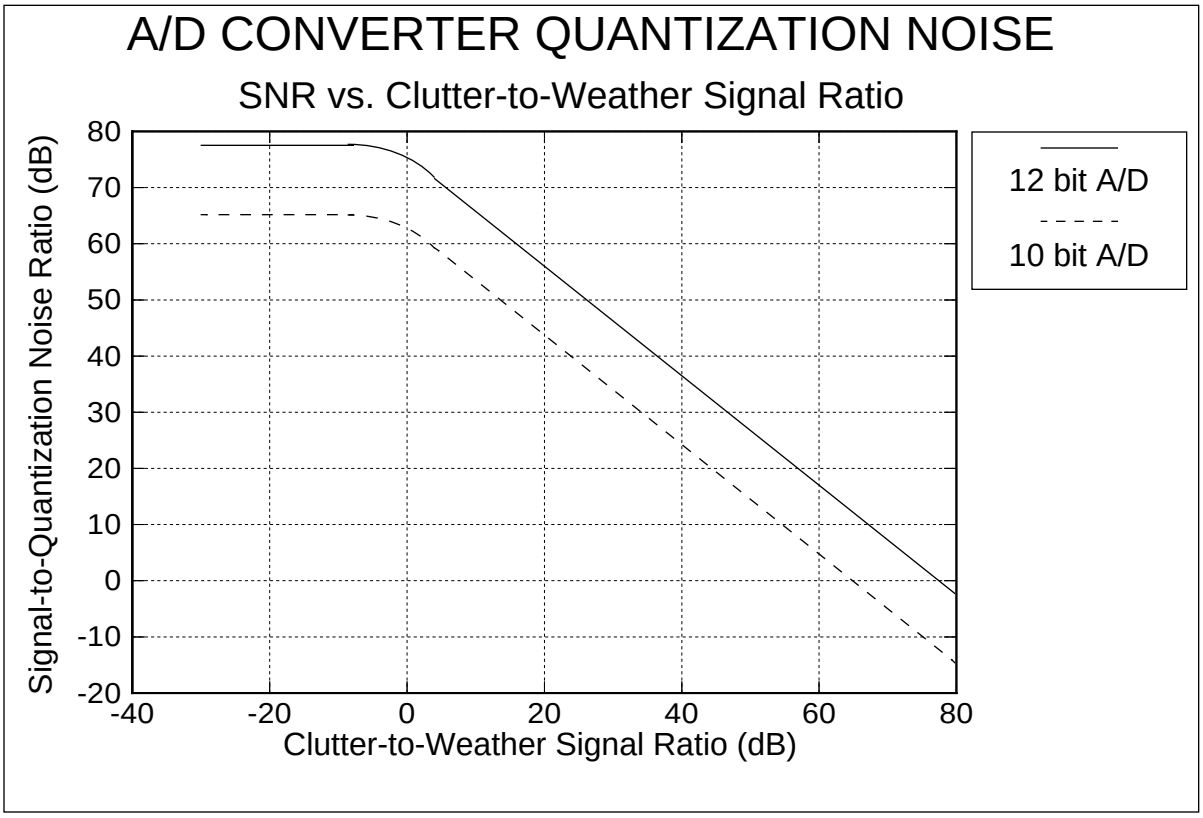

Figure 3.5 Decrease in signal-to-quantization noise ratio as a function of clutter-to-weather signal ratio.

would maintain a constant average power level at the input of the A/D converter. Using the models illustrated in Figure 3.6, the new value of AGC is found by

$$A_t = \frac{G\left(P_{ic} + P_{is}\right)}{P_k} = \frac{A_c P_{IQc} + G P_{is}}{P_k} \qquad (3)$$

where

A_t = Recalculated AGC level,

A_c = AGC level of real (clutter) data,

G = System Gain Calibration Constant,

P_{ic} = Averaged Power of real (clutter) IQ voltages,

P_{is} = Averaged Power of simulated (weather) IQ voltages, and

P_{IQc} = Power input to A/D converter (assumed constant).

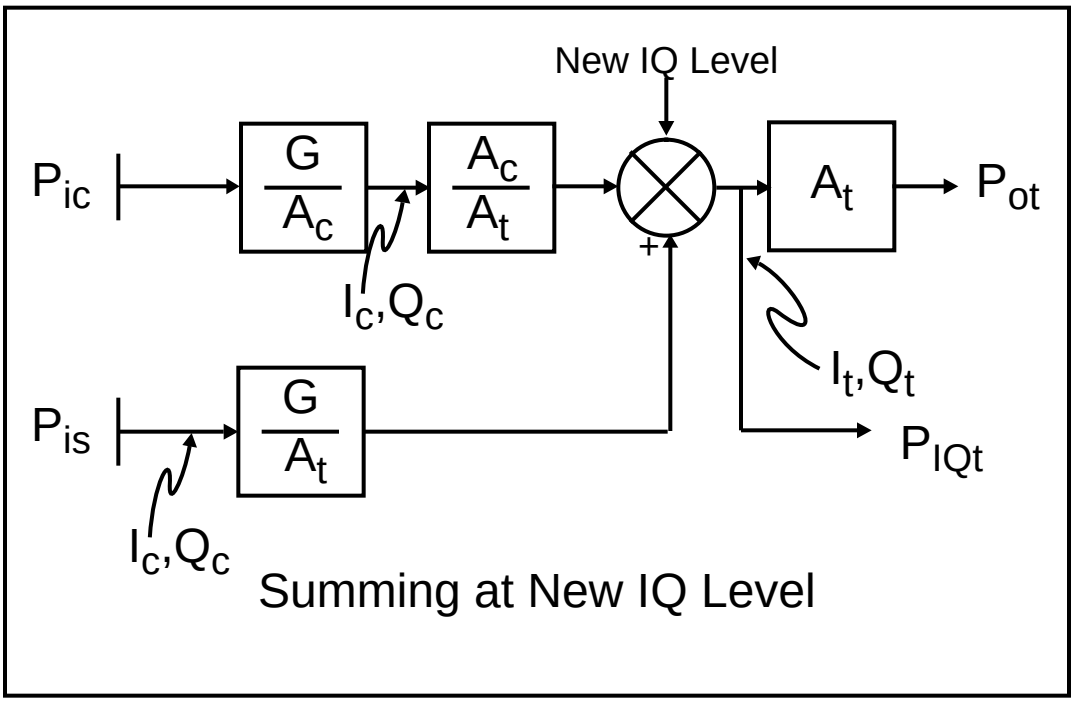

Figure 3.6 Illustrating the Method of Data Merging Used to Assure Proper Scaling of the Flight and Simulated Data for the NASA System.

Using the model shown in Figure 3.6 as a guide, the proper factors to use to scale both sets of IQ voltages prior to summing are calculated. These factors are as follows:

$$F_c = \left[\frac{A_c}{A_t}\right]^{\frac{1}{2}} \quad \text{(clutter)} \tag{4}$$

$$F_s = \left[\frac{G}{A_t}\right]^{\frac{1}{2}} \quad \text{(weather),} \tag{5}$$

where the nomenclature is defined above.

Using these multiplication factors, the new merged values of I and Q are calculated from the real and simulated values for each radar pulse as:

$$I_t = I_c F_c + I_s F_s \tag{6}$$

$$Q_t = Q_c F_c + I_s F_s, \tag{7}$$

where the c subscripts refer to clutter data and the s subscripts refer to simulated weather data. These new IQ values are then passed through simulated A/D converter algorithms that properly quantize the new values and then pass them, along with the new AGC values, to the signal processing routines of the data compression program for further processing into the power and velocity data which is written to the output files. A chart illustrating the combined simulation/flight data processing method used for evaluation of the NASA system is shown in Figure 3.7.

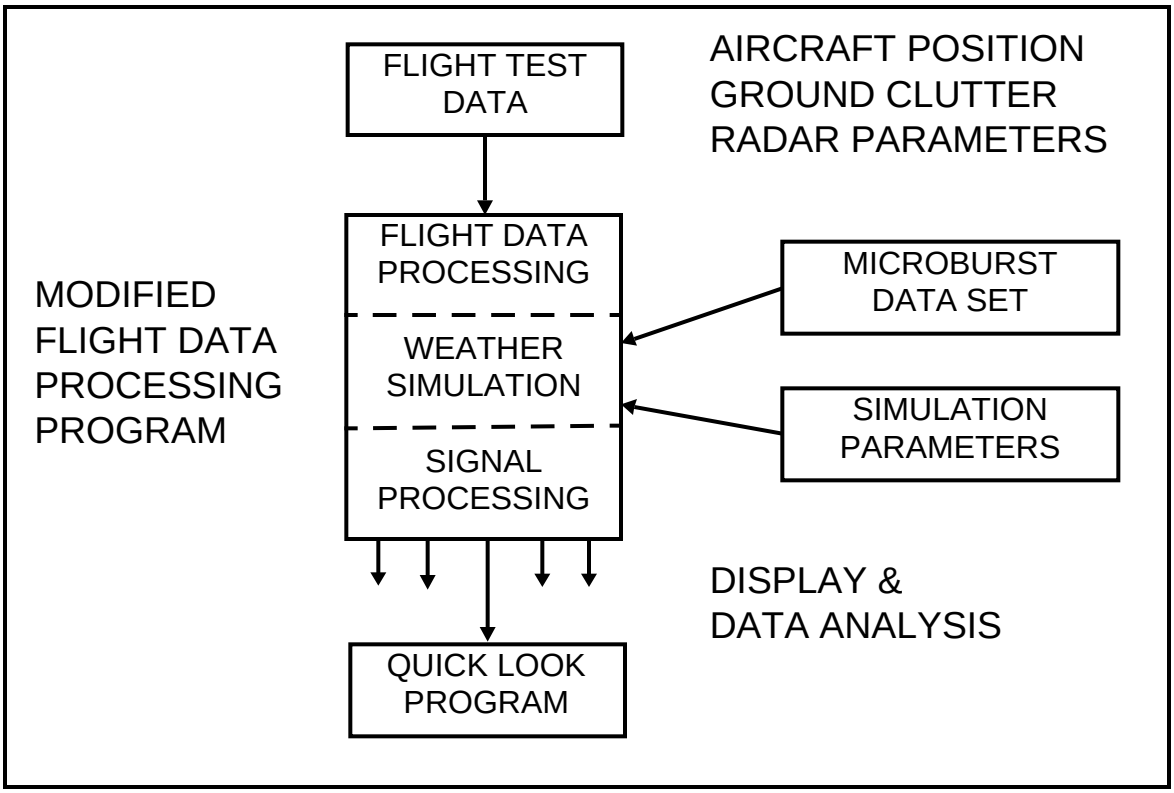

Figure 3.7 Chart Showing the ModifiedFlight Data Processing Program Used for Testing the Certification Concept.

4.0 Certification Simulation Case Runs

4.1 Windshear Database Description

The database was selected from a larger set of case studies conducted with the TASS model as described in Switzer et al (1993). It is designed to provide a wide range of scenarios for the testing of look-ahead sensors. The database is divided into nine data sets from seven case-study simulations. Table 4.1 summarizes each of the seven cases utilized in generating the nine certification data sets. The two additional data sets arise because each data set is frozen in time and cases three and five have two model simulation times. The windshear types represented include microburst types ranging from: 1) small- to large-scale events, 2) low- to high-reflectivity events, 3) symmetrical to asymmetrical events, and 4) weak to hazardous windshear. The database also includes scenarios with: 1) growing and decaying events, 2) interacting microbursts, 3) windshear with intervening rain, 4) microburst penetrating a ground-based stable layer, and 5) a gust front with hazardous shear. Several of the numerically-modelled events in this database represent real accident or incident windshear cases (Switzer et al. 1993).

4.2 Certification Path Scenarios

The six defined flight scenarios (Switzer et al. 1993) are:

1 Aligned for takeoff, near microburst

2 Aligned for takeoff, far microburst

3 Straight approach

4 Curved approach

5 Straight approach with drift

6 go-around

The first scenario is designed for the airplane to be in the headwind conditions of the microburst while the second is for the airplane to enter the hazard 3 nautical miles from brake release. The third is an ILS approach. The fourth scenario is a 90° turn onto the final approach path. The straight approach with drift is the same as the third scenario with a 25° drift angle. The final scenario is an ILS approach until 100 feet above ground level (AGL) at which point a go around maneuver is initiated. Paths are specified by flight direction of takeoff or approach. North, East, South, West correspond to flight direction or track 360, 90, 180, and 270, respectively. Table 4.2 details each of the path definitions utilized in this study. Paths are defined by data set, scenario, and path direction. Additional information is included in the table about the peak FBAR and radar reflectivity along the path.

Table 4.1 Description of Windshear Certification Database (from Switzer et al,1993)

Case No.	Simulation Description	Model Simulation Time (minutes)	Stage of Evolution for Primary Microburst	Approximate Peak 1-kilometer FBAR @ 150 kts	Approximate Diameter of Outflow @ Peak ΔV (km)	Approximate Microburst Core Reflectivity (dBZ)	Intervening Rain	Temp. Lapse Rate	Symmetry
1	DFW Accident Case, Wet Microburst, Rain and Hail	11	Peak Intensity	0.20	3.5	55	No	Adiabatic	Axisymmetric
2	6/20/91 Orlando, Florida, NASA Research Flight, Wet Microburst	37	Peak Intensity	0.19	3.5	50	Yes	Adiabatic	Rough Symmetry
3	7/11/88 Denver, Colorado, Incident Case, Multiple Microburst	49 51	Develop-ing Near Peak	0.08 0.20	3 1.5 - 3	35 20 - 40	Light Yes	Adiabatic	Varies Between Microbursts
4	7/14/82 Denver, Colorado, Stable Layer, Warm Microburst	36	Past Peak but Quasi-Steady	0.29	1.0	27	No	Stable Layer	Axisymmetric
5	7/8/89 Denver, Colorado, Very Dry Microburst	40 45	Near peak 2nd Pulse	0.18 0.16	3 3	17 - 20 5	No	Adiabatic	Rough Symmetry Asymmetric
6	Derived Florida Sounding, Highly Asymmetric Microburst	14	Decaying	0.16	1	50	Light	Adiabatic	Asymmetric
7	8/2/81 Adjusted Knowlton, Montana Sounding, Gust Front	27	N/A	0.14	N/A	20 (in area of largest FBAR)	No	Adiabatic	Asymmetric

Table 4.2 Certification Path Descriptions (from Switzer et al,1993)

Data Set	Scenario	Direction	Approx. Peak FBAR	Approx. Peak RRF (dBZ)	Notes
Case 1 11 min	2	East	0.2	57	Takeoff roll occurs outside domain of data set, with sensor looking into the data set.
	3	East	0.14	55	Approach may begin outside the boundary of the data set.
Case 2 37 min	3	South	0.14	50	About 4 km of intervening rain on path prior to encountering hazard.
	6	West	0.19	50	Runway touchdown zone is in clear air with microburst and 50 dBZ precipitation at far end of runway.
	3	East	0.06	50	Below-alert threshold case. FBAR of .08 exists 500 m right of path; 0.17 exists 2.5 km right of runway touchdown zone.
Case 3 49 min	3	East	0.08	25	Microburst strength is below alert threshold.
	3	North	0.13	37	Light precipitation about 2 km from event with moderate to heavy occurring about 1 km to right of max shear.
Case 3 51 min	1	North	0.17	24	
	2	East	0.19	37	Takeoff is in very weak shear with 20 to 35 dBZ precipitation, followed by about 1 km of clear air before encountering a 0.19 FBAR shear in 25 dBZ precipitation.
	3	360°	0.15	42	Mostly clear view of threat, with rain on each side of path.
	3	045°	0.18	42	Path between 2 small rain cells (30-35 dBZ) about 3 km short of runway.
	3	090°	0.17	41	Passes through intervening cell (20-30 dBZ and FBAR = .08) for last 4 km of approach to primary threat (FBAR=.17).
	3	135°	0.13	42	Passes along edge of adjacent precipitation cell before primary threat. Strong shear exists at far end of runway.

Table 4.2 Certification Path Descriptions (concluded)

Data Set	Scenario	Direction	Approx. Peak FBAR	Approx. Peak RRF (dBZ)	Notes
Case 3 51 min	3	270°	0.17	41	3 km from runway path touches edge of strong shear to south producing weak shear and 5-10 dBZ on path.
	3	315°	0.2	42	Penetrates 0.2 FBAR shear 3-4 km short of runway, with 25 dBZ precipitation. Primary shear has peak FBAR of 0.13 along path. Should detect both.
Case 4 36 min	1	East	0.23	27	Microburst has very small rain shaft: diameter of 5 dBZ contour is less than 1 km at 50 m altitude.
	3	East	0.24	27	
Case 5 40 min	2	West	0.18	22	Diameter of 5 dBZ contour ~1.6 km. About 1 km to each side of primary shear is FBAR of about .12-.15, with reflectivity of less than 0 dBZ.
	3	North	0.16	17	
	6	North	0.17	23	
Case 5 45 min	3	North	0.15	7	2nd microburst pulse, extremely dry. Zero dBZ contour diameter <1 km. Core penetration at 100 m altitude.
Case 6 14 min	3	360°	0.15	52	Clear view of windshear during approach.
	3	045°	0.18	50	
	3	090°	0.10	52	FBAR of .12 exists near path. Intervening rain at 2.5 km prior to peak.
	3	180°	0.15	52	2 km of intervening rain prior to peak.
	3	225°	0.19	50	Clear view of windshear during approach.
	3	270°	0.13	52	Clear view of windshear during approach.
	3	315°	0.13	52	Clear view of windshear during approach.
Case 7 27 min	1	West	0.12	50	Peak FBAR occurs about X = 22.3 km. Reflectivity in shear about 20 dBZ.
	3	West	0.13	26	

4.3 Flight Clutter Data

The phase of flight that is vulnerable to hazardous windshear is below approximately 1200 feet AGL. This corresponds to landing and takeoff conditions. The proximity to the ground gives rise to additional requirements for a windshear radar to properly distinguish between true windshear hazards and surrounding clutter. Clutter is the radar return from objects located on or near an airport facility (e.g., buildings or nearby roads with their associated traffic). The ability to determine what is ground clutter and what actually constitutes a windshear threat is a crucial part of an airborne forward-looking windshear radar. The certification requirements for a windshear radar by the FAA have specific constraints on the location of the radar clutter to be used with the windshear database; however, the NASA flight test program gathered clutter data prior to the constraints being defined. Therefore the clutter from the flight test program that closely matches the scenarios described above are used. No suitable clutter was gathered for either the curved approach or the straight approach with drift. The two primary clutter data sets are from Philadelphia International Airport and Denver Stapleton Airport. An additional set is used from Orlando International airport.

4.3.1 Clutter Flight Test Description

The clutter data from Philadelphia International Airport is used to simulate both landing and go-around approaches. The particular clutter is taken from a landing approach to runway 26R. The go-around approach is modelled by placing the microburst at the far end of the runway while for the Straight approach it is placed near the middle marker (900 meters from runway threshold). Clutter from Denver Stapelton Airport is used to simulate both of the takeoff scenarios. The clutter is obtained for takeoff from runway 35R. One simulation case utilizes the takeoff clutter from runway 18R at Orlando International Airport. The environment surrounding Orlando International Airport has very low levels of clutter. This data demonstrates the effect of clutter to hide the hazard. These three ground clutter data sets comprise all of the clutter utilized for this performance study.

4.3.2 Philadelphia Landing Approach Clutter Data

Figure A.1 shows the clutter environment of runway 26R. The Delaware river is seen in the foreground of the reflectivity plot and the traffic on Interstate 95 is shown in the wind velocity plot. The various buildings surrounding the runway are also evidenced by the high clutter areas near the runway.

4.3.3 Denver Takeoff Clutter Data

Figure A.2 shows the clutter reflectivity for the Denver runway 35R. No distinct features are present. There are strong returns from the terminal on the left and other buildings in the airport vicinity.

4.3.4 Orlando Takeoff Clutter Data

The clutter gathered at Orlando International airport contains very low clutter levels. This data is only used for one case.

4.4 Simulation Case Runs Performed

Each scenario is simulated by placing the microburst at a location relative to the runway threshold. The relative location of the microburst for each path scenario is described in Switzer et al. (1993). The syntax used to refer to each radar simulation case will be made up of the TASS case number, the TASS simulation time, and the path scenario as described in section 4.2 connected by underscores. For example case 1 at 11 minutes for a go-around is 1_11_6. For data sets with more than one ILS approach, the path scenario will have a letter appended to isolate each case (e.g., case 3 at 51 minutes on ILS track 135 is 3_51_3d).

Additional runs have been performed with enhanced reflectivity values for all scenarios of cases 4_36, 5_40, and 5_45. These cases have been denoted by appending an “er” to the end of the case number. The levels of reflectivity enhancement correspond to the FAA and industry accepted values and are labeled on Table 4.3. The case that utilizes the low clutter environment of Orlando and is referred to by appending “lc”. Table 4.3 labels each path that was simulated in the first column. The grayed areas represent runs that were not performed for a particular case.

Table 4.3 Performance Summary for NASA Certification Simulation Runs

Case No	Case Name	Path Definition	Advanced Warning Time, sec			FBAR Values						Outflow Refl. @Max Vel.,dBz	
						Clutter		No Clutter		Truth			
			Clutter	No Clutter	Truth	Ave.	Peak	Ave.	Peak	Ave.	Peak	HW	TW
1_11_2	DFW(11)	Takeoff East	82		82	.15	.171			.51	.176	46	46
1_11_3	DFW(11)	Approach East	104		104	.16	.204			.15	.186	43	43
2_37_3a	Fla.Wet(37)	Approach South	106		109	.14	.170			.13	.153	47	50
2_37_6	Fla.Wet(37)	Go Around	158		158	.13	.162			.12	.165	45	43
2_37_3b	Fla.Wet(37)	Approach East	92		100	.14	.170			.13	.161	46	37
3_49_3a	Den Inc.(49)	Approach East	34	42	N	.11	.12	.11	.12	.09	.098	10	16
3_49_3b	Den Inc.(49)	Approach North	35	35	35	.14	.164	.14	.17	.12	.142	20	17
3_51_1	Den Inc.(51)	Takeoff North	31	31	31	.13	.137	.14	.178	.14	.170	18	18
3_51_2	Den Inc.(51)	Takeoff East	76	77	82	.13	.158	.14	.196	.14	.200	23	20
3_51_3a	Den Inc.(51)	0 Approach	97		105	.14	.169			.13	.139	21	15
3_51_3b	Den Inc.(51)	45 Approach	101		110	.14	.179			.14	.183	24	17
3_51_3c	Den Inc.(51)	90 Approach	104		104	.14	.179			.13	.154	27	24
3_51_3d	Den Inc.(51)	135 Approach	100, 101	147, 106	153, 45	.13	.143	.13	.156	.11	.125	24	36
3_51_3e	Den Inc.(51)	270 Approach	102		106	.13	.169			.13	.147	20	32
3_51_3f	Den Inc.(51)	315 Approach	58		59	.16	.204			.16	.197	14	22
4_36_1	Den Stab(36)	Takeoff East	N	32	33			.16	.215	.16	.257	4	4
4_36_1er	Den Stab(36)	Takeoff East	32 (1)		33	.14	.200			.16	.257	19	19
4_36_3	Den Stab(36)	Approach East	N	N	29					.12	.144	4	4
4_36_3er	Den Stab(36)	Approach East	26 (1)		29	.14	.205			.12	.144	19	19
5_40_2	Den Dry(40)	Takeoff West	22 (2)	76	78			.12	.131	.14	.190	0	-10
5_40_2er	Den Dry(40)	Takeoff West	26 (3)		78	.14	.185			.14	.190	10	0
5_40_3	Den Dry(40)	Approach North	42	72	104	.14	.185	.13	.177	.14	.190	-4	-10
5_40_3er	Den Dry(40)	Approach North	48		104	.14	.192			.14	.190	6	0
5_40_6	Den Dry(40)	Go Around N.	N	68	155			.12	.134	.14	.180	-4	-10
5_40_6er	Den Dry(40)	Go Around N.	N (4)		155					.14	.180	6	0
5_45_3	Den Dry(45)	Approach North	N	N	72					.12	.133	-11	-11
5_45_3er	Den Dry(45)	Approach North	N (5)		72					.12	.133	0	0
6_14_3a	Fla Asy(14)	0 Approach	45		46	.11	.118			.12	.131	51	44
6_14_3b	Fla Asy(14)	45 Approach	52, NU		52	.14	.176			.13	.180	47	49
6_14_3c	Fla Asy(14)	90 Approach	51, NU	51, NU	N	.13	.158	.13	.144	.09	.102	15	22
6_14_3d	Fla Asy(14)	180 Approach	31	31	26	.17	.204	.16	.204	.12	.131	34	22
6_14_3e	Fla Asy(14)	225 Approach	59		59	.14	.175			.13	.184	47	48
6_14_3f	Fla Asy(14)	270 Approach	93	96	88	.13	.162	.12	.137	.13	.155	43	47
6_14_3g	Fla Asy(14)	315 Approach	72	81	N	.12	.126	.12	.155	.09	.11	43	46
7_27_1	Mont GF(27)	Takeoff West	N	39	39			.12	.140	.12	.137	20	21
7_27_1lc	Mont GF(27)	Takeoff West	32 (6)		32	.14	.183			.13	.165	20	21
7_27_3	Mont GF(27)	Approach West	49	95	95	.15	.180	.14	.176	.14	.184	20	21

N= No Alert NU= Nuisance Alert The “No Clutter” cases include Radar system noise. TW, HW= Tail/Head Wind

1. Refl. increased by 15 dBZ. Limit at 28 dBZ
2. Detected after Takeoff, 642' Alt.
3. Refl. increased by 10 dBZ. Limit at 17 dBZ detected after Takeoff, 546' Alt.
4. Refl. increased by 10 dBZ. Limit at 17 dBZ
5. Refl. increased by 11 dBZ. Limit at 5 dBZ
6. Run with lower clutter airport (Orlando)

5.0 Radar Simulation Test Results

5.1 Summary Performance Results

Table 4.3 shows the results for all of the simulation runs performed. There are three types of simulations performed: clutter, no clutter, and truth. Clutter simulates what a radar would see in the real environment and truth represents what is actually in the TASS dataset along the radar line of sight. No clutter is a run without the ground clutter being mixed with the information from the TASS dataset. The column of advance warning time shows the time that an alert first appeared on the display. The average FBAR is the largest value of all the icons shown at the time of first alert. The peak value is obtained by manually searching inside of the icon(s) to locate the highest value. All FBAR values are 1 km averaged. The final two columns show the reflectivity at the location of peak headwind or tailwind. The results for advanced warning time show a minimum of 22 seconds with values up to 158 seconds. The cases that are very dry (i.e. low reflectivity: 5_40, and 5_45) or small (4_36) are not detected. Most cases detect the hazard with the same warning time as the truth cases did; however, some cases did not detect a hazard where the truth clearly shows a hazard. Some of the results have been included as PPI plots in appendix B. Out of all of the cases there are only two nuisance alerts.

Appendix B contains PPI plots for selected simulation runs. Each plot is taken at the time of first alert and contains both hazard and the wind velocity displays. The plots have the runway outlined in black and the flight path denoted by white dots. The runway location is labeled on each plot. A modified grayscale zebra shading pattern is used in order to retain the information contained in the original color PPI plots. The hazardous windshear and tailwinds are denoted by darker shades. Appendix C gives more specific analysis of some of the PPI plots by comparing the hazard and velocity along a constant azimuth as a function of range in front of the aircraft position. The line plots show the comparison of radar simulation results and truth. In addition, the reflectivity is plotted to help explain why simulation and truth differ.

5.2 Analysis of Each Simulation Run

5.2.1 ILS Landing Approach Cases

<u>Dallas Fort Worth Accident Case, Wet Microburst, Rain and Hail</u>

Case 1_11_3

Figure B.1 shows a windshear threat at 6 km away from the aircraft position. This corresponds to an advance warning time of approximately 104 seconds. The hazard is represented by two icons with a peak 1 km F- factor of 0.16. The wind velocity plot shows the distance of peak-to-peak velocity of approximately 3 km. Figure C.1 shows good agreement for the velocity with the hazard agreeing well on the near side of the event.

Florida NASA Research Flight, Wet Microburst

Case 2_37_3a

Figure B.2 shows the windshear threat at 7.5 km away from the aircraft position with a 1 km average F-factor of 0.14. Figure C.2 shows the relatively high levels of reflectivity well in advance of the hazard. The clutter runs show an overestimate of the peak hazard level.

Case 2_37_3b

Figure B.3 shows two regions of hazard of equal value. The approximate distance from peak headwind to tailwind is 3 km. The icons are located at 7 km away from the aircraft on first alert. The comparison of Figure B.4 with hazard and wind velocity for case 2_37_3b shows the difference of adding clutter to a simulation. The region of hazard is smaller in the truth case and the two separate icons with the clutter case are spread farther apart. Figure C.3 shows the clutter with a higher peak hazard than the truth.

Denver Incident Case, Multiple Microburst

Case 3_49_3a

Figure B.5 shows one small area of hazard at 3 km away from the aircraft position. The value for the F-factor is 0.11 and is situated to the right of the aircraft landing path. The velocity plot shows that the icon is located over nearby Interstate 95.

Case 3_49_3b

Figure B.6 displays two hazard icons. The larger is about 2 km from the aircraft and along the flight path while the other is off the right at 2.5 km from the aircraft. The magnitude of both icons is in the "must alert" category. The velocity plot shows a well defined transition from headwind to tailwind at 3 km along the flight path. The location of peak hazard in Figure C.4 displays good agreement with the hazard lying between two reflectivity peaks.

Case 3_51_3a

Figure B.7 gives an example of an alert detected at a long range from the aircraft. The single icon is along the path and at 7.5 km from the aircraft.

Case 3_51_3b

The advance warning time differs by only 9 seconds between the clutter and truth runs as shown in Table 4.3. The FBAR values also compare very well.

Case 3_51_3c

Figure B.8 shows an array of three icons with hazards ranging from 0.12 to 0.14. The closer two icons are at 4.5 km with one being on the flight path. The farther most hazardous icon is also along the flight path and is at the 7 km range. The region between the two icons on the flight path shows a region of performance increasing windshear (not a hazard). Figure B.9 shows the truth hazard. The truth differs from the simulated radar by the addition of a new region of hazard at 9.5 km and the coalescing of the two closer icons at 4.5 km. Also the magnitude of the hazard at 7 km is reduced and the inner icon is no longer along the flight path. The clutter result of the hazard at 7 km ahead of the aircraft compares well with the truth in Figure C.5. The disagreement in the hazard at 4.5 km is due to the radar splitting the hazard into two regions. The magnitude is the same as shown in Figure B.8 but the location is displaced.

Case 3_51_3d

This case also has both simulated radar returns and truth plots. Figure B.10 displays three icons of magnitude 0.13. Of the closer two icons only the smaller is actually an alert since the larger has only one bounding box (on the next scan the region becomes an alert). The range to these hazard regions is 3 km. Also at 7 km a region of hazardous windshear exists. Figure B.11 shows good agreement between simulated radar and truth. The difference between the two is primarily the larger size of the alerting region beyond the runway for the truth case. Figure C.6 shows two hazard regions. The nearfield hazard is over estimated whereas the farfield is not only under estimated but also much smaller which is consistent with the PPI plots of Figures B.10 and B.11.

Case 3_51_3e

The agreement in warning time and FBAR values are very good as shown in Table 4.3.

Case 3_51_3f

Figure B.12 shows three icons ranging from 0.12 near the runway threshold to 0.18 at 3 km from the aircraft. The large area of hazard has a peak hazard factor of 0.17 and lies along the aircraft flight path. There exists 2 km of performance increasing windshear prior to encountering the hazardous region. The velocity plot clearly shows a change from headwind to tailwind starting at about 3.5 km range. Figure C.7 show very good agreement in the location of the peak hazard.

Denver Stable Layer, Warm Microburst

Case 4_36_3

No detection of a hazard in the original data.

Case 4_36_3er

Figure B.13 shows a very small region of hazardous windshear with a

magnitude is 0.14 at 1.5 km from the aircraft position. Figure B.14 shows the true hazard condition. The truth shows good agreement to the radar simulation. Figure C.8 shows the relative comparison of the hazard levels. The peak hazard level is larger than the truth with the width being in good agreement.

Denver Very Dry Microburst

Case 5_40_3

No detection of a hazard in the original data.

Case 5_40_3er

Figure B.15 shows two rectangular icons at 2 km in front of the aircraft. The icons are aligned along the flight path with the more severe at 0.14 magnitude. Figure B.16 shows the truth for this case. The size of the truth is considerably larger than the radar simulation and also a larger value (0.15). The hazard is significantly larger than the radar simulation as seen in Figure C.9. The reason for the discrepancy is due to the small region of reflectivity above 0 dBZ.

Case 5_45_3

No detection of a hazard in the original data.

Case 5_45_3er

No detection of a hazard in the enhanced data.

Derived Florida Sounding, Highly Asymmetric Microburst

Case 6_14_3a

Figure B.17 displays three small hazardous regions. The magnitude ranging from 0.11 to 0.13. The range to the closest alert box is 3 km and is on the flight path. The closest and most severe hazard region has not yet become an alert box. Figure C.10 shows excellent agreement for both hazard and velocity.

Case 6_14_3b

Figure B.18 shows two hazardous regions of 0.13 magnitude with one being on the flight path and at 3 km range from the aircraft position. Figure B.19 shows the truth for this case and displays only one icon. This icon is the same magnitude size and location as the radar simulation figure. The truth figure shows the edge of the windshear data set at rages from 7 to 10 km. Figure C.11 displays very good agreement for both hazard and velocity.

Case 6_14_3c

This case is a nuisance alert. The region of peak hazard is only 0.09 while the radar returns 0.13 which is above the "must alert" threshold.

Case 6_14_3d

The peak hazard is over-predicted by 25 percent. The time of warning is at 31

seconds from encounter.

Case 6_14_3e

Figure B.20 shows numerous regions of hazardous windshear. The area to the left of the aircraft and at 2km range contains hazards of magnitude 0.12. The largest icon lies along the flight path at 4 km range and is 0.14 in magnitude. The most severe icon is at 3.5 km to the right of the path and a value of 0.18. The peak hazard as shown in Figure C.12 displays very good agreement. The radar shows a departure from the truth on the far side of the hazard.

Case 6_14_3f

The comparison of warning time and FBAR values shows good agreement in Table 4.3

Case 6_14_3g

This is a nuisance alert. The FBAR values as shown in Table 4.3 display an over estimate of the hazard such that the level is boosted from above the "must alert" threshold.

Adjusted Montana Sounding, Gust Front

Case 7_27_3

Figure B.21 shows only one icon, but it is along the flight path and has a magnitude of 0.15 at 3 km from the aircraft position. The hazard is shown to have good agreement in both range and magnitude in Figure C.13.

5.2.2 Takeoff Cases

Dallas Fort Worth Accident Case, Wet Microburst, Rain and Hail

Case 1_11_2

Figure B.22 displays a very large area of hazardous windshear of 0.15 magnitude. The icon is located at 5.5 km from the aircraft and 3 km from the end of the runway. Also the velocity gradient is clearly shown.

Denver Incident Case, Multiple Microburst

Case 3_51_1

Figure B.23 shows a rectangular icon at the departure end of the runway with a value of 0.13. There are also icons to the left and the right of this icon at about the same range.

Case 3_51_2

Figure B.24 displays three icons with one along the flight path. The closer icon is at 3.5 km but is off to the left. The icon along the path is at 5.5 km or 3 km from the end of the runway and has a magnitude of 0.11. Figure B.25 shows the truth for this case. Larger magnitudes are shown in both primary regions with the outer region encompassing the two outer icons from the radar simulation. The differential of magnitude is 0.03 from the truth to the radar simulation.

Denver Stable Layer, Warm Microburst

Case 4_36_1

No detection of a hazard in the original data.

Case 4_36_1er

Figure B.26 shows a single icon at the departure end of the runway elongated along the runway direction and having a magnitude of 0.15. Figure B.27 displays the truth for this case. The truth shows a larger region of hazardous windshear but at the same location.

Denver Very Dry Microburst

Case 5_40_2

Table 4.3 shows the hazard being detected after takeoff with only 22 seconds warning time. The truth run showed an increase in warning time by almost a minute.

Case 5_40_2er

The enhanced reflectivity doesn't significantly change the results as compared to no enhancement (Table 4.3).

Adjusted Montana Sounding, Gust Front

Case 7_27_1

No detection of a hazard in the original data.

Case 7_27_1lc

The lower clutter environment shows very good agreement with truth results (Table 4.3).

5.2.3 Go Around Cases

Florida NASA Research Flight, Wet Microburst

Case 2_37_6

Figure B.28 displays two icons at the range of the departure end of the runway or 10 km from the aircraft position. One of the icons resides at the end of the runway.

Denver Very Dry Microburst

Case 5_40_6

No detection of a hazard in the original data.

Case 5_40_6er

No detection of a hazard in the enhanced data.

6.0 Conclusion

This report described the NASA airborne windshear radar hardware, signal processing algorithms, and the experimental flight tests. The details of the radar simulation program have been explained showing how the flight data and the simulated weather data are merged to give an accurate representation of the performance of the NASA airborne windshear radar. Finally, the results of the simulation testing detailing the flight scenarios and clutter data have shown the ability of the NASA system to detect hazardous windshear.

The NASA Airborne radar system has been shown to perform extremely well in a wide range of environmental conditions and path scenarios. The ability of the system to detect hazardous windshear behind intervening rain and in areas of severe ground clutter demonstrate the strengths of the system; however, the two nuisance alerts and the inability to detect hazardous windshear in areas of extremely low reflectivity demonstrate the weaknesses of NASA Doppler radar. The alert for all cases was displayed with at least 1.5 km distance from the aircraft or approximately 30 seconds prior to penetration giving time and space to execute the proper windshear encounter procedure. The favorable comparison of truth and clutter simulation runs for a select number of cases exhibits the ability of the radar system to capture the salient details of the hazardous windshear; however, they also show that the radar detects a subset of the true hazard. This demonstrates that there may be areas of undetected hazardous windshear outside of the alert boxes. The overall result is that the NASA airborne windshear radar can detect hazardous windshear with a high degree of reliability.

7.0 References

Bowles, R. L., 1990: Reducing Windshear Risk Through Airborne Systems Technology. The 17th Congress of the ICAS, Stockholm, Sweden, 27 pp.

Britt, C. L., 1990: User Guide for an Airborne Windshear Doppler Radar Simulation (ADWRS) Program. NASA Contract NAS1-17639, Research Triangle Institute, Research Triangle Park, NC, June 1990.

Britt, C. L., 1993: Operation of the Windshear Flight Data Compression Program. RTI/4500/027-02F, Research Triangle Institute, November 1993.

Britt, C. L., and L. H. Crittenden: 1993: Operation of the Airborne Doppler Radar Quick-Look Data Analysis Program. RTI/4500/027-01F, Research Triangle Institute, November 1993.

Doviak, R. J. and D. S. Zrnic: Doppler Radar and Weather Observations. Academic Press Inc. 1984.

Harrah, S. D., E. M. Bracalente, P. R. Schaffner, and C. L. Britt, 1993: NASA's Airborne Doppler Radar for Detection of Hazardous Wind Shear: Development and Flight Testing: AIAA93-3946, AIAA Aircraft Design, Systems & Operation Meeting, Aug 11-13, 1993, Monterey, CA.

Proctor, F. H., 1987a: The Terminal Area Simulation System, Volume I: Theoretical formulation. NASA Contractor Rep. 4046, NASA, Washington, DC, 176 pp. [Available from the National Technical Information Service, Springfield, VA, 22161.]

Proctor, F. H., 1987b: The Terminal Area Simulation System, Volume II: Verification Experiments. NASA Contractor Rep 4047, NASA, Washington, DC, 112 pp. [Available from the National Technical Information Service, Springfield, VA, 22161.]

Proctor, F. H., 1988a: Numerical simulations of the 2 August 1985 DFW microburst with the three-dimensional Terminal Area Simulation System. Preprints Joint Session of 15th Conf. on Severe Local Storms and Eighth Conf. on Numerical Weather Prediction., Baltimore, Amer. Meteor. Soc., J99-J102.

Proctor, F. H., 1988b: Numerical simulations of an isolated microburst. Part I: Dynamics and structure. J. Atmos. Sci., 45, pp. 3137-3160.

Proctor, F. H., 1989: Numerical simulations of an isolated microburst. Part II: Sensitivity experiments. J. Atmos. Sci., 46, pp. 2143-2165.

Proctor, F. H., 1993: Case study of a low-reflectivity pulsating microburst: Numerical simulation of the Denver, 8 July 1989, Storm. To appear in Preprints, 17th Conference on Severe Local Storms, St. Louis, Amer. Meteor. Soc., 677-680.

Proctor, F. H. and R. L. Bowles, 1992: Three-dimensional simulation of the Denver 11 July 1988 microburst-producing storm. Meteorol. and Atmos. Phys., 47., 107-124.

Proctor, F. H., E. M. Bracalente, S. D. Harrah, G. F. Switzer, and C. L. Britt, 1995: Simulation of the 1994 Charlotte Microburst with Look-Ahead Windshear Radar. 27th Conf. on Radar Meteorology, Vail, CO, Amer. Meteor. Soc., 530-532.

Switzer, G. F.,F. H. Proctor, D. A. Hinton, and J. V. Aanstoos, 1993: Windshear Database for Forward-Looking Systems Certification. NASA TM-109012, November 1993.

Appendix A

Selected Clutter Plan Position Indicator Diagrams

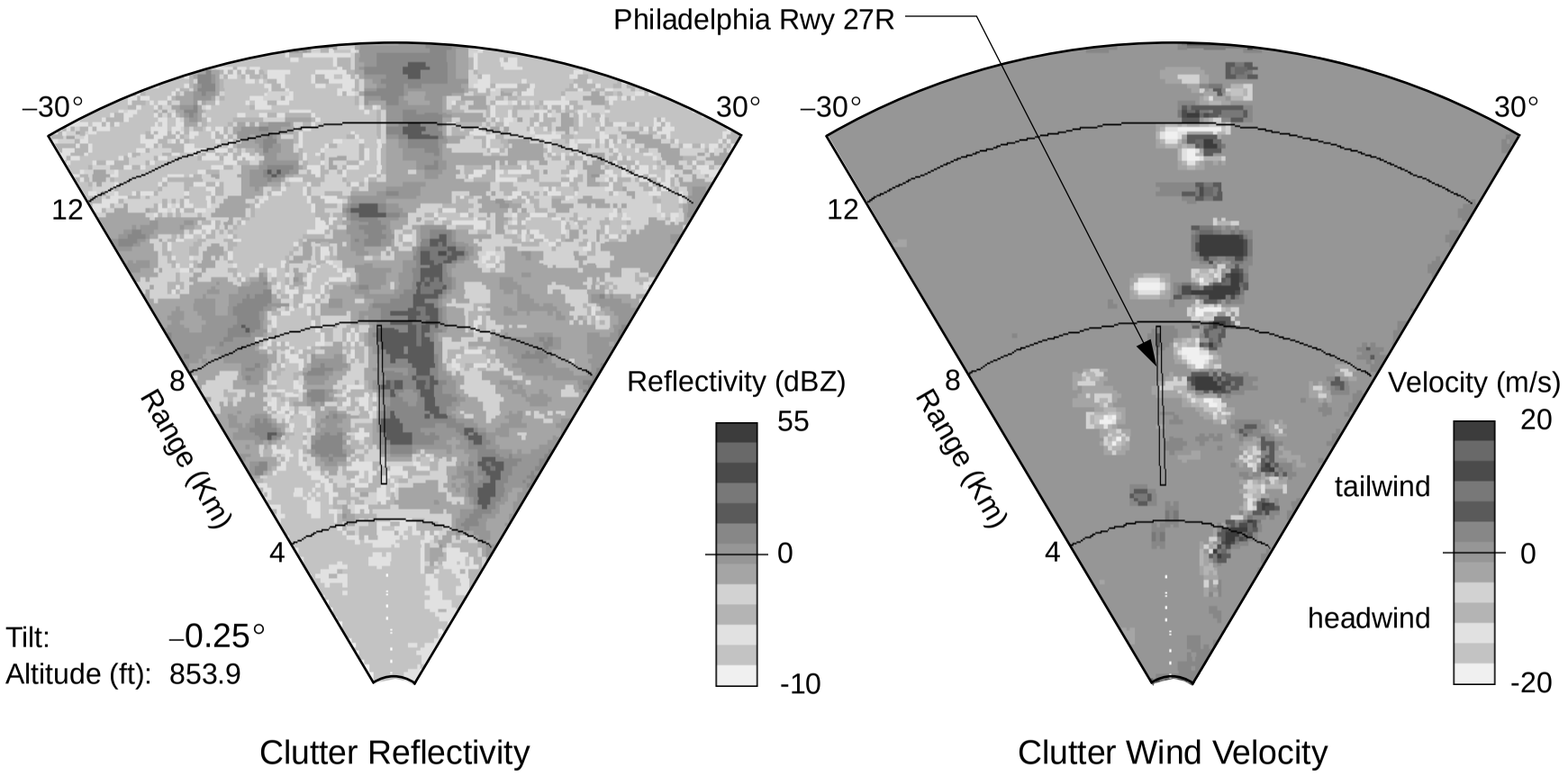

Figure A.1 Clutter reflectivity and wind velocity for Philadelphia runway 27R. The wind velocity plot shows the traffic clutter from nearby Interstate 95. The white dots indicate the aircraft flight path.

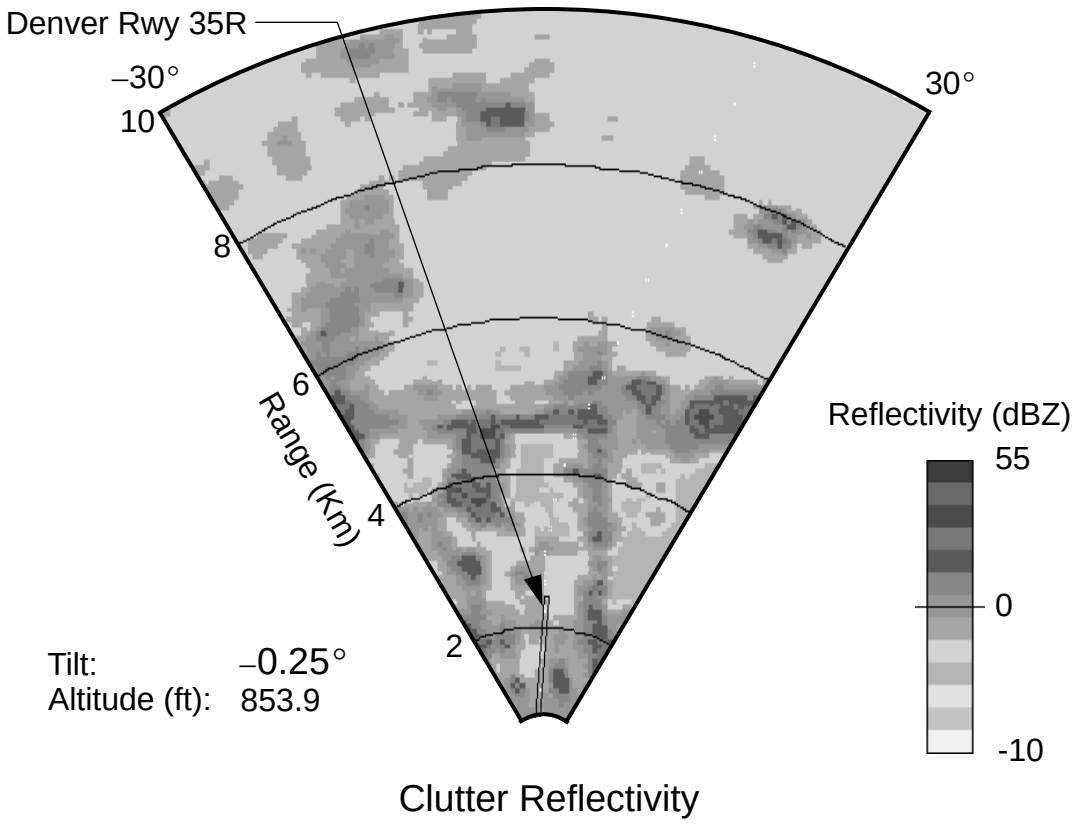

Figure A.2 Clutter reflectivity for Denver runway 35R. The white dots indicate the aircraft flight path.

Appendix B

Selected Plan Position Indicator Diagrams

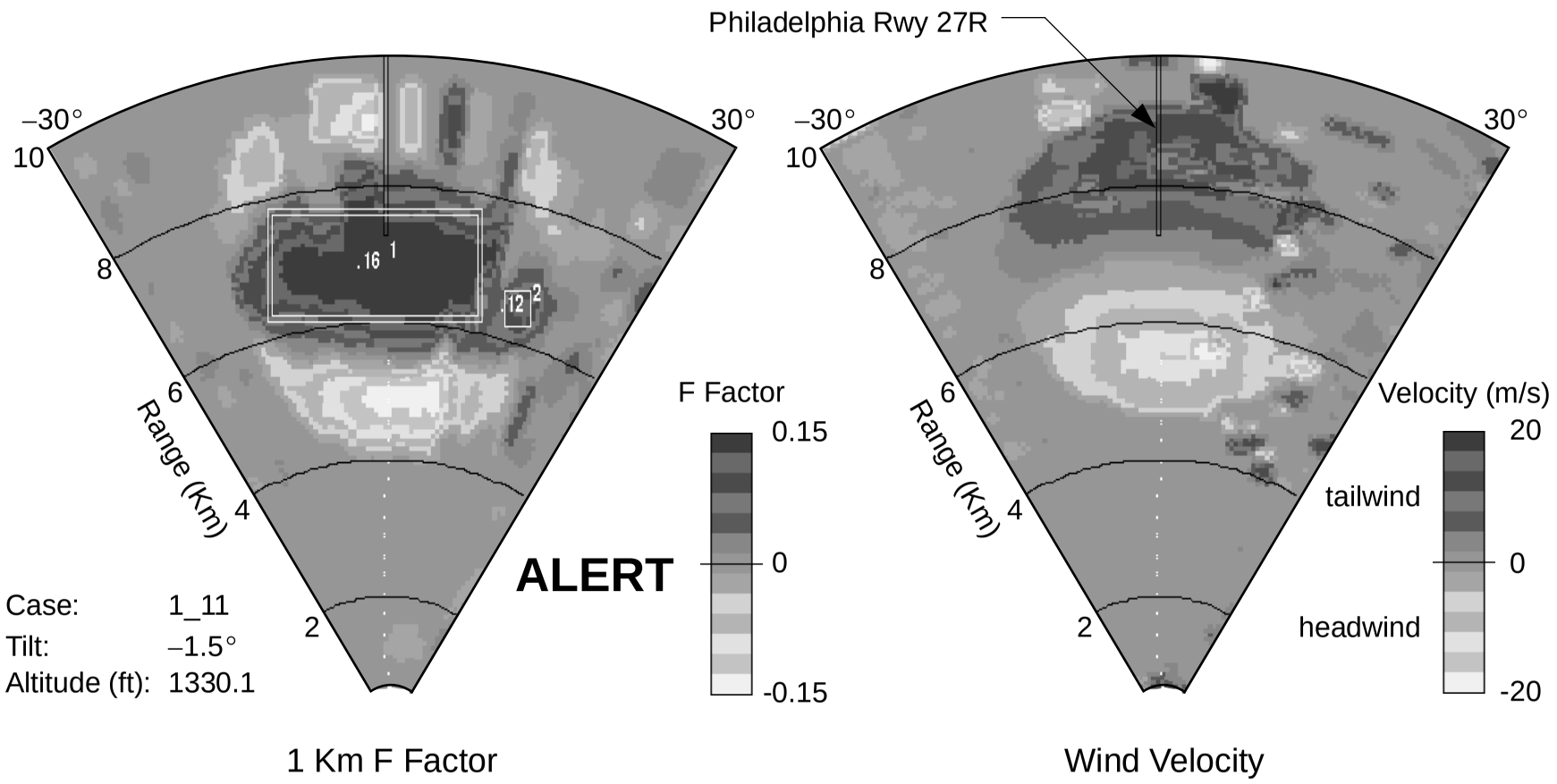

Figure B.1 Hazard and wind velocity for case 1_11_3

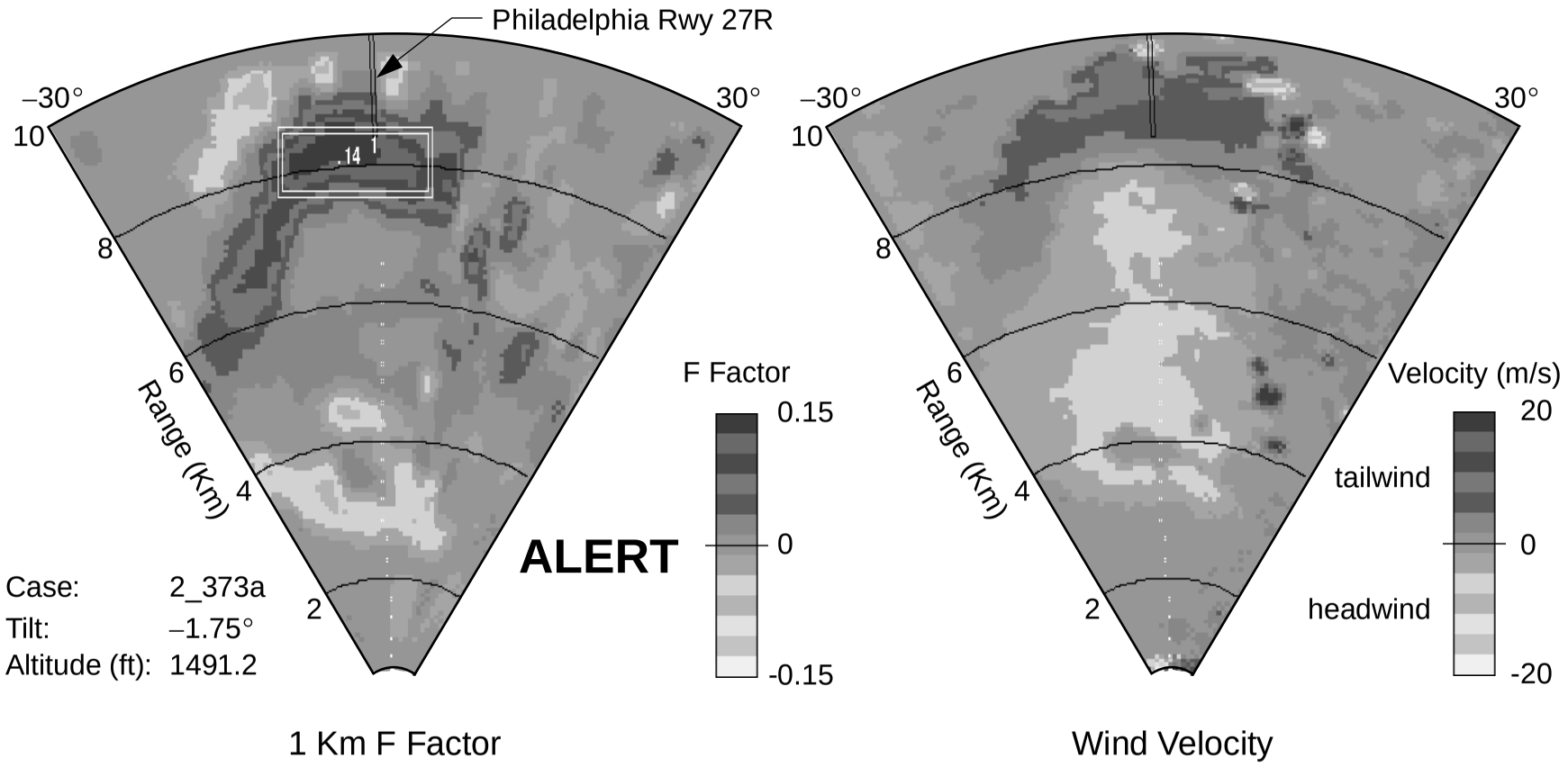

Figure B.2 Hazard and wind velocity for case 2_37_3a

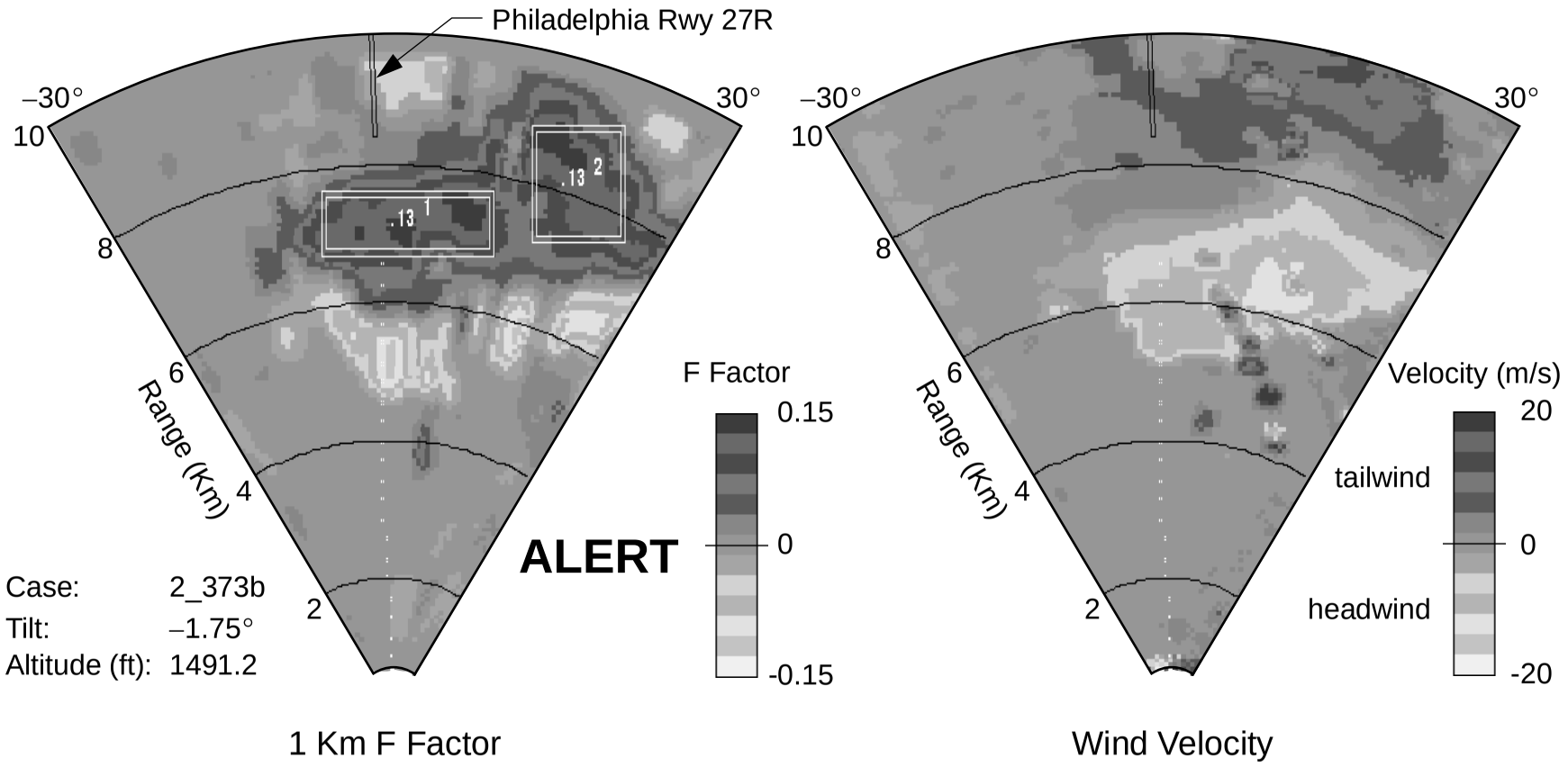

Figure B.3 Hazard and wind velocity for case 2_37_3b

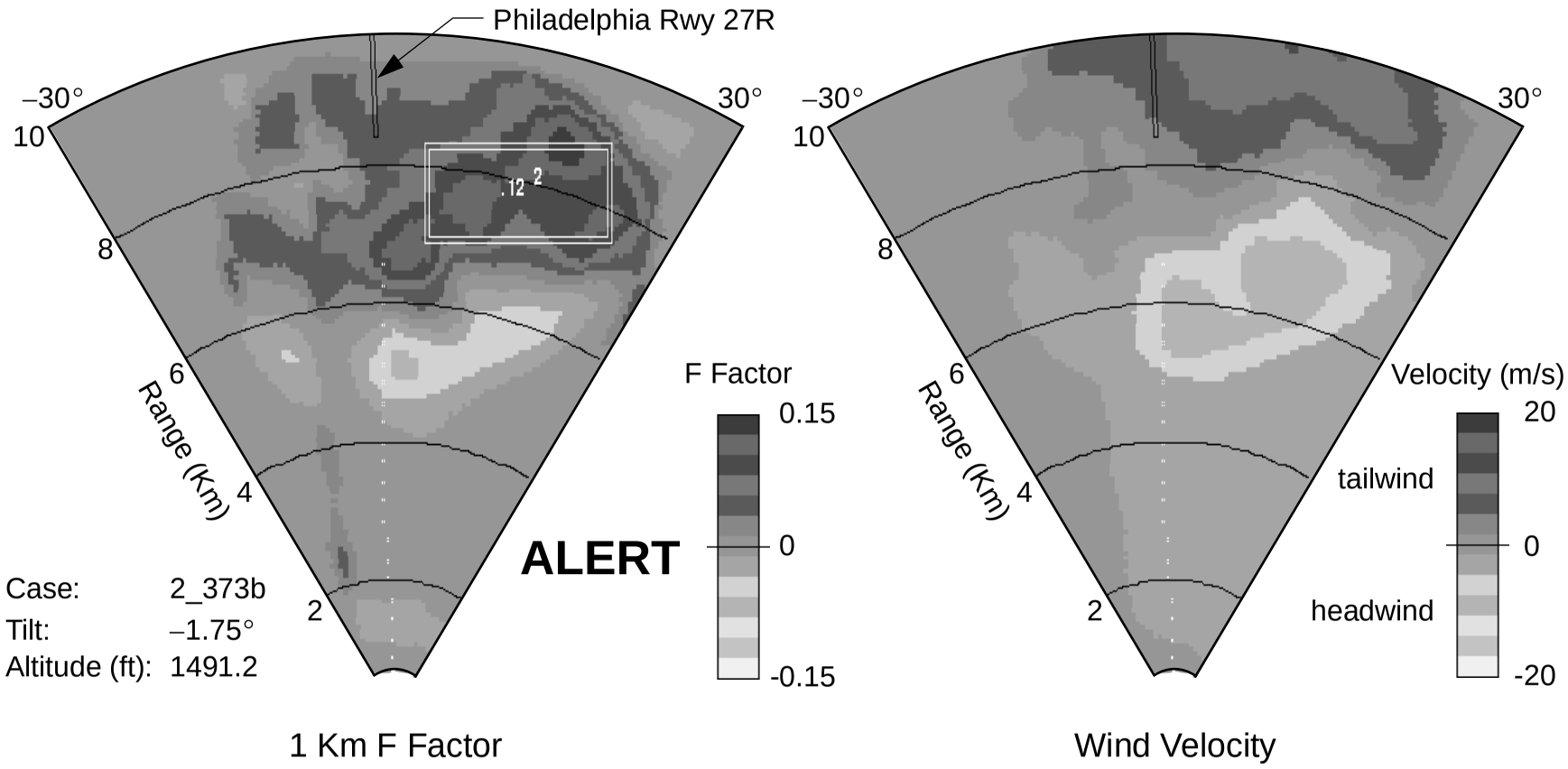

Figure B.4 True hazard and wind velocity for case 2_37_3b

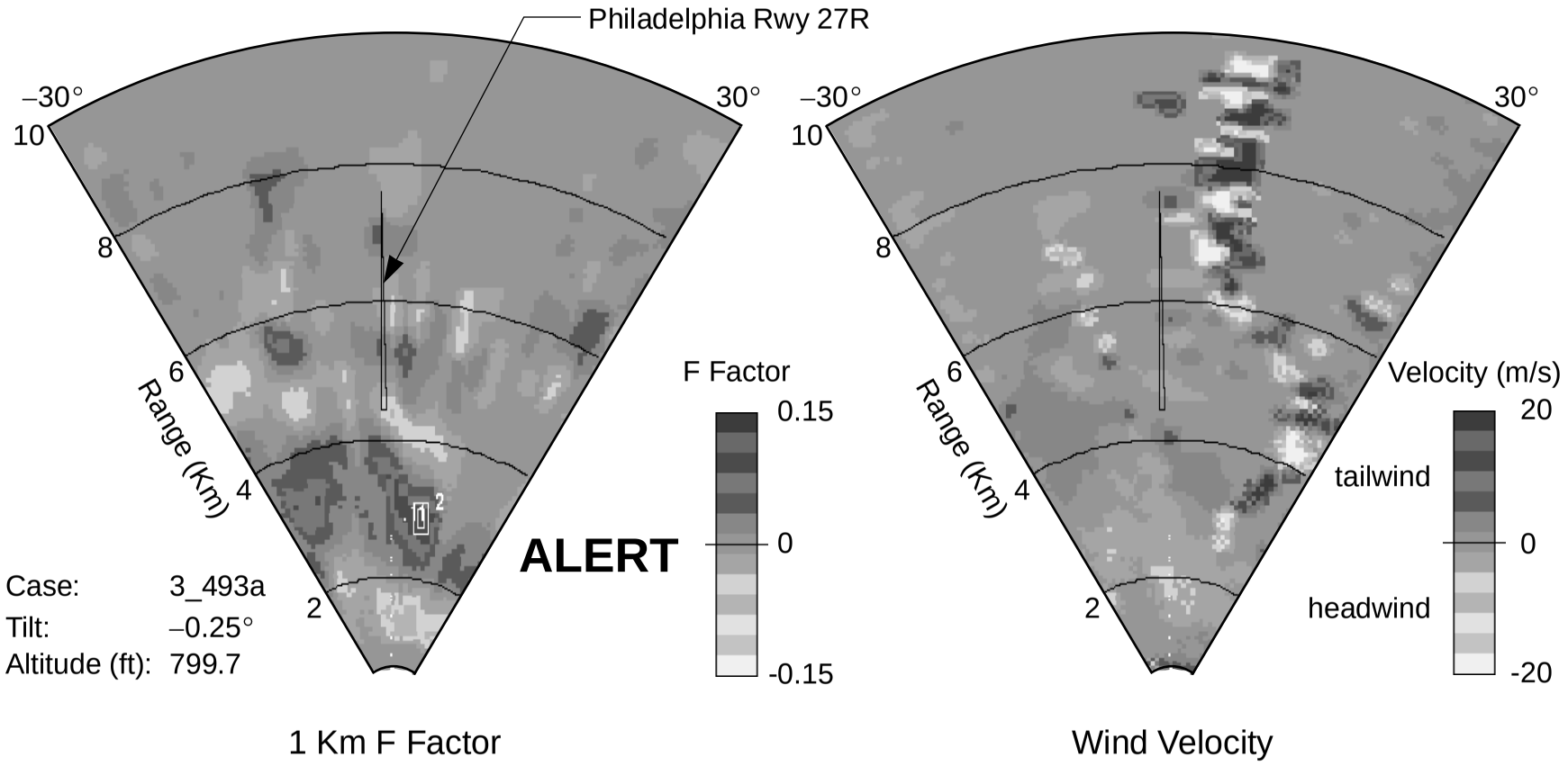

Figure B.5 Hazard and wind velocity for case 3_49_3a

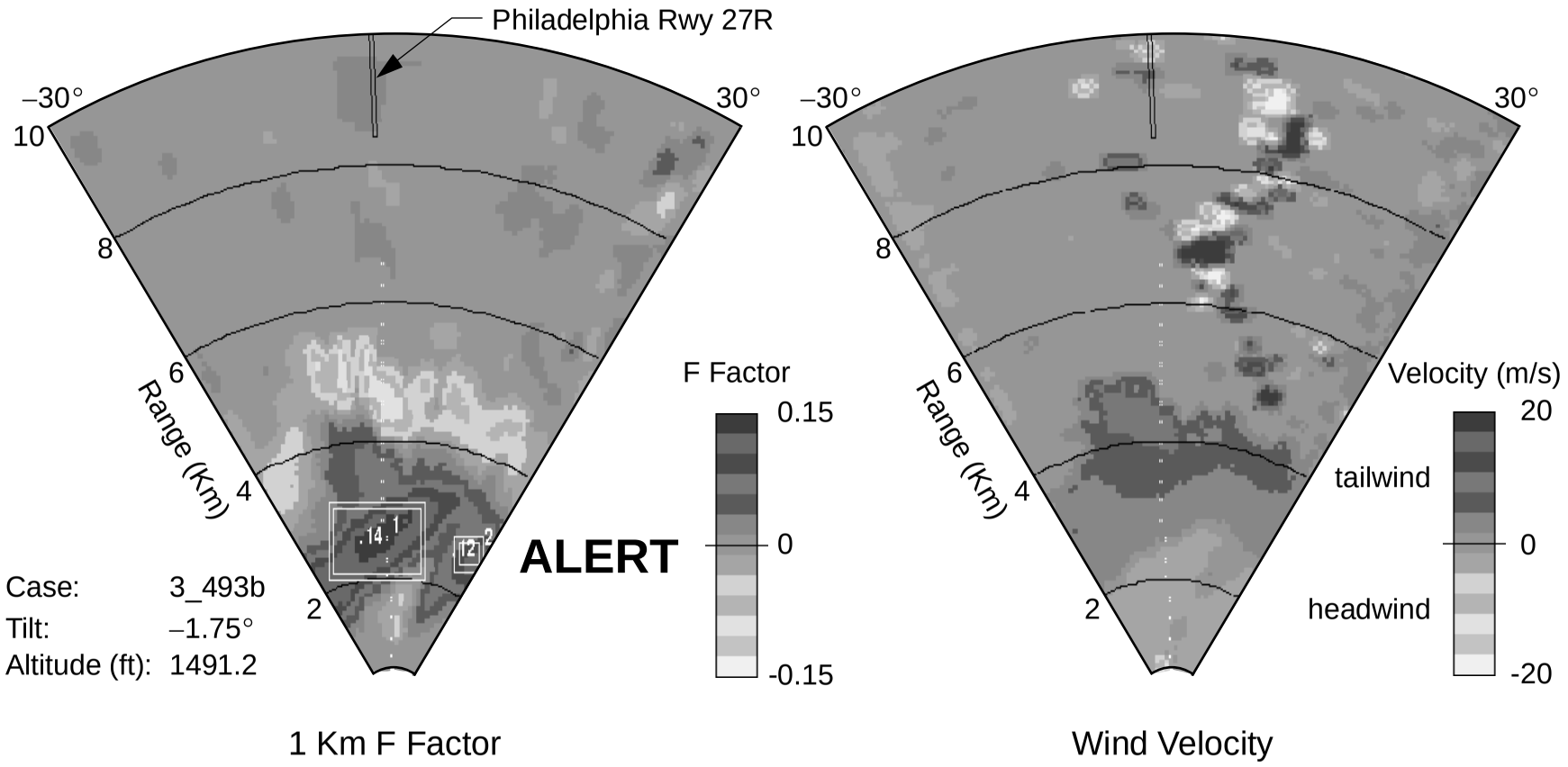

Figure B.6 Hazard and wind velocity for case 3_49_3b

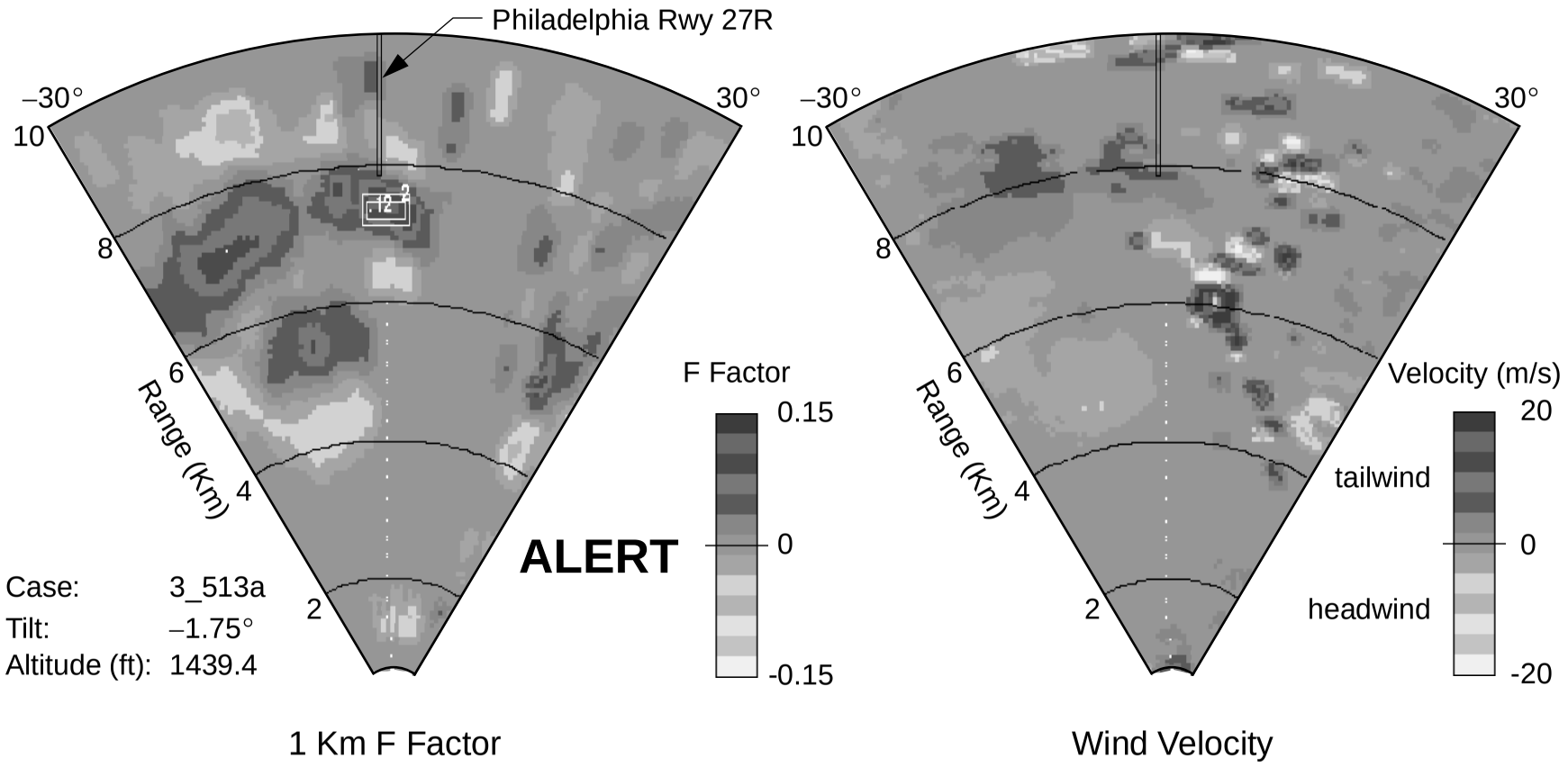

Figure B.7 Hazard and wind velocity for case 3_51_3a

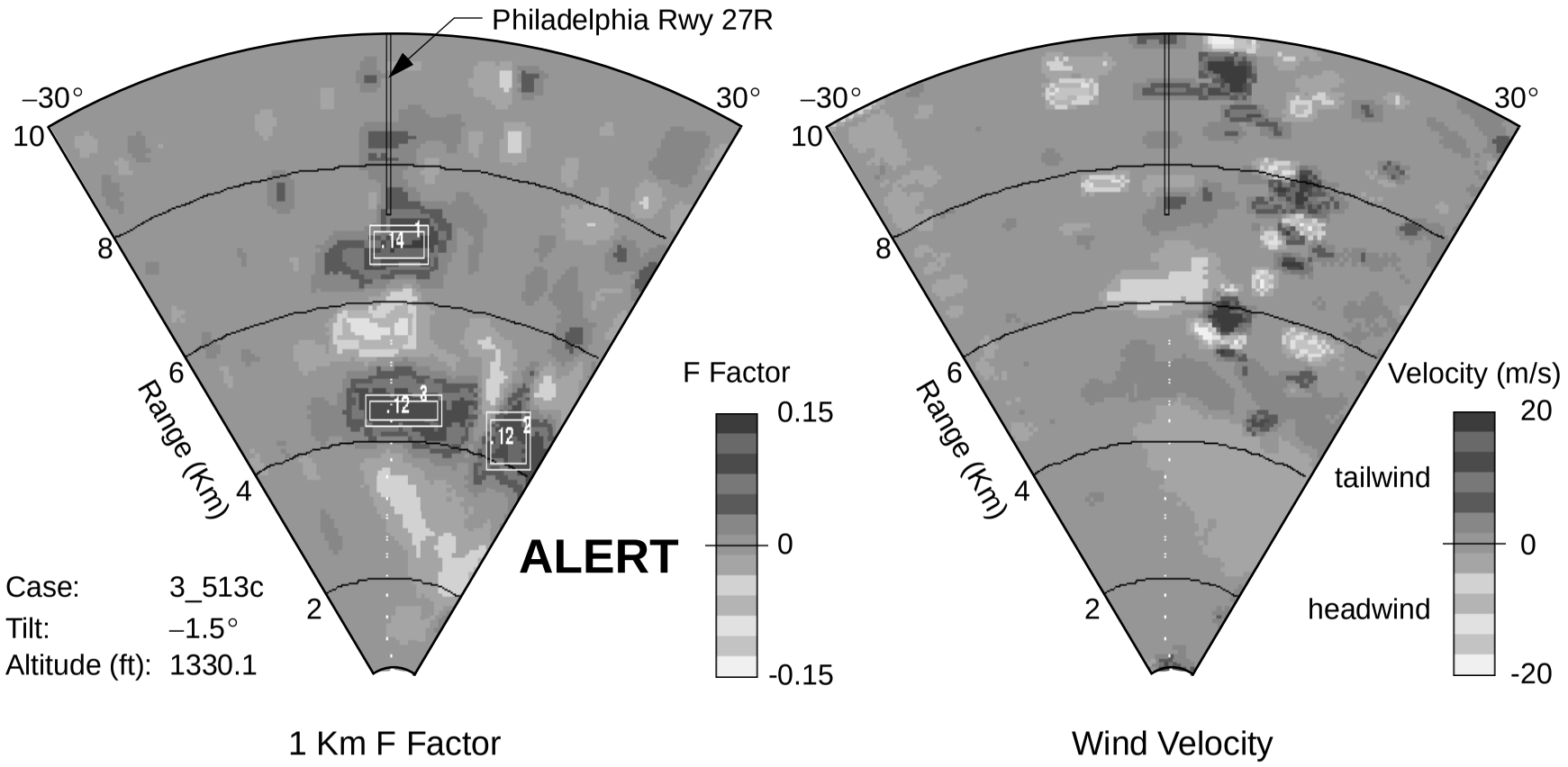

Figure B.8 Hazard and wind velocity for case 3_51_3c

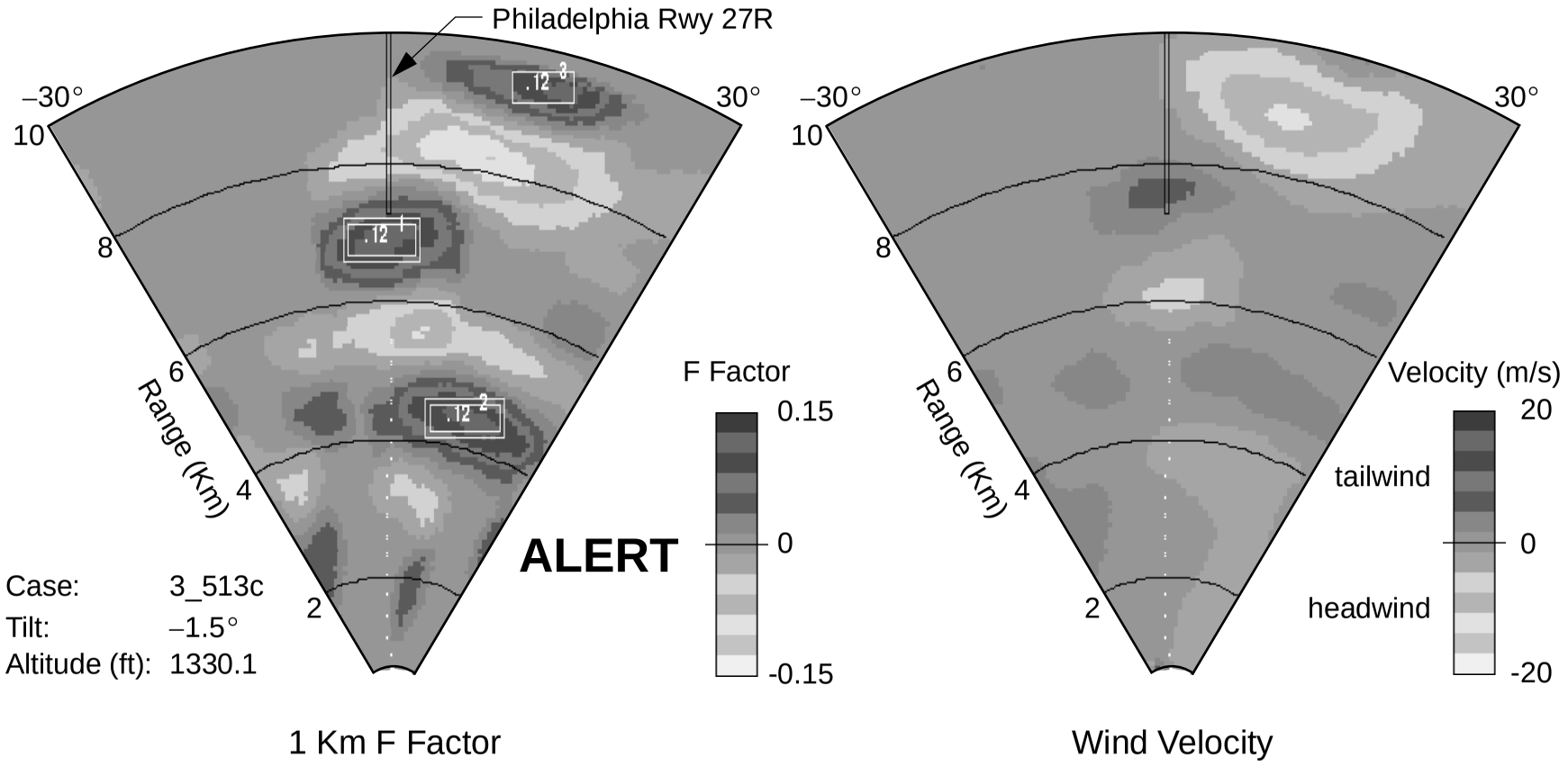

Figure B.9 True hazard and wind velocity for case 3_51_3c

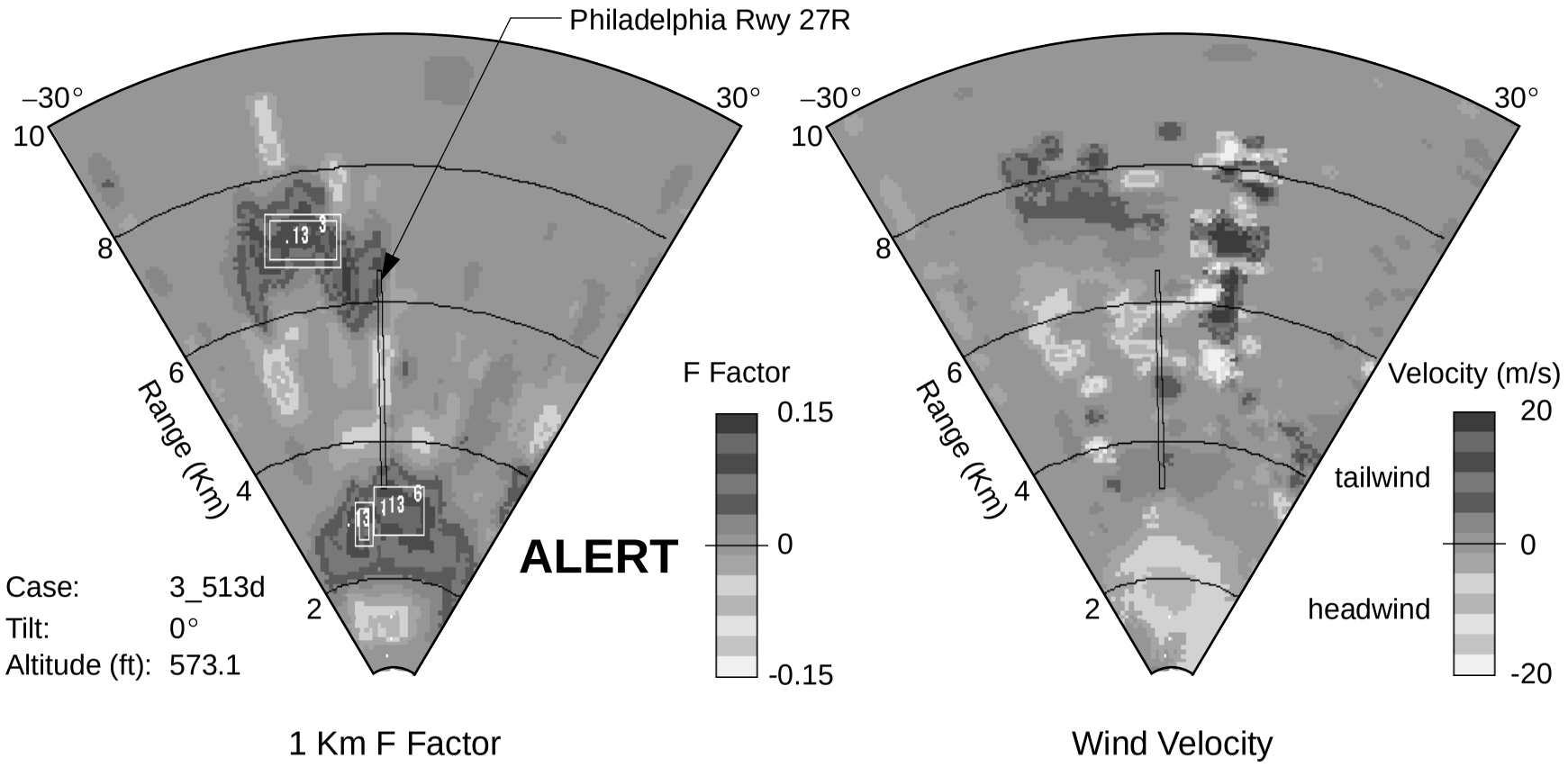

Figure B.10 Hazard and wind velocity for case 3_51_3d

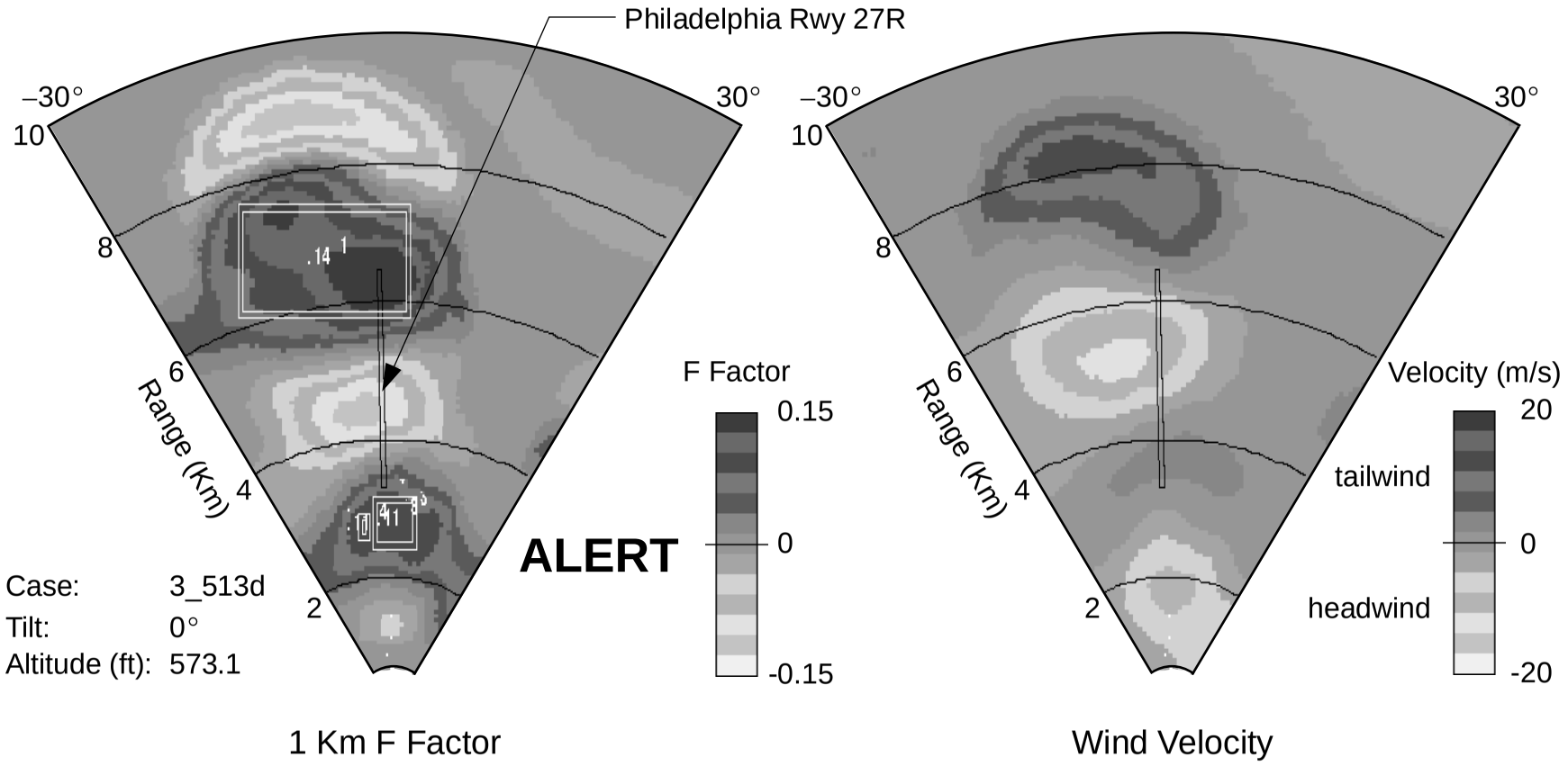

Figure B.11 True hazard and wind velocity for case 3_51_3d

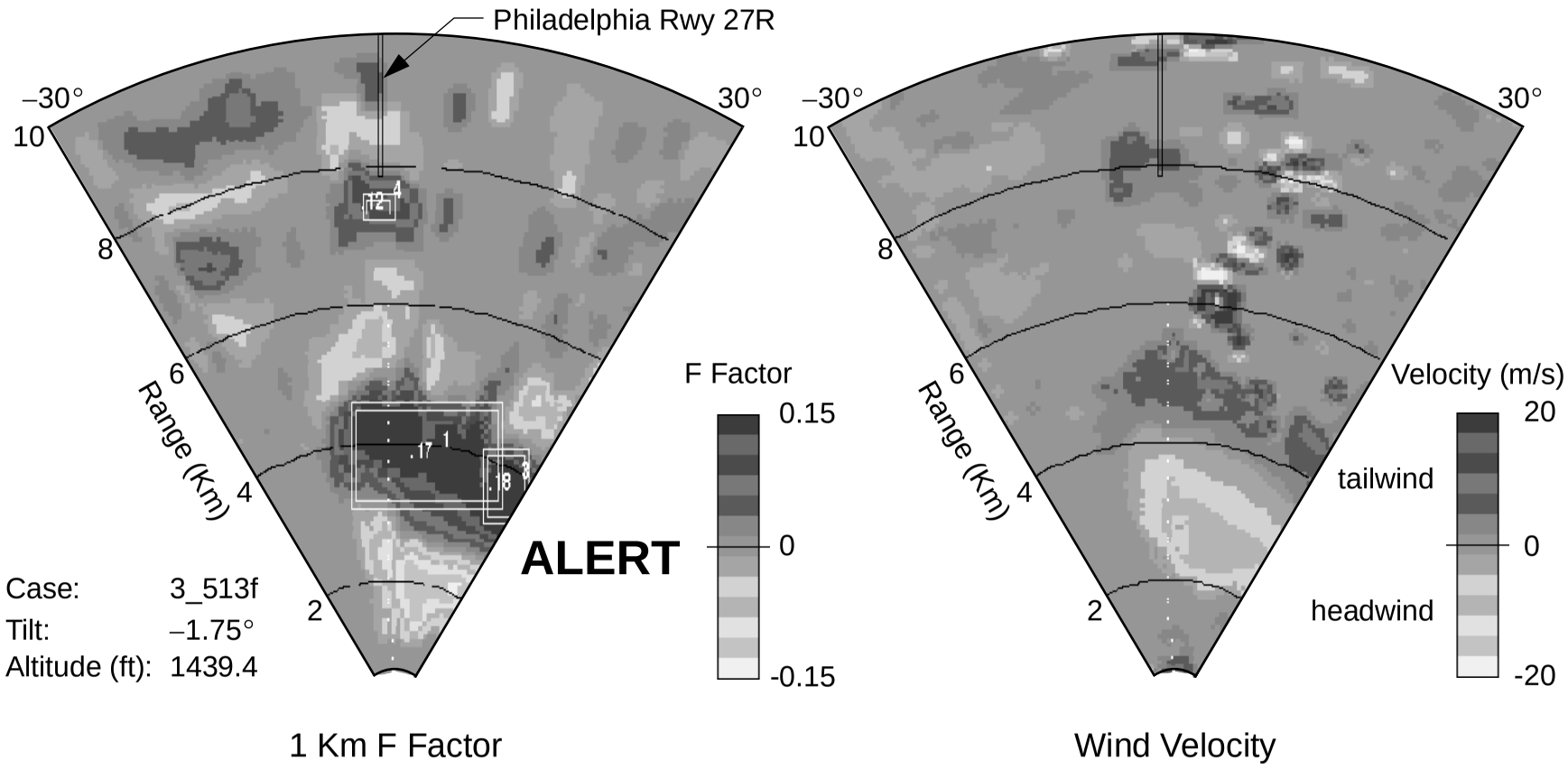

Figure B.12 Hazard and wind velocity for case 3_51_3f

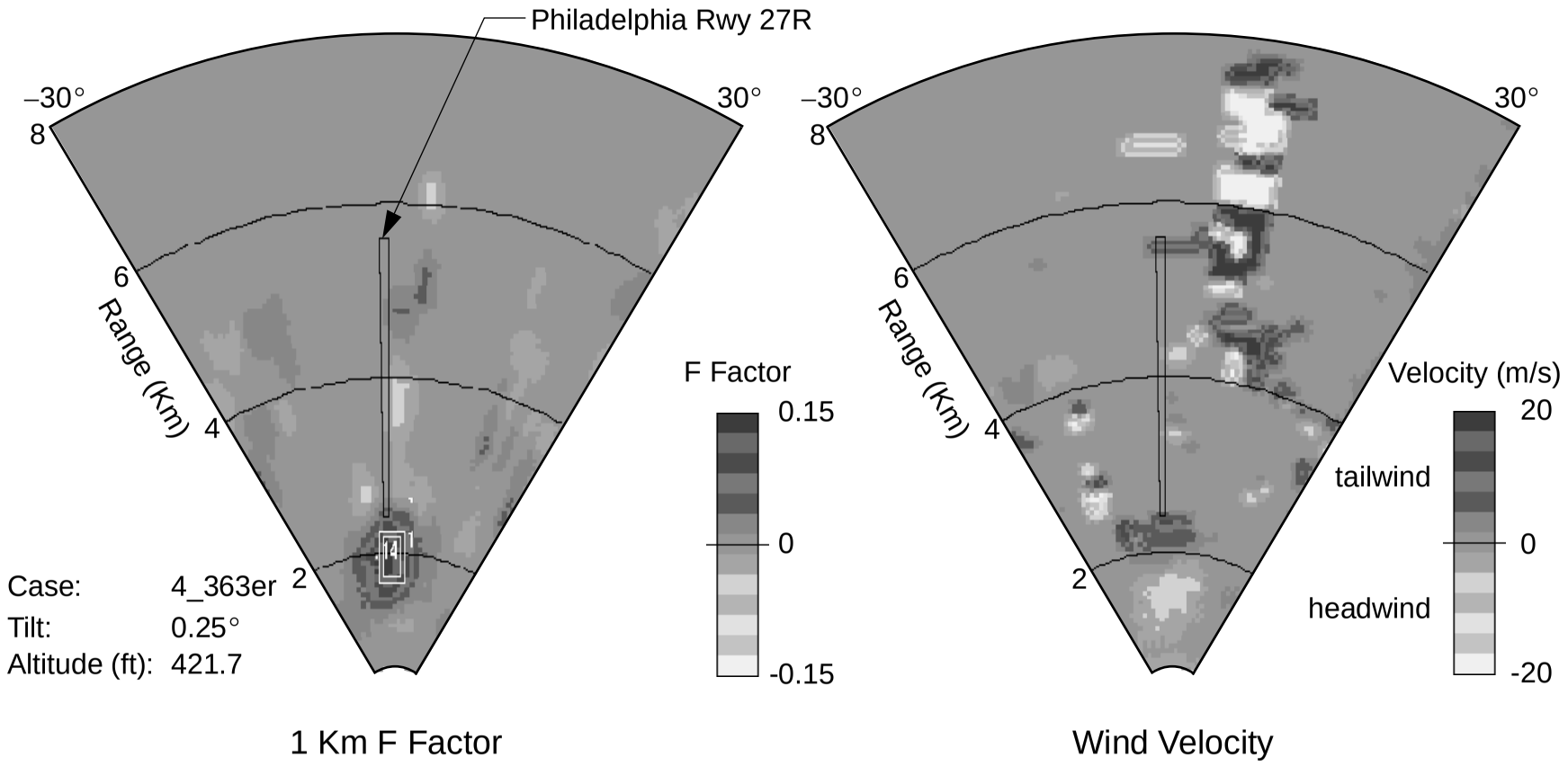

Figure B.13 Hazard and wind velocity for case 4_36_3er

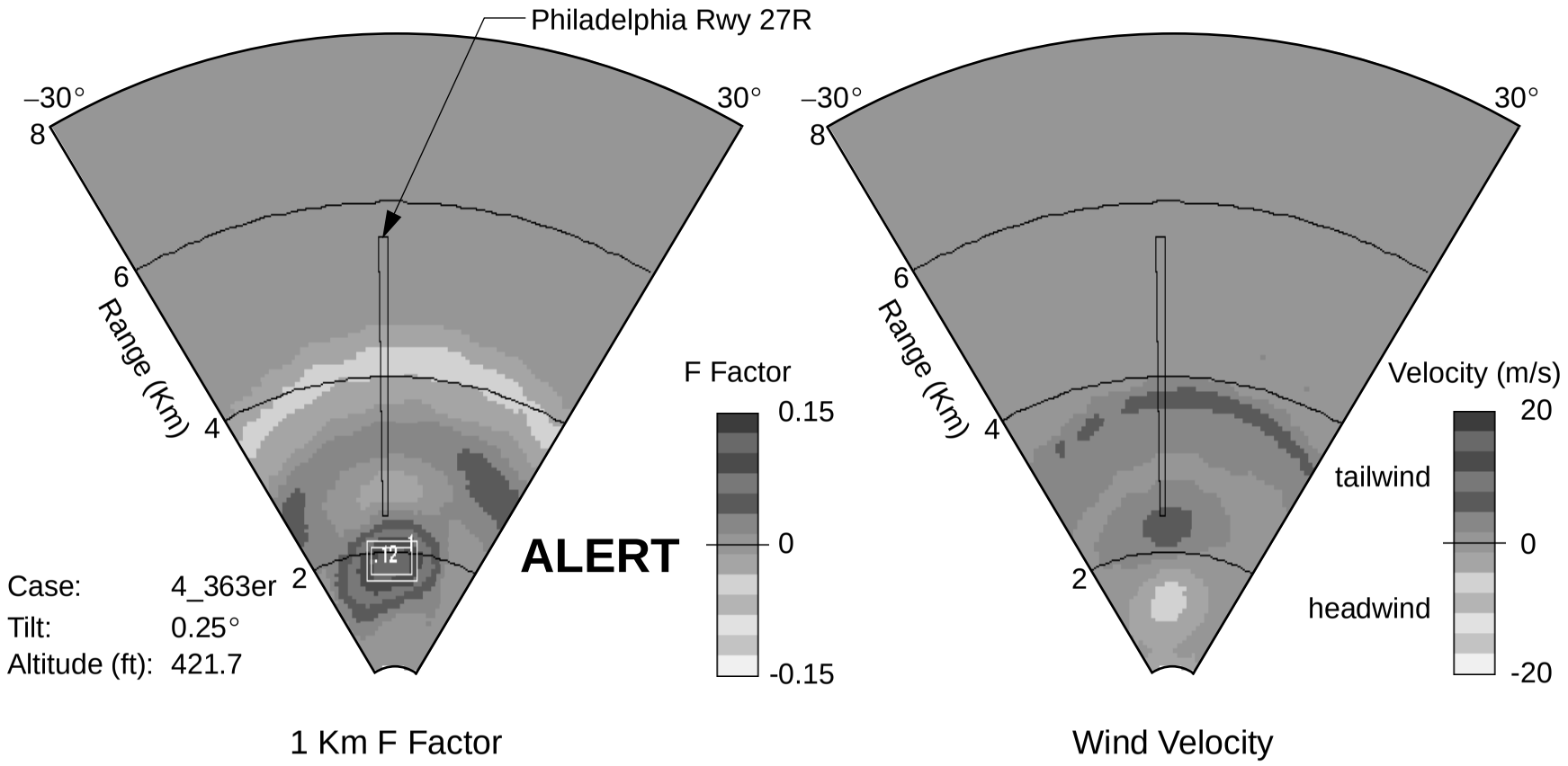

Figure B.14 True hazard and wind velocity for case 4_36_3er

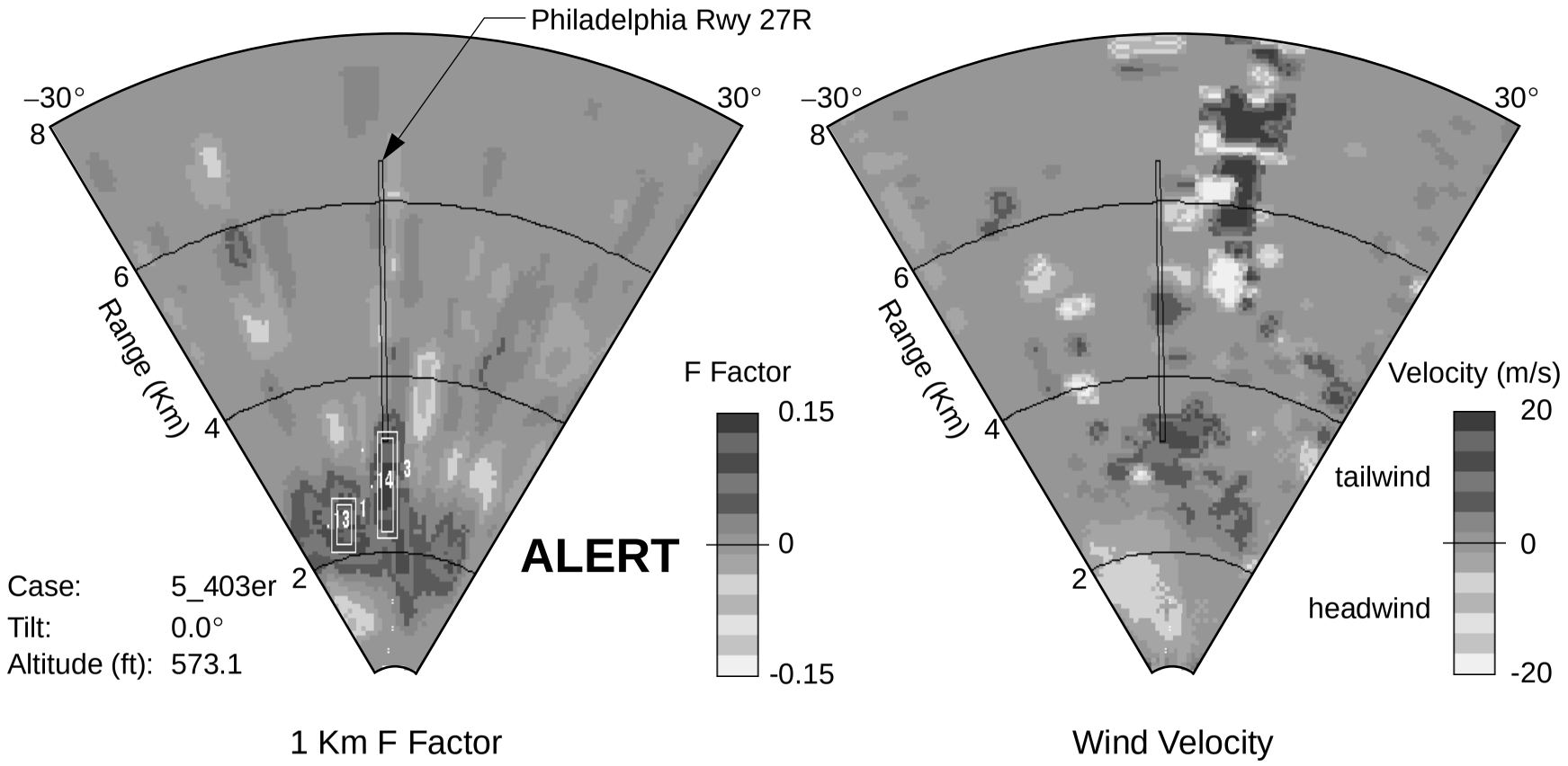

Figure B.15 Hazard and wind velocity for case 5_40_3er

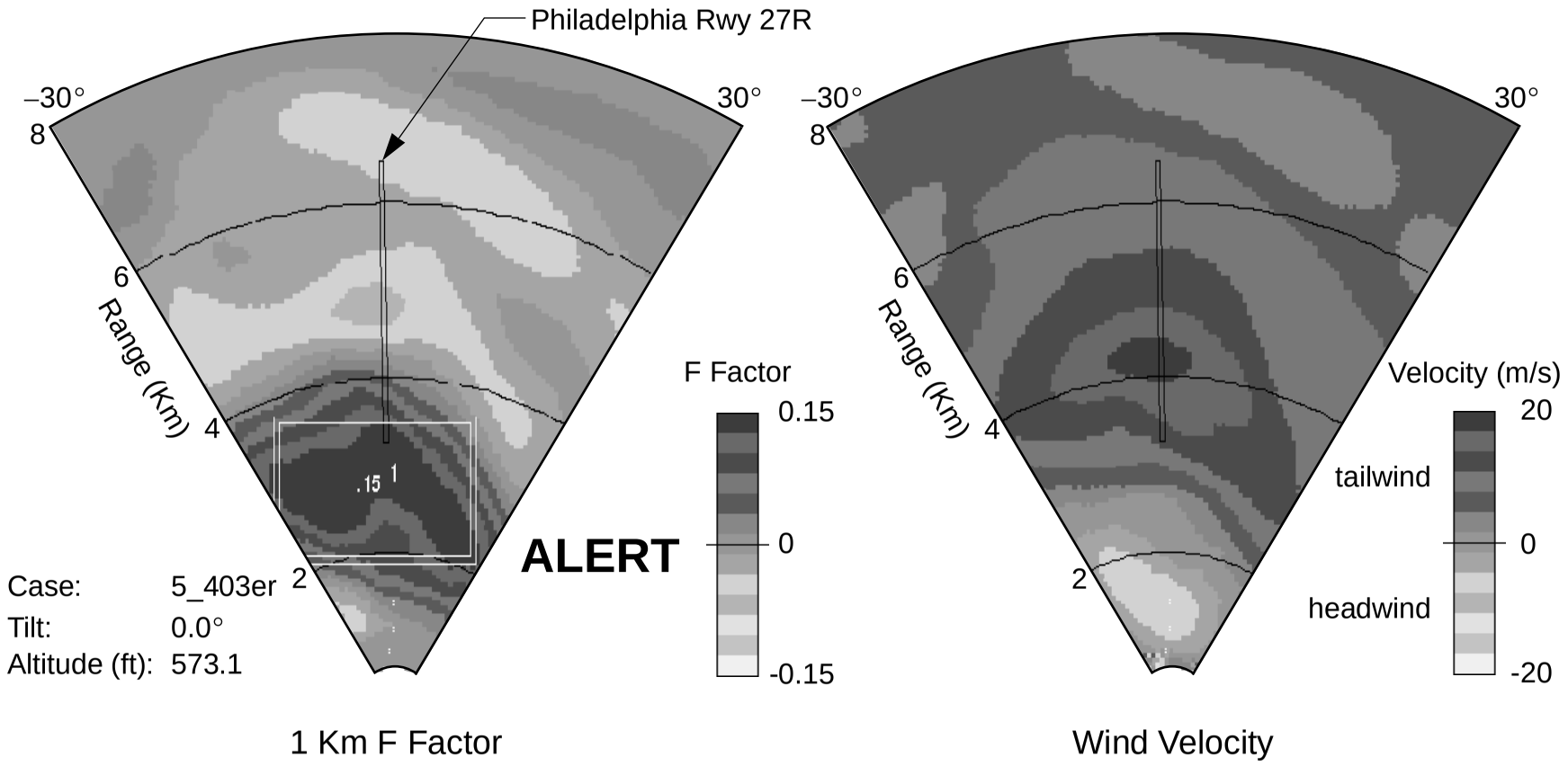

Figure B.16 True hazard and wind velocity for case 5_40_3er

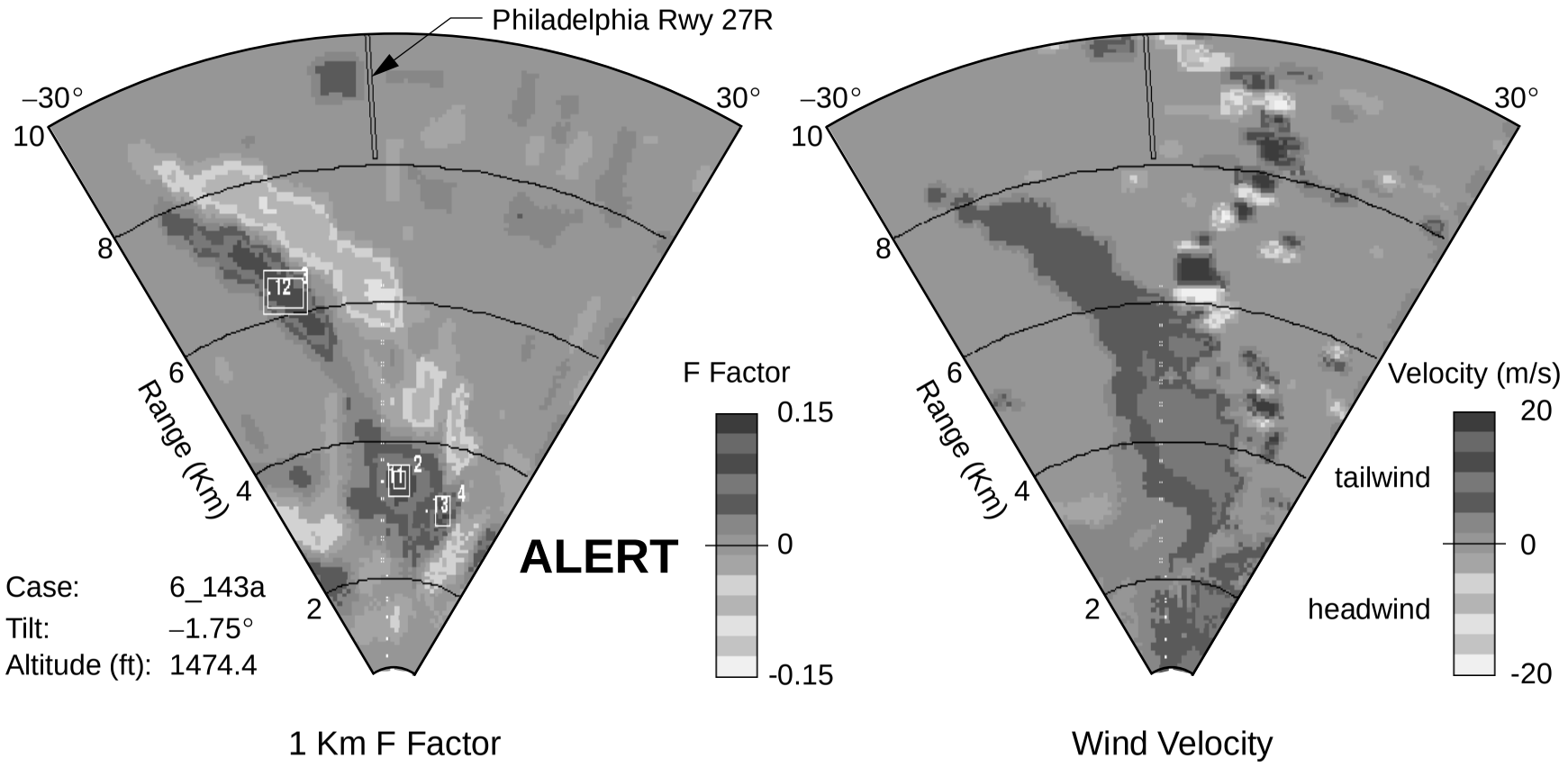

Figure B.17 Hazard and wind velocity for case 6_14_3a

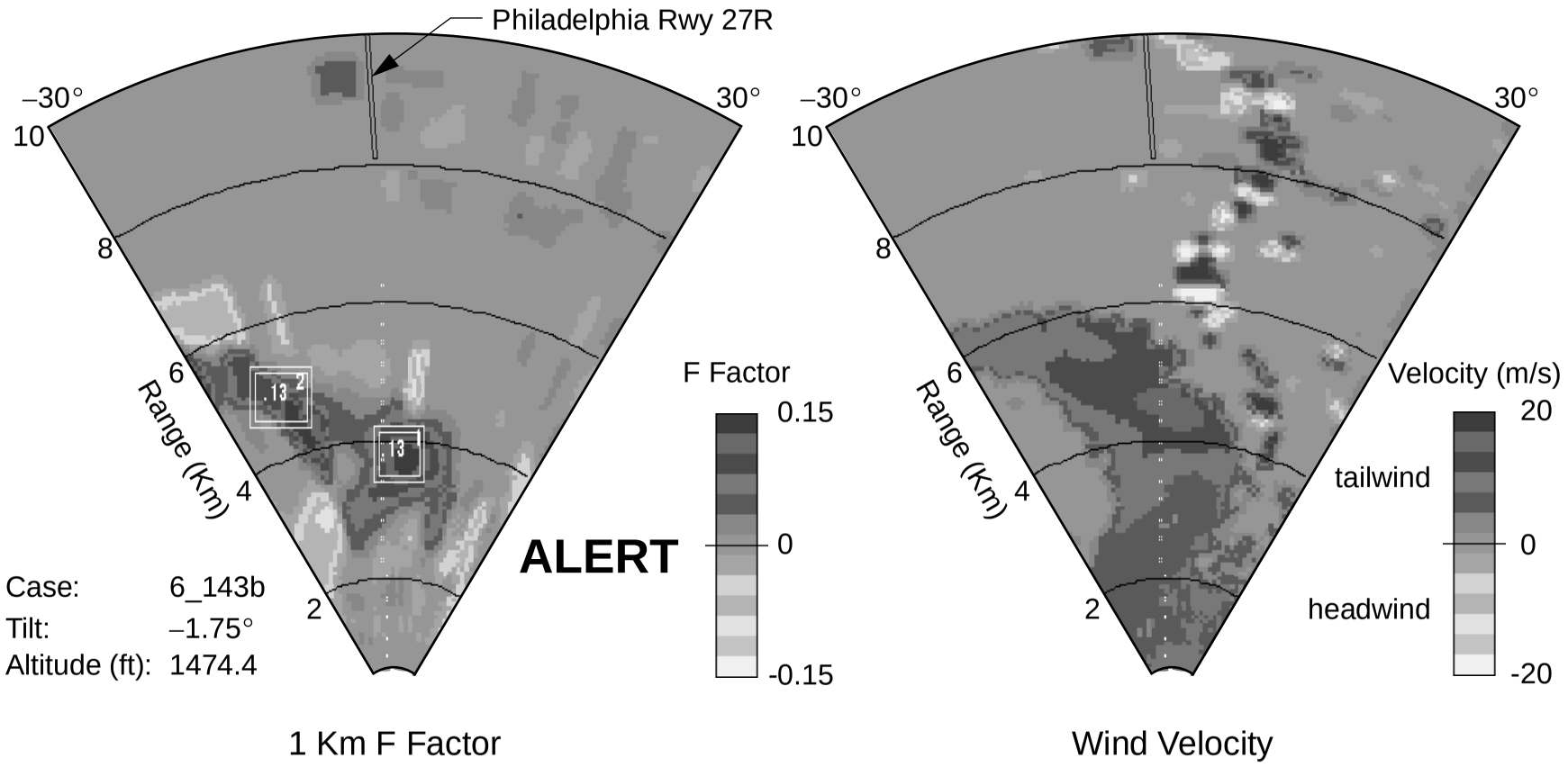

Figure B.18 Hazard and wind velocity for case 6_14_3b

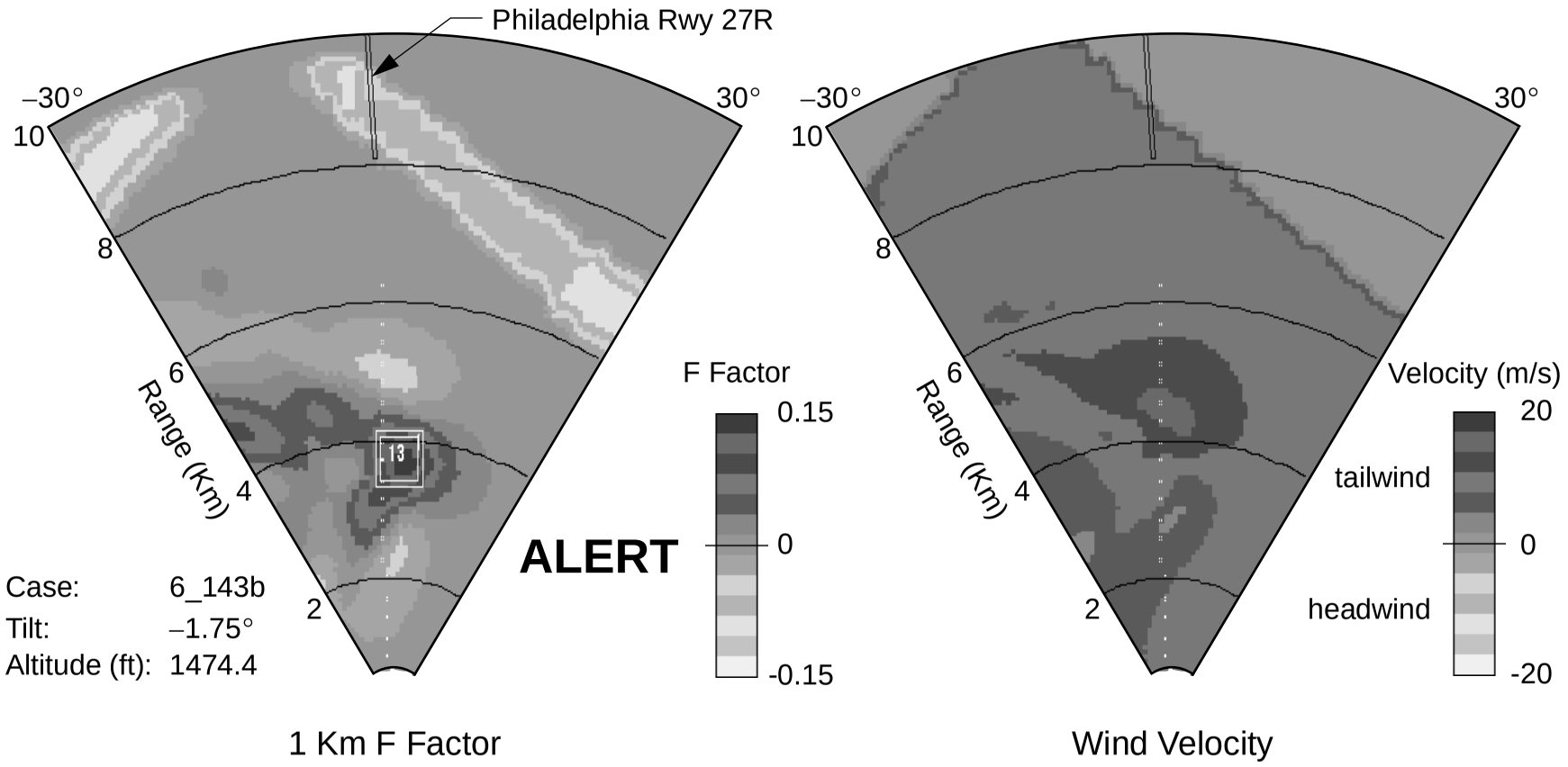

Figure B.19 True hazard and wind velocity for case 6_14_3b

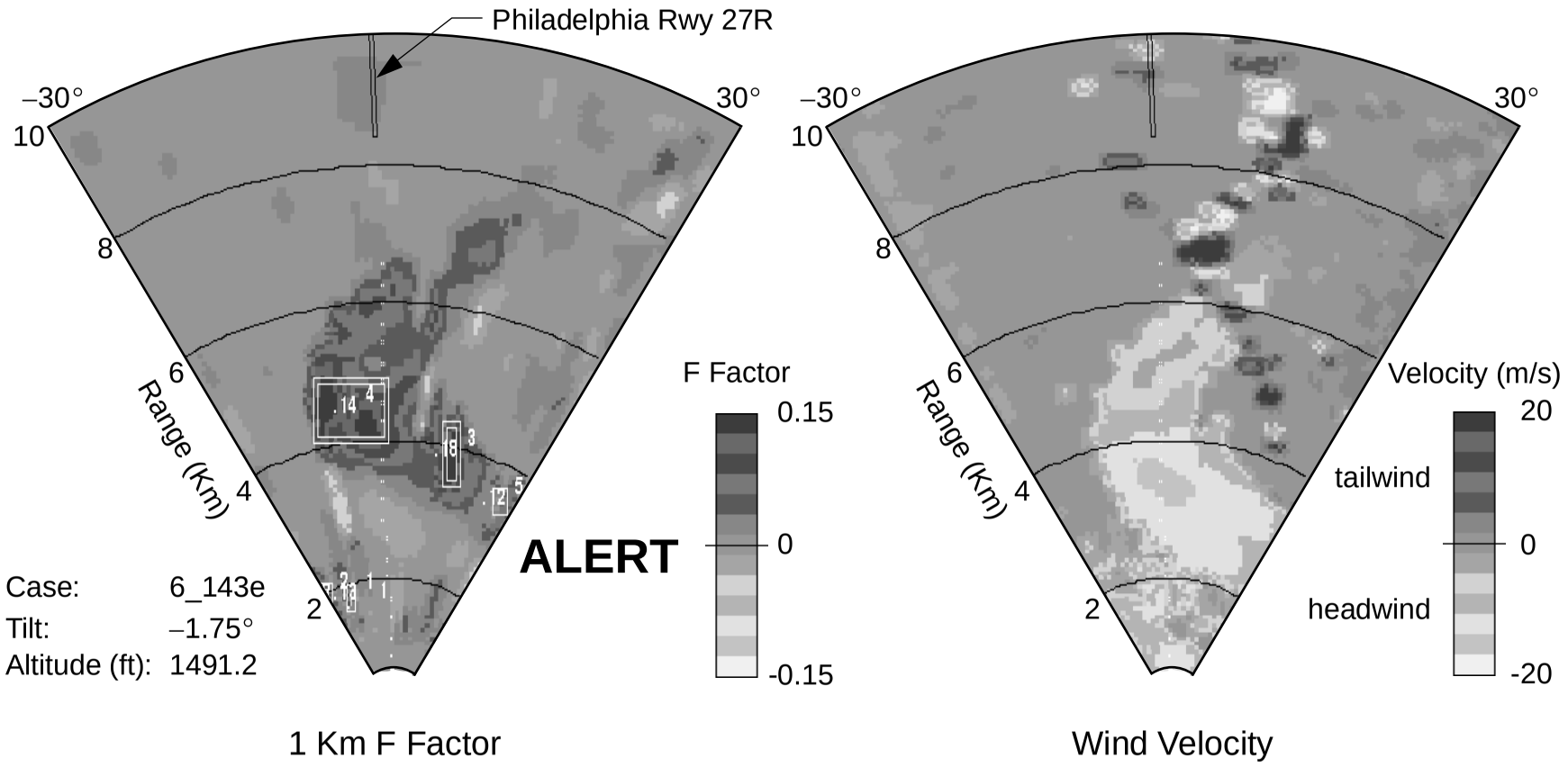

Figure B.20 Hazard and wind velocity for case 6_14_3e

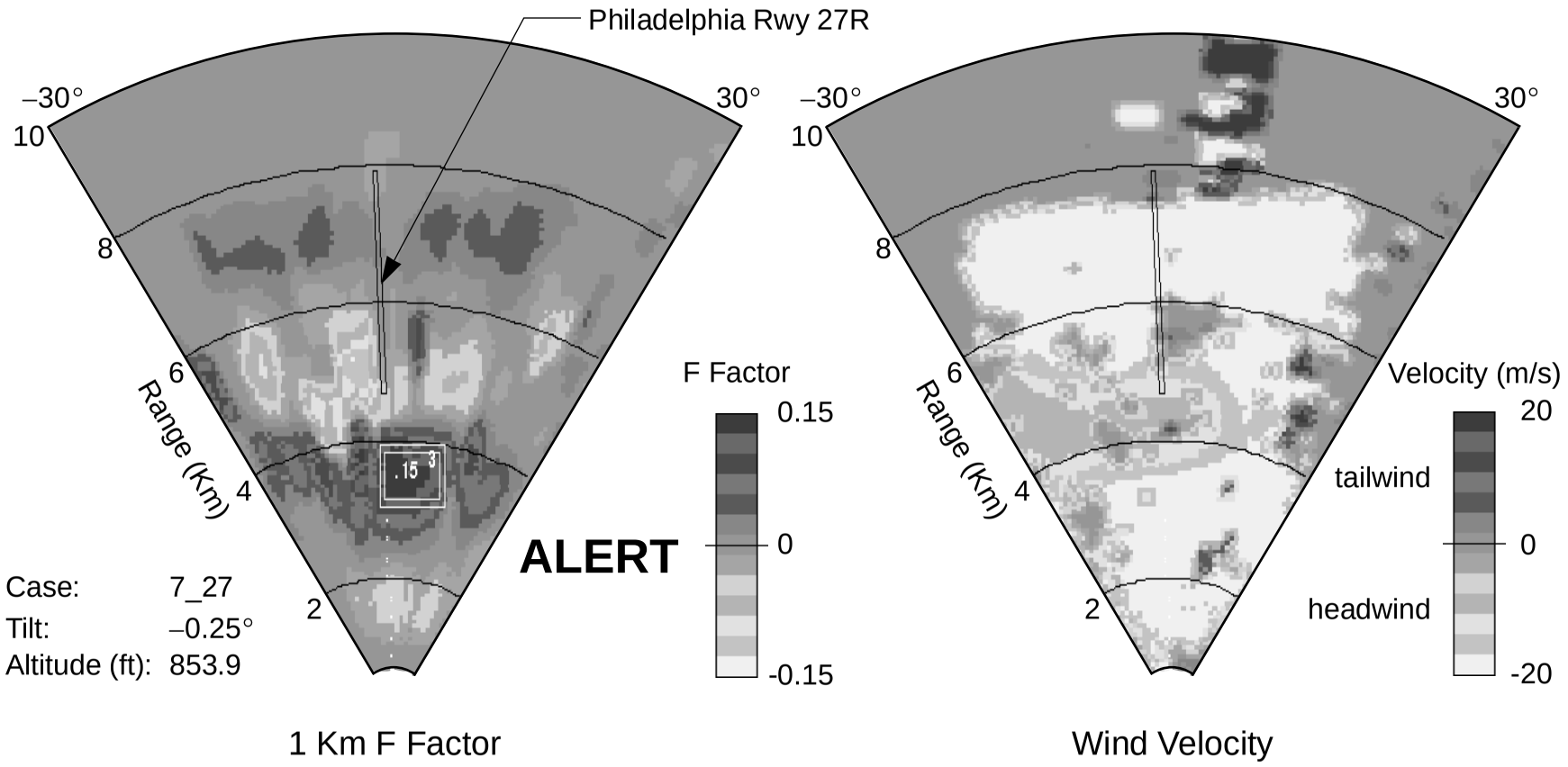

Figure B.21 Hazard and wind velocity for case 7_27_3

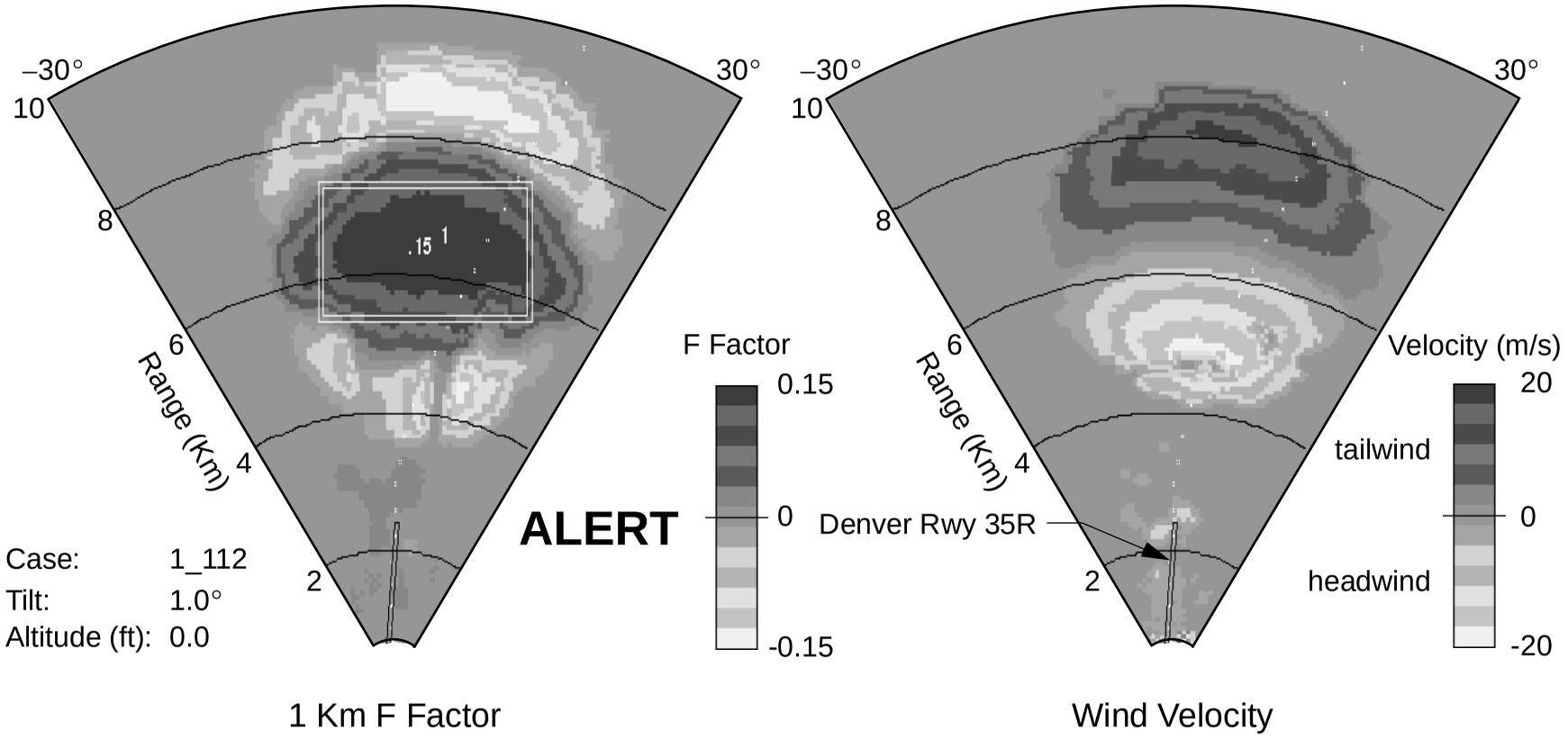

Figure B.22 Hazard and wind velocity for case 1_11_2

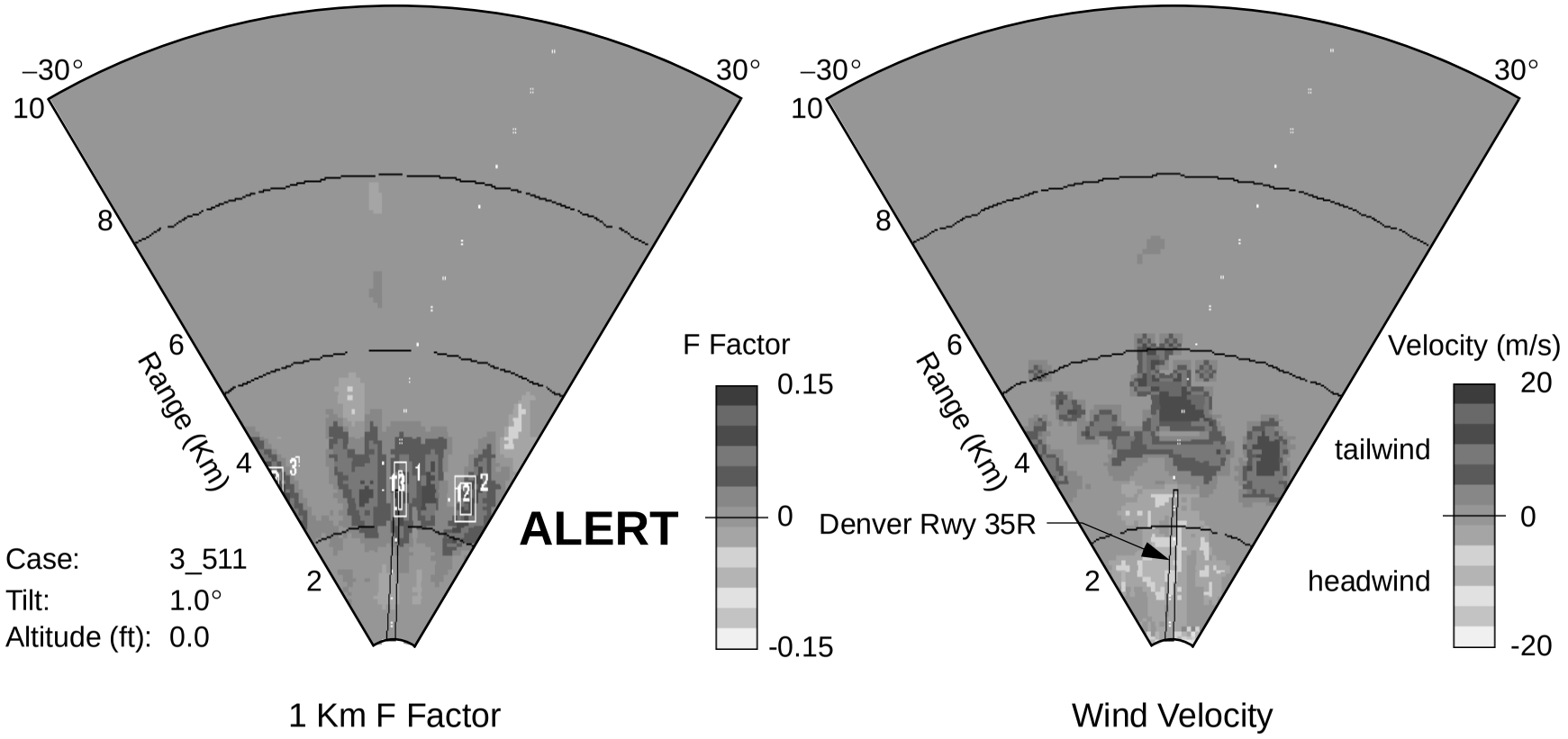

Figure B.23 Hazard and wind velocity for case 3_51_1

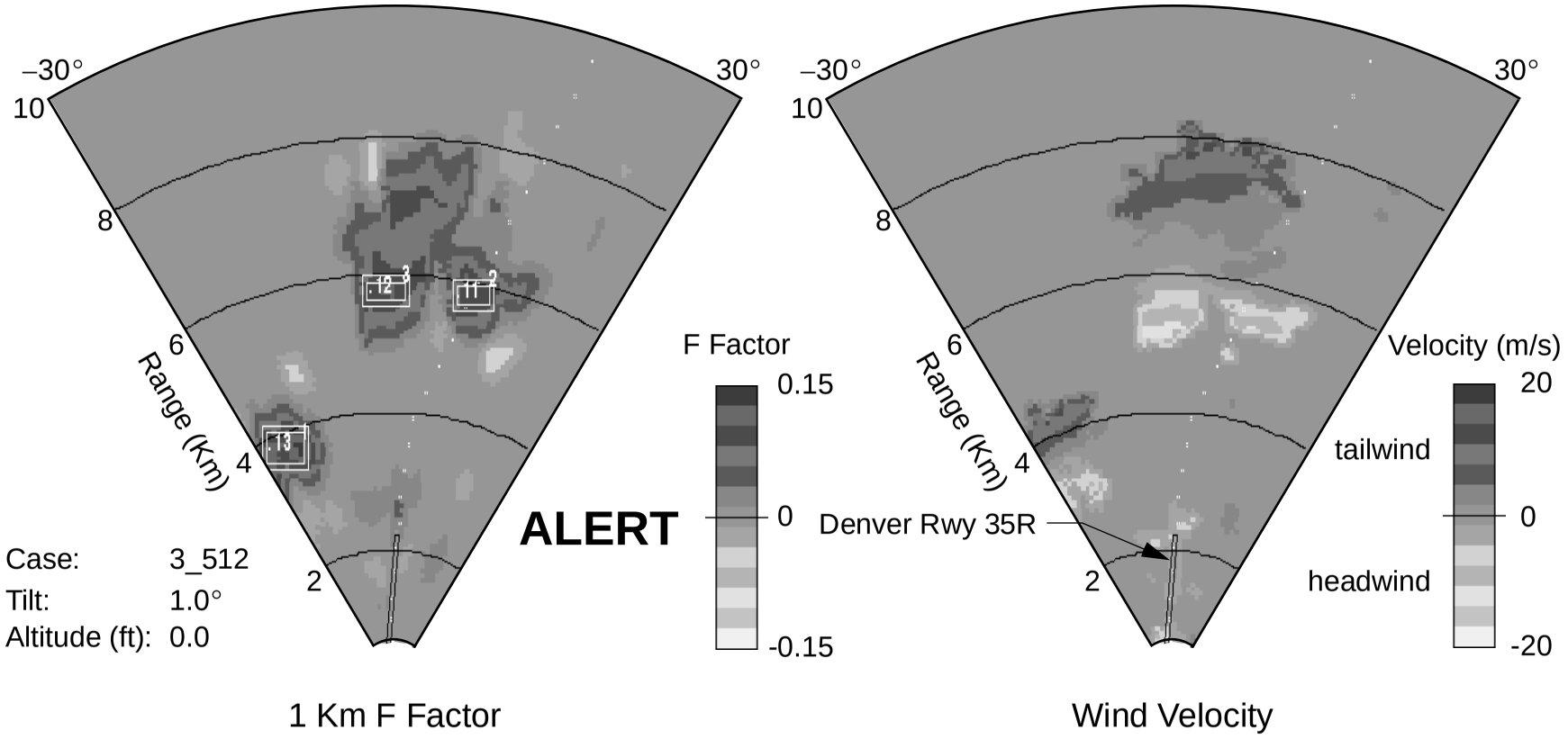

Figure B.24 Hazard and wind velocity for case 3_51_2

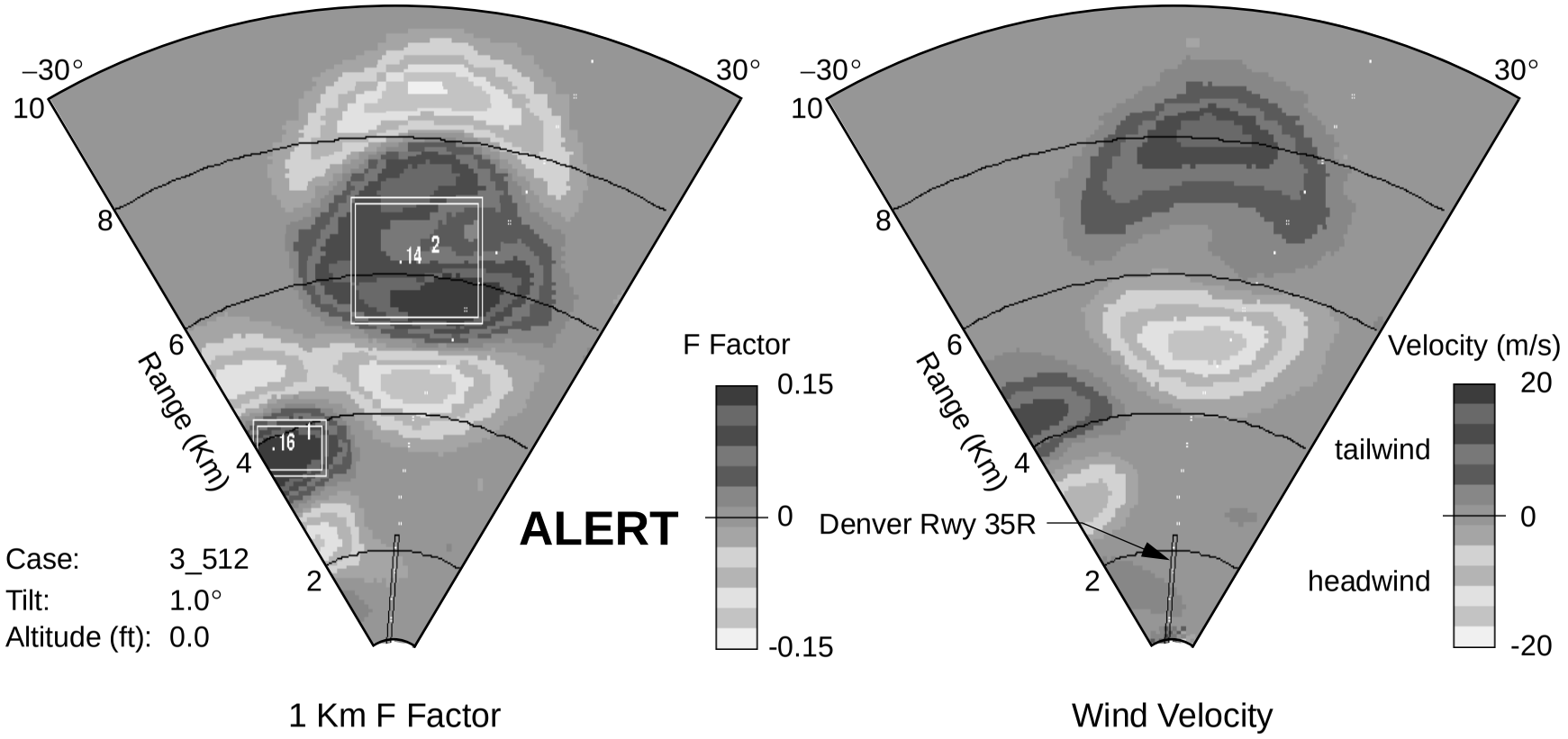

Figure B.25 True hazard and wind velocity for case 3_51_2

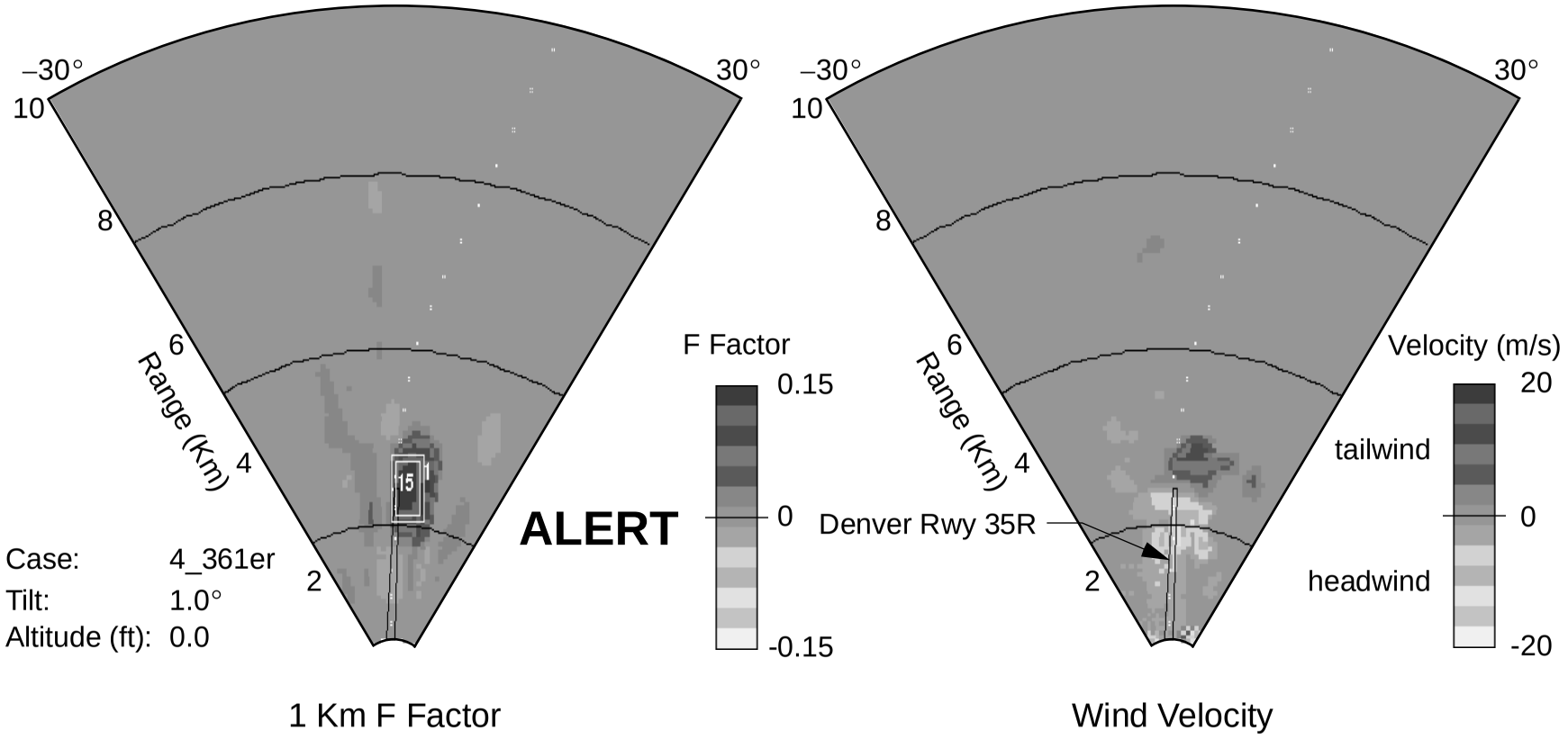

Figure B.26 Hazard and wind velocity for case 4_36_1er

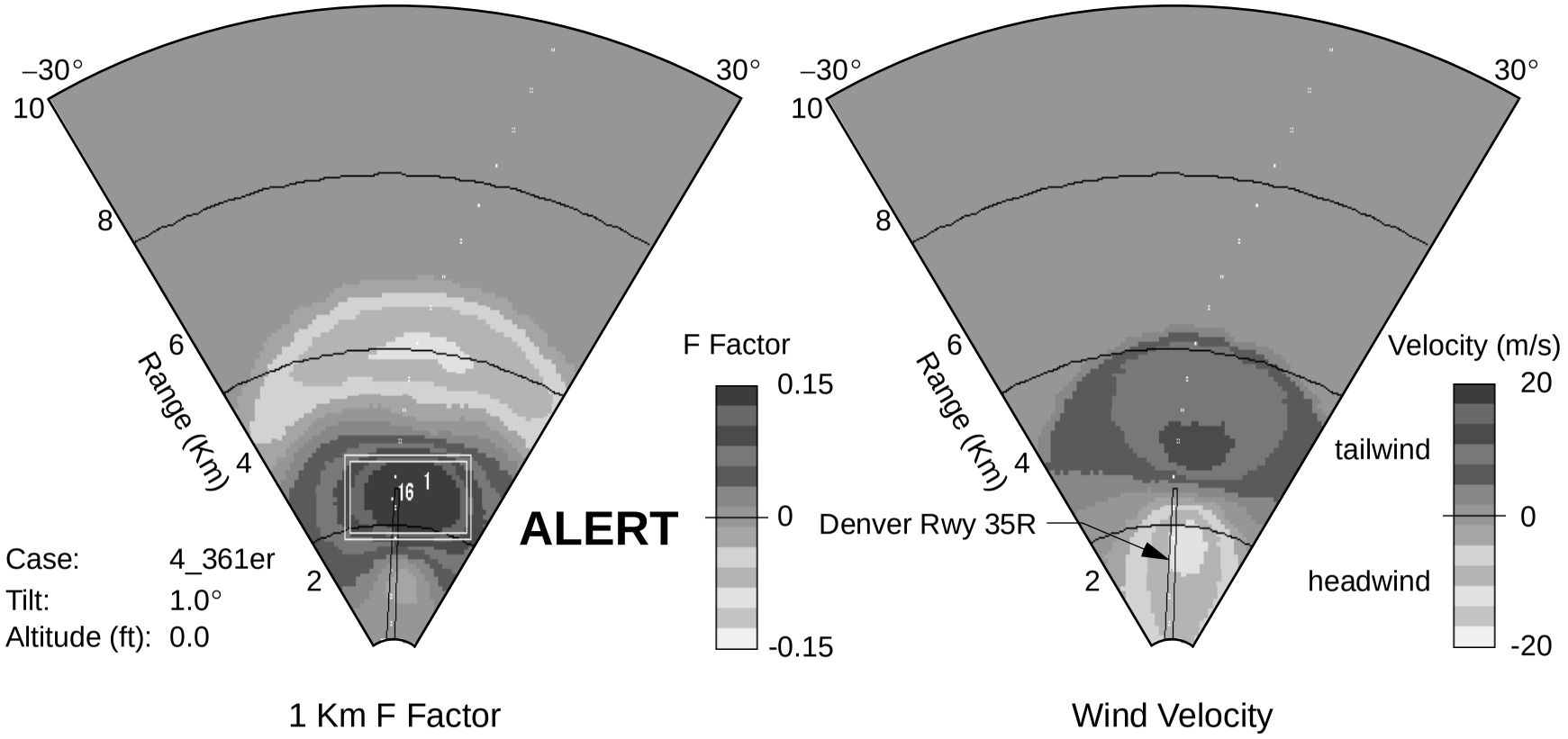

Figure B.27 True hazard and wind velocity for case 4_36_1er

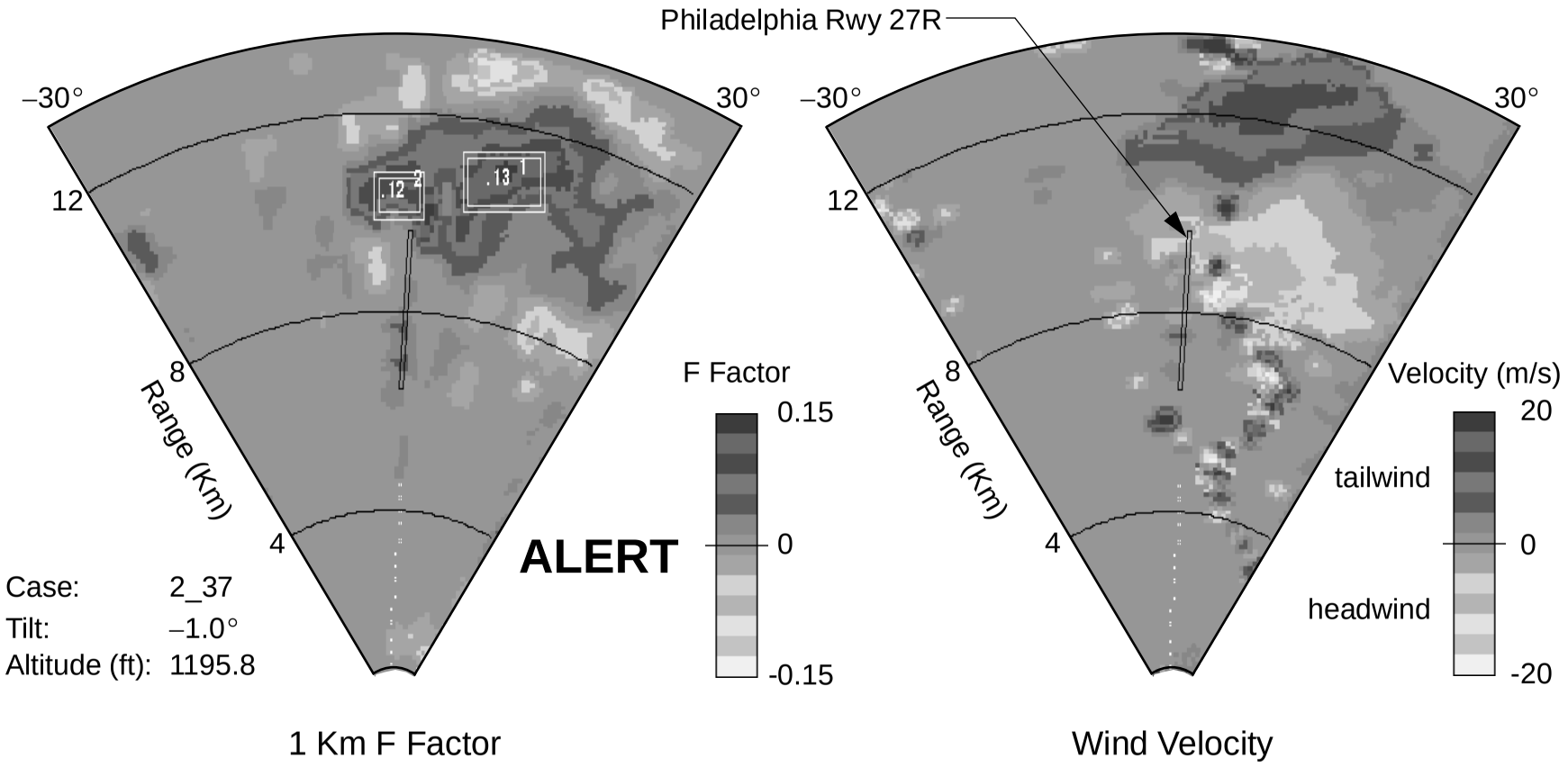

Figure B.28 Hazard and wind velocity for case 2_37_6

Appendix C

Selected Line Plots of Variables Along a Constant Azimuth

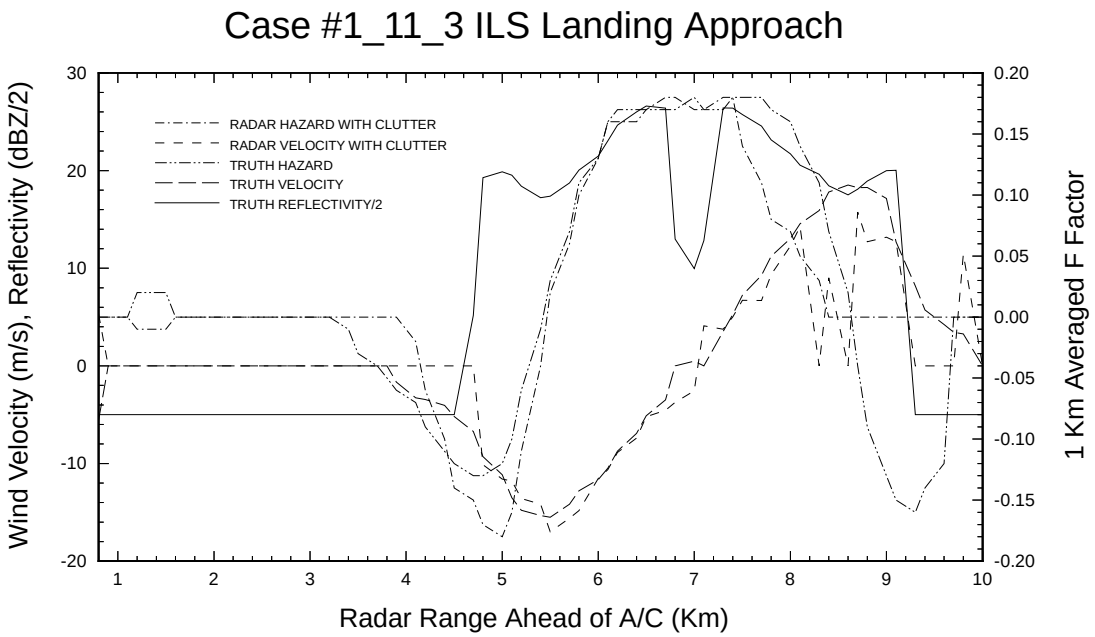

Figure C.1 Comparison truth and radar along 0˚ azimuth for case 1_11_3

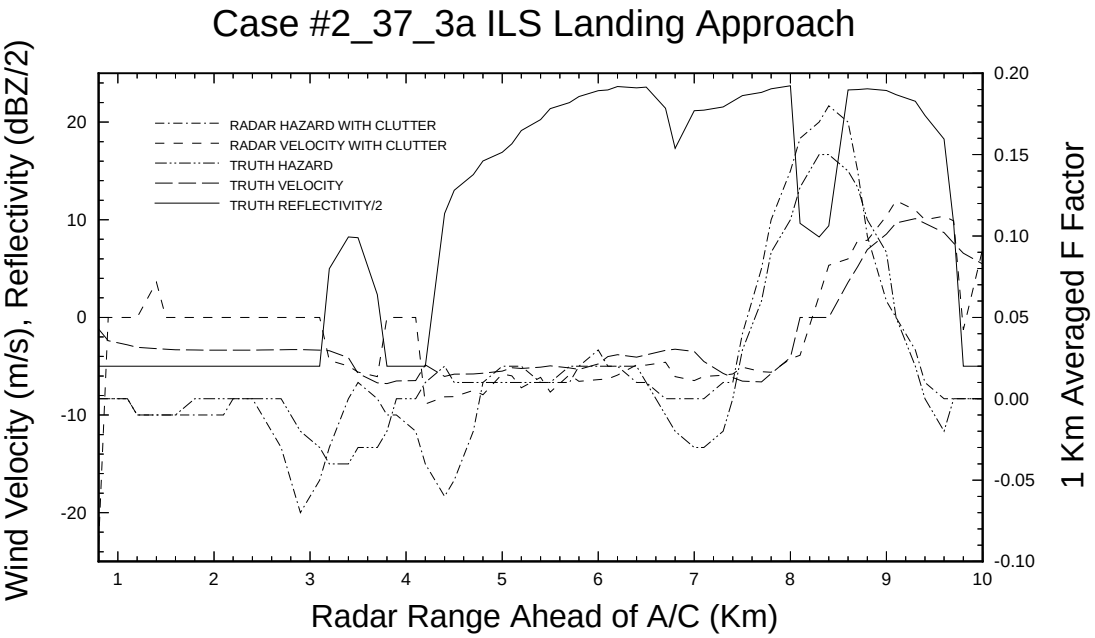

Figure C.2 Comparison truth and radar along -4˚ azimuth for case 2_37_3a

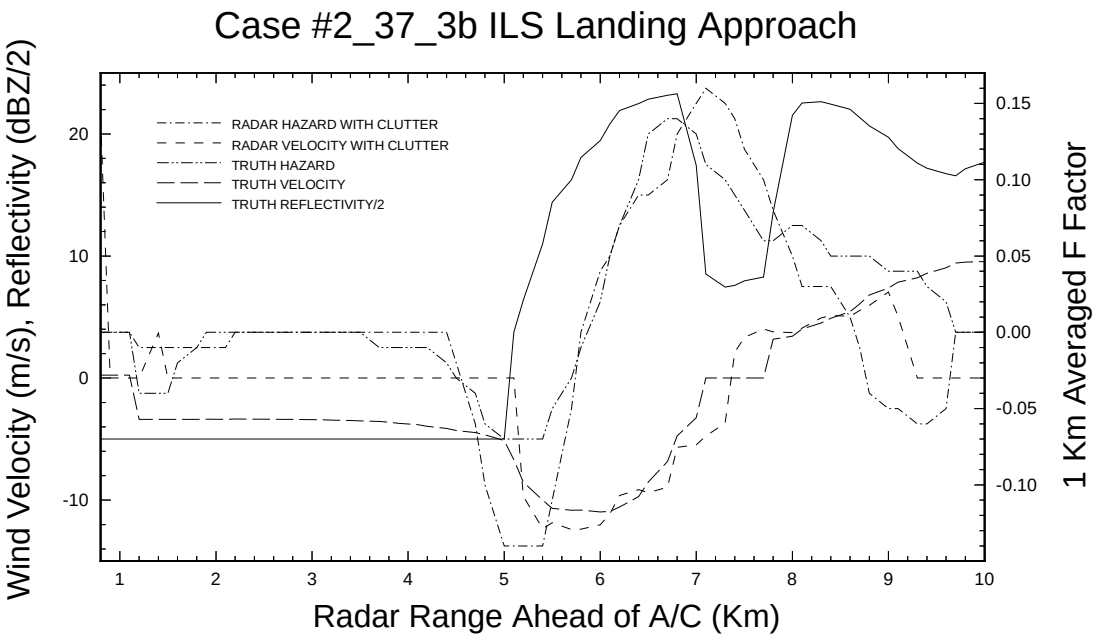

Figure C.3 Comparison truth and radar along 0˚ azimuth for case 2_37_3b

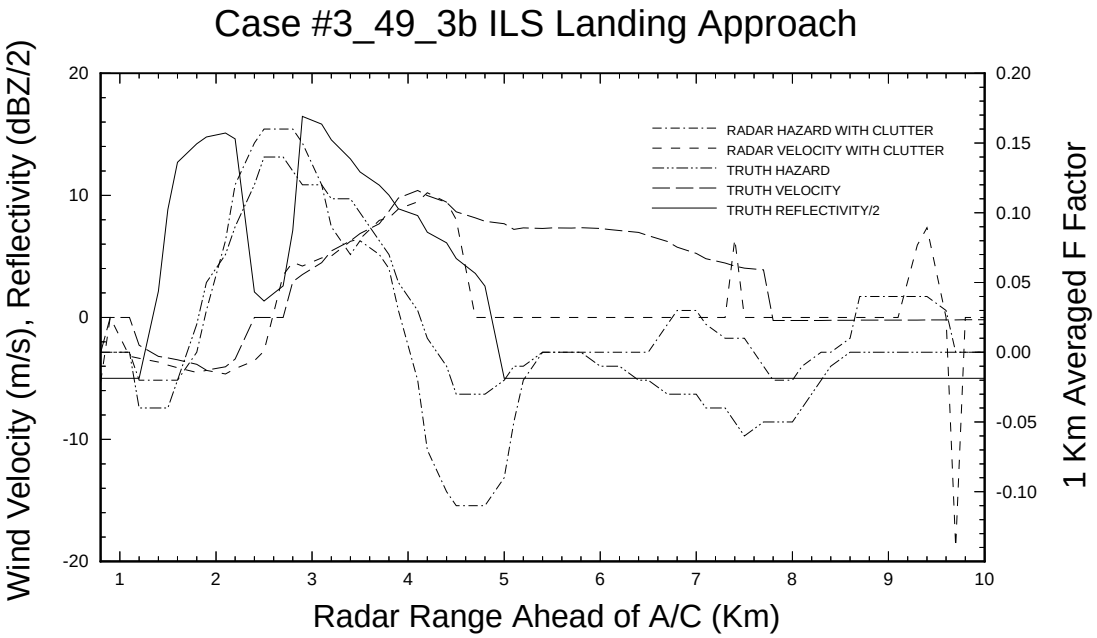

Figure C.4 Comparison truth and radar along -2˚ azimuth for case 3_49_3b

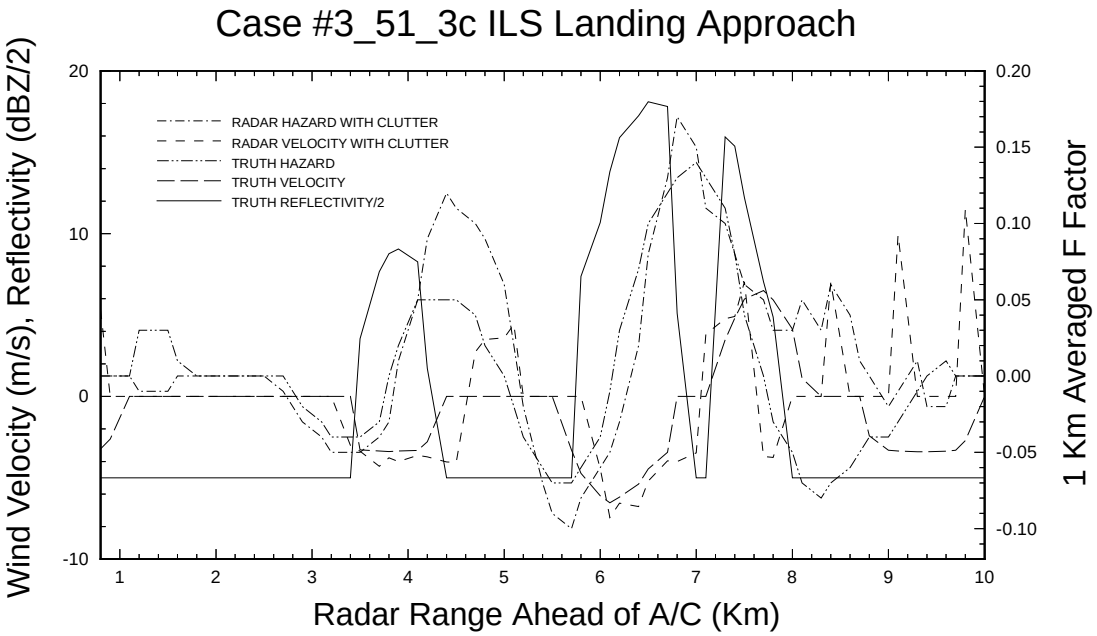

Figure C.5 Comparison truth and radar along 0˚ azimuth for case 3_51_3c

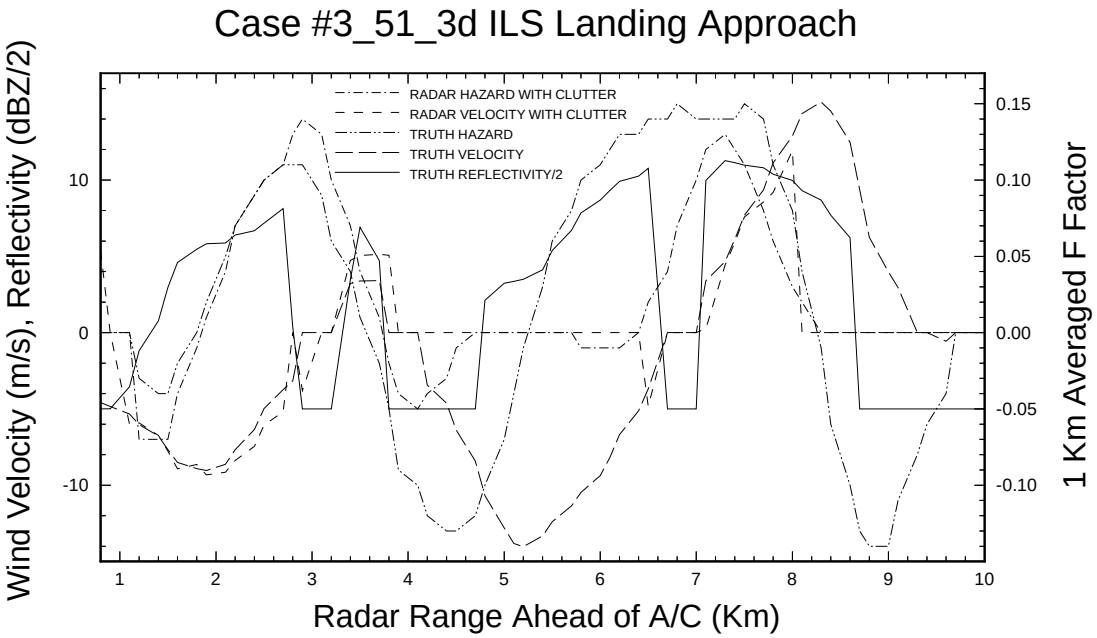

Figure C.6 Comparison truth and radar along -10˚ azimuth for case 3_51_3d

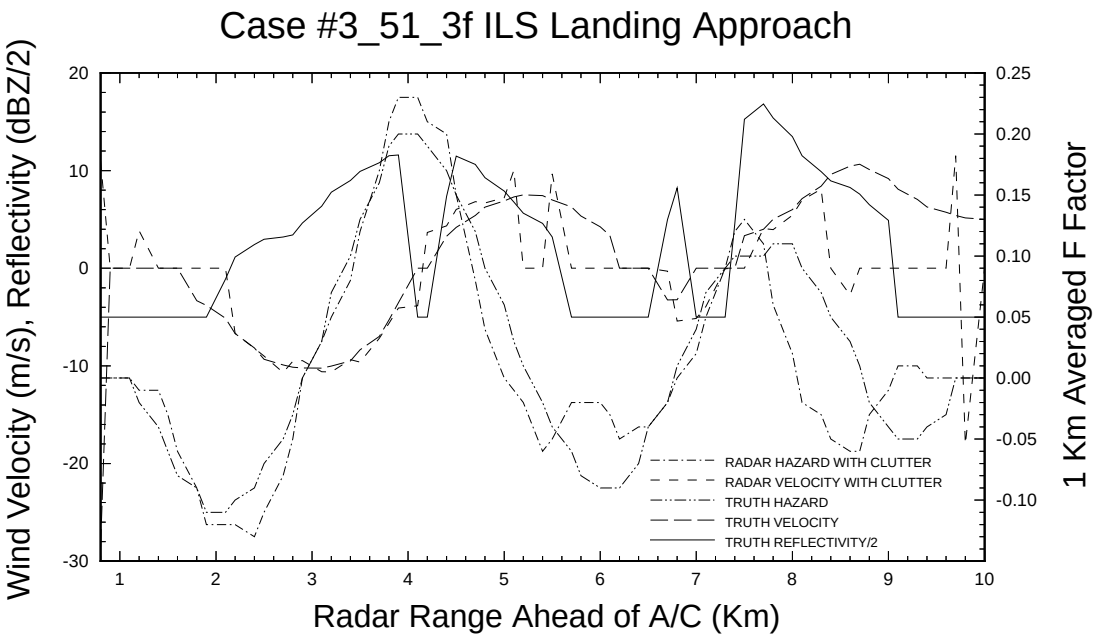

Figure C.7 Comparison truth and radar along 0˚ azimuth for case 3_51_3f

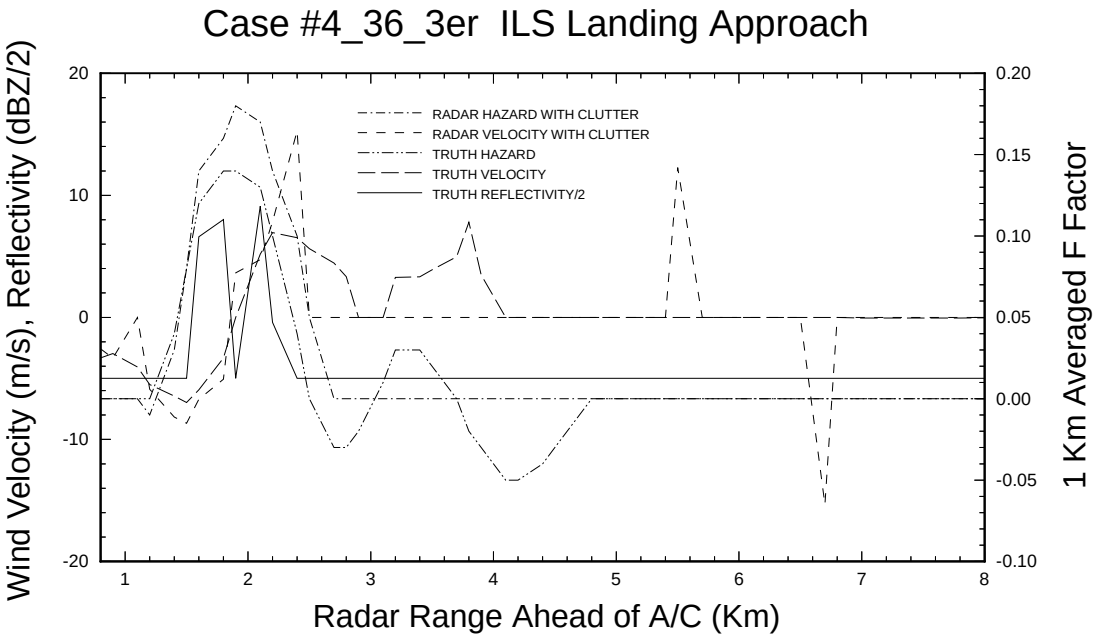

Figure C.8 Comparison truth and radar along -2˚ azimuth for case 4_36_3er

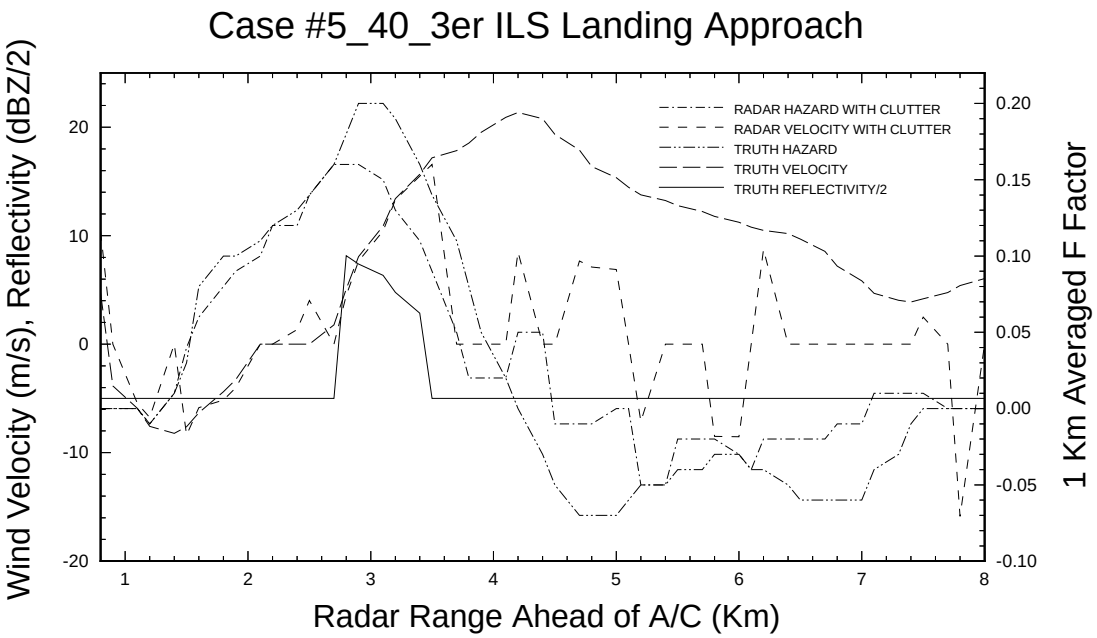

Figure C.9 Comparison truth and radar along 0˚ azimuth for case 5_40_3er

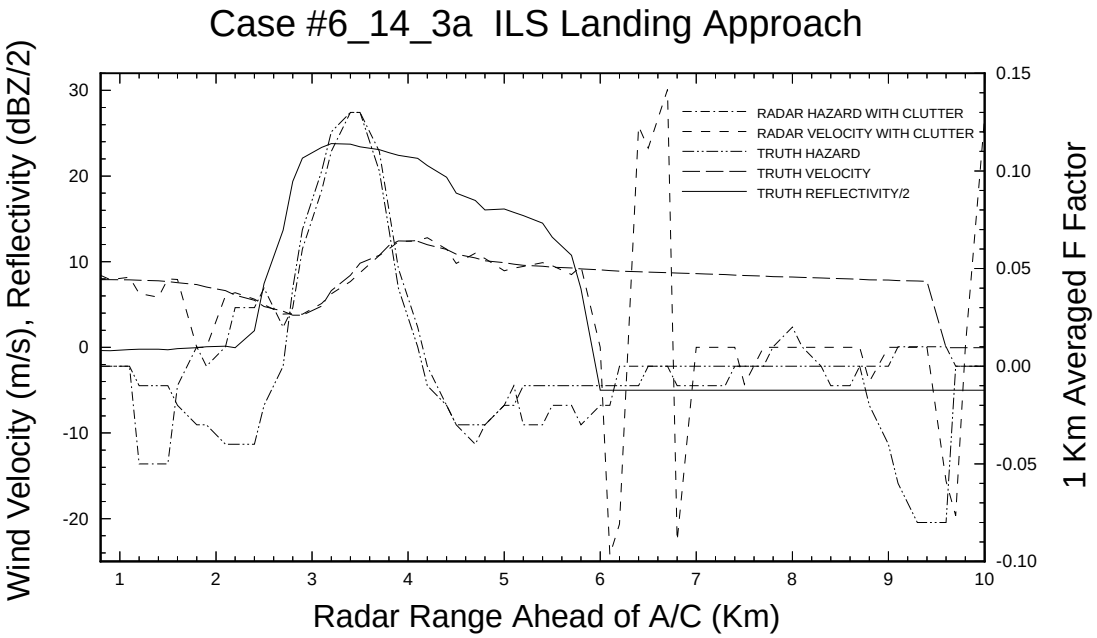

Figure C.10 Comparison truth and radar along 2˚ azimuth for case 6_14_ar

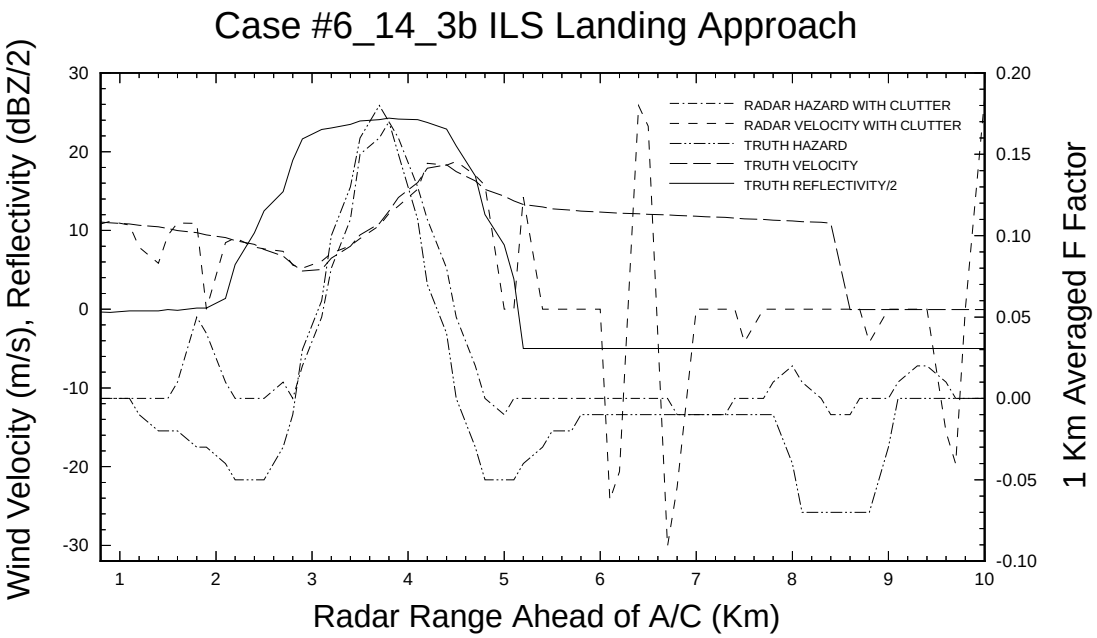

Figure C.11 Comparison truth and radar along 2˚ azimuth for case 6_14_3b

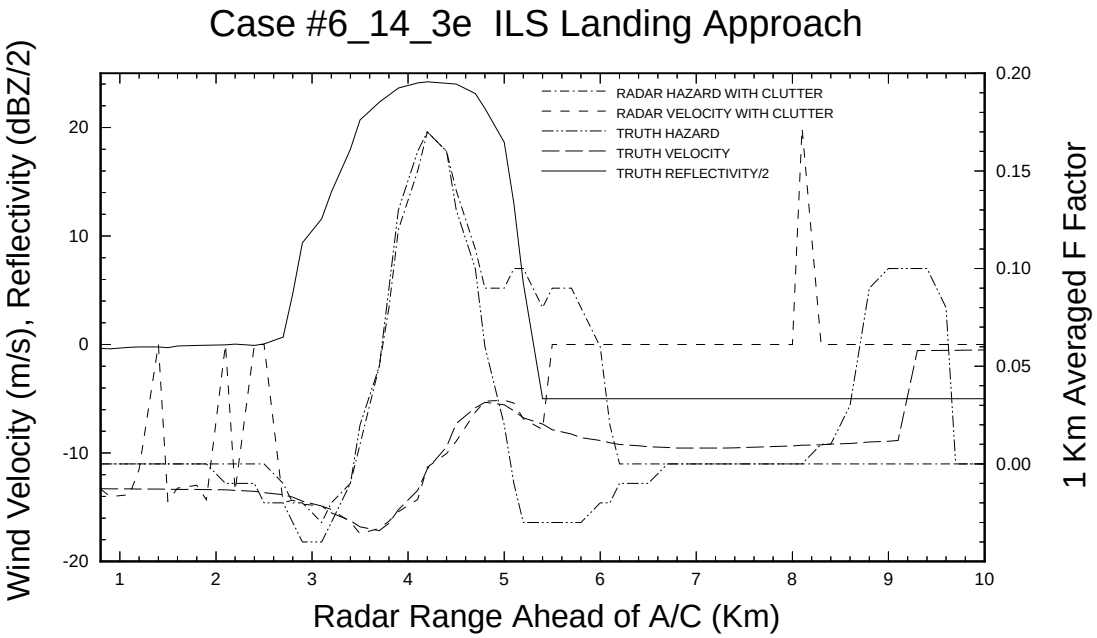

Figure C.12 Comparison truth and radar along -6˚ azimuth for case 6_14_3e

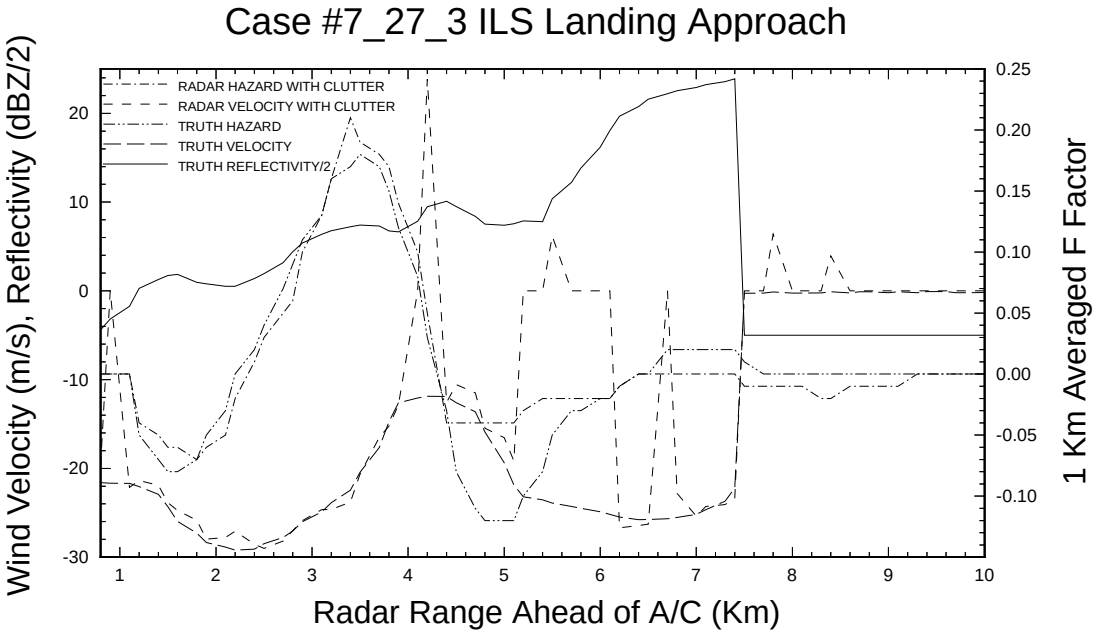

Figure C.13 Comparison truth and radar along 0˚ azimuth for case 7_27_3